COHERENT ACOUSTIC PHONONS IN METAL / DIELECTRIC SUPERLATTICES

By

Andrej Halabica

Dissertation

Submitted to the Faculty of the

Graduate School of Vanderbilt University

in partial fulfillment of the requirements

for the degree of

DOCTOR OF PHILOSOPHY

in

Physics

December, 2009

Nashville, Tennessee

Approved:

Professor Richard F. Haglund, Jr.

Professor Robert Magruder III

Professor Sharon Weiss

Professor Sokrates Pantelides

Professor Norman Tolk

To my wife, Ying, my son, Alex,
and my parents, Marta and Stanislav.

ACKNOWLEDGEMENTS

First and foremost, I thank Prof. Richard Haglund Jr., my advisor, for his expert guidance and teaching. I thank him for always asking the right and often hard questions that inspired and directed my research path. I am greatly indebted to him for molding me into a physicist and meanwhile teaching me how to master many experimental, analytical and writing skills.

I am also grateful to the other members of my committee - Profs. Robert Magruder III, Sharon Weiss, Sokrates Pantelides and Norman Tolk - for their time, advice and expertise. Special thanks go to Prof. Magruder for his willingness to part with many of his implanted samples, which I used in my experiments.

For their help, training, suggestions and many fruitful discussions, I thank my colleagues and friends: René Lopez, Eugenii Donev, Stephen Johnson, Kevin Tetz, Nicole Dygert, John Kozub, Tony Hmelo, Kannatessen Appavoo, Joyeeta Nag, Charlie Adams, Davon Ferrara, Jed Ziegler, Xiao Xia Liang, Florian Lenz and Al Meldrum. In more detail, I am grateful to Stephen Johnson for his help with the laser annealing experimental setup, Eugene Donev for helping me with the RBS measurements, Xiao Xia Liang for doing the TEM analysis, Florian Lenz for preparation of the one-layer Al_2O_3 films, Kevin Tetz for showing me how to produce nice figures using Matlab and Al Meldrum for inviting me to University of Alberta and allowing me to use his group's deposition facilities. I would also like to thank the staff of the W. M. Keck Foundation Free-Electron Laser Center for their expert operation of the facility. I am grateful for the support of a grant from the GOALI program of the National Science Foundation.

Finally, I thank my family for their support and encouragement during my graduate studies. Special thanks go to my wife Ying, not only for her moral support, but for teaching me the workings of time-resolved spectroscopy and her expert help with many pump-probe measurements. She was always there when I was getting desperate in search of a zero delay.

TABLE OF CONTENTS

LIST OF TABLES

LIST OF FIGURES

CHAPTER I

INTRODUCTION

Metal/dielectric composites are the central topic of this study. Their preparation and modification methods are discussed. Infrared pulsed laser annealing is successfully applied for modification of composites prepared by implantation. Composites with a superlattice structure are probed using time-resolved spectroscopy to study their elastic properties. This introduction starts with the motivation for our research, which is followed by a section describing basic properties of metal/dielectric composites. The theory of coherent acoustic phonon modes in superlattices is described in detail in the last section.

1.1 Motivation

Nearly all materials surrounding us are composites, which means they are composed of two or more constituents. The main reason for mixing materials is to create new materials with improved optical or physical properties. This goal was followed also in many studies of metal/dielectric composites. In this case, it is their optical properties that are among the most interesting, and the search for optimal composites with properties suitable for specific applications is not abating.

There are many different preparation processes for metal/dielectric composites. However, the prepared composites do not always possess the desired properties right away, so there is need for a post-processing method that can modify the composite

in the desired direction. One of the widely used methods is laser annealing. The availability of a pulsed laser source operating in wavelength range 2-10 μm allowed us to perform a unique study of the effects of pulsed infrared laser irradiation on metal/dielectric composites. The laser annealing process was successfully applied to our Au and Ag implanted samples. Results presented in Chapter III show that growth and nucleation of Au nanoparticles in both SiO_2 and Al_2O_3 matrices is observed. On the other hand, pulsed infrared laser annealing seems to cause dissolution of Ag nanoparticles in a SiO_2 matrix due to the high diffusivity of Ag atoms.

Implantation is not an optimal metal/dielectric composite preparation method because it is usually a time-consuming and low yield process. We decided to prepare a composite made up of alternating thin metal and dielectric layers by electron beam evaporation. The aim at this stage was primarily coloration of such multilayer structure, which is achieved due to the nanoparticle structure of the thin metal films. The multilayer is analyzed using time-resolved pump-probe spectroscopy and an oscillatory signal is detected, which is traced back to coherent acoustic phonons and related surface modes of our superlattice. Previous studies of this phenomenon deal mostly with smooth continuous films and use the experimental data to determine the elastic constants of the superlattices and their constituents. This spurred our interest to study the effects of the nanoscale structure of the metal films on their apparent elastic properties in these superlattice structures. A new set of multilayer samples with varying Au layer thickness was prepared, and a comprehensive time-resolved spectroscopy study of these samples plus a few others is presented in Chapter IV.

1.2 Composite materials - metal/dielectric

The visual appearance of a solid is closely related to its optical properties in the visible wavelength range of the spectrum; these optical properties are determined by the electronic properties, including defects and physical structure. Dielectric solids are insulators and have no free electrons to absorb (reflect) light in the visible and near-infrared wavelength region, so they are transparent in the given range. There are several possible ways of changing the visual appearance of dielectrics, such as doping them with some other material or structuring their surfaces. Concerning addition, the usual materials that are incorporated into the dielectric matrices are metals and semiconductors. Once they are mixed in, a composite material is created that may have significantly different optical properties than the original dielectric.

In recent years, there has been increased interest in the composite materials made of a metal and a dielectric matrix. This interest is driven by the fact that, in such composites, the metal usually exists in the form of nanoparticles, which often exhibit strong surface plasmon resonance (SPR) extinction bands in the visible spectrum resulting in deep coloration [1]. Often, only classical free-electron theory and electrostatic limit models of particle polarizability are needed to understand the spectra of metal nanoparticles. The position of the SPR peak can be shifted by up to hundreds of nanometers just by changing nanoparticle shape, size, number density in the composite material and the dielectric properties of the surrounding medium. This variability significantly contributes to the interest in such composites. Another property that draws attention to them is the enhanced third-order optical nonlinearity, which has

potential use in several optical applications such as nonlinear optical switches, directional couplers etc [2]. The dielectric confinement that produces the SPR in metal nanoparticles is also the cause of the high third-order optical susceptibility in these composites [3]; this nonlinearity is generated by interband electronic transitions involving collective plasma excitations in the nanoparticles. In addition to dielectric confinement, composites in which the metal nanoparticles are smaller than 10-15 nm exhibit an additional enhancement due to quantum confinement of the interband electronic transitions. Consequently, this effect is most efficient in the spectral range near the position of a SPR maximum. In order to enhance the effect, attempts are usually made to increase the concentration of metal nanoparticles in a composite layer, thus enhancing the absorption in the SPR region.

Metal nanoparticles have been known for centuries; probably the oldest object containing gold nanoparticles is the Lycurgus chalice from fifth-century Rome. Later on in the seventeenth century Johann Kunckel is credited for developing the first systematic procedures for incorporating gold into molten silica, thus producing ruby glass[1]. However, the physical basis of color in these applications was not known at that time. In 1904 J. C. Maxwell-Garnett made the first attempt to explain theoretically the colors of metal nanoparticles. His theory was applicable only to particles whose dimensions were negligible in comparison to the wavelength of the incident light. In 1908 Gustav Mie presented the first rigorous theoretical treatment of the optical properties of spherical metal particles [4]. His theory is applicable to spheres of any size and produces results that fit the experiments well. Mie's approach was later adapted also to other shapes of nanoparticles. Since then, the general

interest in the metal-nanoparticle composites and also the particles themselves was growing and at present this field is still expanding rapidly. Nowadays the metal nanoparticles are not important only in physics, but also in many other research fields, such as chemistry, geology, mineralogy, astrophysics, biology and medicine, where they already have many useful applications [3].

The study of metal-dielectric composite materials requires that one understand the basic physics of the constituent materials. In particular, the knowledge of their dielectric functions and their structural arrangement in the composite is crucial in determining the optical properties of the composite. The understanding of those properties can then be further used for designing experiments that can modify and tune the optical properties for practical applications.

1.2.1 Optical properties - metals vs dielectrics

A crystalline solid is composed of periodically arranged atoms, which create a periodic potential field for the electrons present in the solid. By solving for the electron wave equation in this periodic potential, the electronic band structure can be obtained [5]. The band structure tells us that the electrons in crystals are arranged in energy bands, separated by band gaps where there is no solution to the wave equation. The crystal is an insulator if the highest occupied energy (valence) band is fully filled and the lowest unoccupied energy (conduction) band is empty. The same configuration holds for semiconductors, but their band gap is usually less then 4 eV and their resistivity can be easily controlled by doping. Metals have their conduction band only partly filled, which means there is a continuum of states available for the

electrons right above the highest occupied state. This allows treating the electrons close to that energy state as nearly free. Such a model gives useful insights into the properties of metals, such as heat capacity, thermal conductivity or electrical conductivity. The optical properties of a crystal are closely related to its dielectric function $\epsilon(\omega,\mathbf{K})$, which describes the response of the crystal to an electromagnetic field. The dielectric function depends on the electronic band structure of the crystal, which can be determined by optical spectroscopy measurements. The wavevector of the electromagnetic radiation in the infrared, visible and ultraviolet wavelength region is usually very small compared to the shortest reciprocal lattice vector, and therefore it is usually taken to be zero. Then we are left with the dielectric function at zero wavevector. The measurable functions such as the reflectance *R(ω)*, the refractive index *n(ω)* and the extinction coefficient *K(ω)* are related to the dielectric function and can be used to calculate it. Using the classical theory of electrodynamics, the relation between the reflectance R, which is the ratio of the reflected intensity of normal incident radiation to the incident intensity, and the dielectric function is [6]:

$$R = \left| \frac{1-\sqrt{\epsilon}}{1+\sqrt{\epsilon}} \right|^2 . \tag{1.1}$$

The dielectric function is complex and its real and imaginary parts $\epsilon = \epsilon_1 + i\epsilon_2$ are related by

$$\epsilon_1(\omega) = 1 + P\int_{-\infty}^{\infty} \frac{dw}{\pi} \frac{\epsilon_2(w)}{w-\omega}, \qquad \epsilon_2(\omega) = -P\int_{-\infty}^{\infty} \frac{dw}{\pi} \frac{\epsilon_1(w)-1}{w-\omega} . \tag{1.2}$$

These relations are known as Kramers-Kronig relations and P stands for the Cauchy principal value. Consequently, there is only one unknown function (ϵ_1 or ϵ_2). Assuming reflectivity R can be measured in a wide range of frequencies, then both ϵ_1 and ϵ_2 can be determined using the Kramers-Kronig relations. If only transitions within a single band (intraband), intersected by the Fermi level, are taken into account, then the frequency-dependent dielectric function is given by

$$\epsilon(\omega) = 1 - \frac{\omega_p^2}{\omega(\omega + i/\tau)} \tag{1.3}$$

where ω_p is the plasma frequency and τ is relaxation time; this model is known as the Drude model. In the case where the only allowed transitions are between occupied and unoccupied bands separated by a band gap (interband transitions), the expression for the dielectric function is more complicated and is known as the Lorentz model,

$$\epsilon(\omega) = 1 - \frac{\omega_p^2}{(\omega^2 - \omega_0^2) + i\eta\omega} \tag{1.4}$$

where ω_0 and η are two additional constants. The dielectric function of an insulator is derived from interband contributions only, but that of a metal with several bands has interband as well as intraband contributions.

1.2.1.1 Metal Nanoparticles

The interaction of light with metal nanoparticles stimulated most of the scientific research in this field. The main reason for that is the way metals respond to electro-

magnetic waves, which is described by their dielectric function $\epsilon(\omega)$. Equation (1.3) shows the dielectric function of a free-electron metal, in which most of the electronic and optical properties are due to the conduction electrons alone. Alkali metals, magnesium and aluminum are standard examples of the free-electron metals. However, there are many other metals in which interband transitions from lower-lying bands into the conduction band, or from the conduction band into higher unoccupied levels, contribute significantly to the dielectric function. The influence of electrons which undergo such transitions contributes additional complex terms to $\epsilon(\omega)$.

In 1908, G. Mie presented a complete solution to Maxwell's equations for a spherical nanoparticle. His theory provides an accurate description of the extinction spectra of spheres. The calculation is performed by solving Maxwell's equations in spherical polar coordinates and using the usual boundary conditions for the fields at the surface of the particle. The optical properties are usually expressed in terms of absorption and scattering cross sections σ_{abs} and σ_{sca}. In practice, absorption and scattering both contribute to the intensity loss of a beam of incident light. Then the resulting extinction cross section is $\sigma_{ext} = \sigma_{abs} + \sigma_{sca}$. All the cross sections are calculated from Mie theory by series expansion of the involved fields into partial waves of different spherical symmetries. Using the notation of Bohren and Huffman [7]

$$\sigma_{ext} = \frac{2\pi}{|\boldsymbol{k}|^2} \sum_{L=1}^{\infty} (2L+1) \mathrm{Re}\{a_L + b_L\} \tag{1.5}$$

$$\sigma_{sca} = \frac{2\pi}{|\boldsymbol{k}|^2} \sum_{L=1}^{\infty} (2L+1)(|a_L|^2 + |b_L|^2) \tag{1.6}$$

$$\sigma_{abs} = \sigma_{ext} - \sigma_{sca} \tag{1.7}$$

where

$$a_L = \frac{m\psi_L(mx)\psi_L^{'}(x) - \psi_L^{'}(mx)\psi_L(x)}{m\psi_L(mx)\eta_L^{'}(x) - \psi_L^{'}(mx)\eta_L(x)}$$

$$b_L = \frac{\psi_L(mx)\psi_L^{'}(x) - m\psi_L^{'}(mx)\psi_L(x)}{\psi_L(mx)\eta_L^{'}(x) - m\psi_L^{'}(mx)\eta_L(x)} \tag{1.8}$$

$m = n/n_m$, where n denotes the complex index of refraction of the particle, which is related to the dielectric function by $n = \sqrt{\epsilon}$, and n_m is the real index of refraction of the surrounding medium. $\boldsymbol{k}$ is the wavevector, $x = |\boldsymbol{k}|R$ is the size parameter and R is the particle radius. The prime here indicates differentiation with respect to the argument in parenthesis. The functions $\psi_L(x)$ and $\eta_L(x)$ are cylindrical Riccati-Bessel functions. The summation index L is the order of spherical multipole excitations in the particles: $L = 1$ corresponds to dipole fields, $L = 2$ to quadrupole and so on. a_L and b_L represent the amplitude of electric and magnetic oscillation, respectively. The electric-multipole excitations are surface-plasmon polariton modes while the magnetic multipoles are due to eddy currents and also due to electronic excitations. In order to obtain the cross sections, the coefficients a_L and b_L have to be calculated using equation (1.8).

If the particles are very small compared to the wavelength of the light ($R \ll \lambda$), the Mie formula can be simplified considerably. This approximation is known as the *quasi-static limit*, because it is possible to replace electrodynamics treatment with electrostatics. Neglecting phase retardation and effects of higher multimodes ($L = 1$)

and further knowing that a_L and b_L are proportional to $(|\boldsymbol{k}|R)^{2L+1}$) leads to:

$$\sigma_{ext} = 9|\boldsymbol{k}|\epsilon_m V_0 \frac{\epsilon_2(\omega)}{[\epsilon_1(\omega) + 2\epsilon_m(\omega)]^2 + \epsilon_2(\omega)^2} \tag{1.9}$$

where $V_0 = (4\pi/3)R^3$ denotes the particle volume, ϵ_m is the dielectric function of the embedding medium, and $\epsilon = \epsilon_1 + i\epsilon_2$ is the dielectric function of the particle material. ϵ can be expressed also using the susceptibility χ as $\epsilon = 1-(4\pi/e^2)\chi$. Since the higher multimodes were neglected and the scattering cross section is strongly suppressed in a given size region, this extinction cross section (1.9) is due to dipolar absorption only. It has a resonance at the frequency where the denominator $[\epsilon_1(\omega) + 2\epsilon_m(\omega)]^2 + \epsilon_2(\omega)^2$ has its minimum. If $\epsilon_2(\omega)$ is small or does not change significantly in the vicinity of the resonance, then the condition can be simplified to $\epsilon_1(\omega) = -2\epsilon_m$. This condition can be fulfilled especially by metals, but in practice only a few of them, like the alkali and noble metals as well as aluminum, exhibit sharp resonances. One of the possible reasons is that $\epsilon_2(\omega)$ is not always small in the vicinity of the resonance, causing significant dampening and broadening of the resonance. The position and shape of the resonance of equation (1.9) is not directly dependent on the particle radius R. However, such dependence is hidden in the size dependencies of $\epsilon_{1,2}(\omega, R)$. This gives the opportunity to use the resonance frequency, amplitude and width to study the size dependence of the dielectric functions. It is clear from the resonance condition, that the surrounding medium and its dielectric function ϵ_m play an important role in determining the resonance frequency. It is actually one of the parameters that can be used to shift the resonance position in a desired direction.

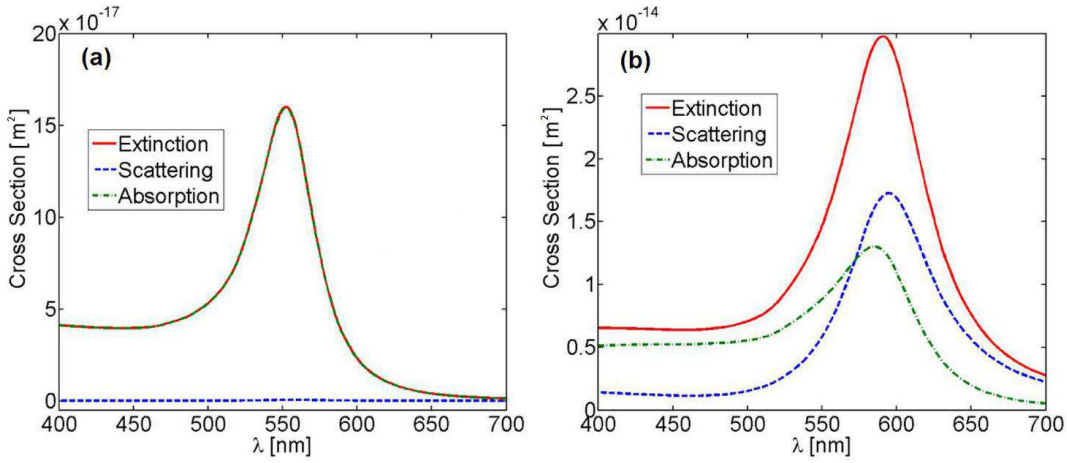

Figure 1.1: Contributions of scattering and absorption cross sections to total extinction cross section for two nanoparticles of radii ((a)$R = 5nm$, (b)$R = 30nm$) of Au nanoparticles in Al_2O_3 matrix. Mie theory calculation using Matlab code.

For particle radius above 10 nm, the retardation of the fields across the particle and effects of higher multipoles ($L > 1$) come into play, so a simple equation defining the resonance condition such as equation (1.9) is not readily available. With increasing size of the particles, the scattering causes significant shifts, broadening, and increase of the amplitude of the extinction cross section due to the increasing particle volume. This is clearly visible in Fig. 1.1, which shows a comparison of extinction cross section and the contributing absorption and scattering cross sections between two Au nanoparticles with radii 5 and 30 nm in Al_2O_3 matrix (Fig. 1.1(a) and (b), respectively). In practice, it is difficult to prepare samples of monodisperse particles. Consequently the width of the size distribution induces additional broadening of the resonance. The effect of a broad size distribution is that the extinction spectra are dominated by the largest, strongly scattering particles. One of the best techniques for

producing nearly monodisperse particles is colloidal chemistry; most other techniques produce size distributions of considerable width. In order to fit the experimental data well, realistic size distributions have to be used in the Mie-theory calculations. The Gaussian distribution, also called the normal distribution, is usually used if the size distribution of the particles is symmetric.

There have been several extensions made to the Mie-theory after it was developed in 1908. The first thing considered was different nanoparticle shapes[7]. The simplest extension of a spherical shape is an ellipsoid. Electrodynamic treatment of this shape is still possible. The main parameters of the ellipsoid are the three principal-axis lengths. These determine the optical resonances, so it is possible to obtain up to three resonances for an arbitrary ellipsoid, while their magnitude depends on the polarization direction of the incident light with respect to a given axis. For many samples, these resonances are not separated in the measured spectrum, but both red and blue shifts with respect to the classical Mie resonance of a sphere are possible. For particle shapes other than spheres and ellipsoids, it is usually not possible to obtain analytical solutions to the Maxwell equations. Therefore, there has been a great effort to develop numerical methods that would be able to solve them for an arbitrary particle shape. Discrete dipole approximation (DDA)[8, 9], multiple multipole (MMP)[10] and T-matrix[11, 12] are some of the numerical methods that have been successfully used to describe non-spherical metal particles. For example, in the DDA approach, the object of interest is divided into a large number of polarizable cubes. Since there is no restriction on which cubes are occupied, this method can be applied to an object or multiple objects of any shape. The induced dipole polarizations in

the cubes are determined self-consistently, and then the extinction cross section can be determined in terms of the induced polarizations. The DDA method can also be applied to so-called core-shell particles. These are particles composed of a core made of one material and a shell made of a different material. Since core and also shell materials can be dielectrics, semiconductors or metals and the number of shells is not limited, a broad variety of interesting materials can be thus designed.

The theoretical modeling of nanoparticle optical properties is easiest with just a single particle. However, in order to get a measurable signal from a sample, it is usually necessary that the sample contain large number of particles ($> 10^{10}$)[13]. Consequently, in such samples it is possible that the particles are close enough to each other that their mutual influence cannot be neglected. Once the particles are not independent, the properties of the system will differ more or less from the sum of individual particle properties. Generalized Mie theory (GMT) is usually applied to such systems. The calculation is based on the single-particle case of the Mie theory, which is generalized to include the electromagnetic near-field coupling among all the particles of the sample at their real positions. It has been shown that the particular geometric arrangements of the particles can dramatically influence the Mie resonances, so that it can broaden and even split them into several peaks[14].

There are two more important extensions to Mie theory; those are the near-field and nonlinear optical properties of metal nanoparticles. Concerning the near-field properties, it was calculated that the electric fields close to the $R = 30nm$ spherical metal nanosphere are enhanced compared to the field in the absence of the sphere by factor of nearly 100 at the resonance peak wavelength[1]. This has

applications in surface-enhanced Raman spectroscopy (SERS)[15] where molecules on the surface interact with the incident field. Since the field is enhanced at the sphere surface, it induces a stronger oscillating dipole in the molecule. The radiation from that dipole, which also interacts with the surface, results in Raman scattering. The enhanced surface fields also strongly increase nonlinear effects, such as second-harmonic generation (SHG), or third-order effects, such as the Kerr effect. All these effects greatly contributed to the interest in the research field of metal nanoparticles.

1.2.1.2 Dielectrics

The two dielectrics used in this work are SiO_2 and Al_2O_3. In the case of SiO_2, it is more precise to talk about fused silica, which is our most common substrate material. Fused silica is a high-purity, synthetic silicon dioxide that is noncrystalline. Due to its broad transmission range from 0.2 up to 3 μm, it is widely used in optical applications. Significant mid-infrared absorption in SiO_2 starts at wavelengths around 6 μm and peaks at 9.6 μm; the absorption is caused by the excitation of Si-O vibrational modes. Similar mid-infrared absorption bands are observed in other dielectrics and are usually described well by a multiphonon absorption model[16].

In our experiments, we have the crystalline form of Al_2O_3, sapphire, and the amorphous Al_2O_3. Al_2O_3 substrates are always sapphire and the deposited Al_2O_3 films are amorphous. Sapphire, also known as α-Al_2O_3, is the only thermodynamically stable oxide of aluminum [17], and crystallizes in the hexagonal-rhombohedral system. Its structure can be viewed as hexagonal closest packing of oxygen ions forming layers parallel to the (0001) plane, while the interstices between the oxygen layers accom-

modate Al^{3+} ions. Only two-thirds of the octahedral interstices are occupied by Al^{3+} ions to maintain charge balance. Sapphire can be synthesized by both thermal and hydrothermal methods. For example, the Verneuil method can be used for preparation of large single crystals, including gem-quality sapphire and ruby crystals[18]. Single crystals of appreciable size can be also grown from melts containing lead fluoride or cryolite. Sapphire is often used in optical applications because of its strength, hardness and broad transmission wavelength range from 0.15 to 5 μm. Some of the basic physical properties of sapphire and fused silica are compared in Table I.1[19].

Table I.1: Properties of Al_2O_3 and a-SiO_2, comparison.

	Al_2O_3	**a-SiO_2**
Density [g/cm^3]	3.98	2.2
T$_{Melting}$ [K]	2327	1740
Thermal Conductivity [W/m.K]	35.1 (at 300K)	10.7 (at 323K)
Thermal Expansion [K^{-1}]	5.6x10^{-6} (at 298K)	0.52x10^{-6} (at 278-308K)
Specific Heat [cal/g.K]	0.18 (at 298K)	0.17 (at 273K)
Bandgap E$_g$ [eV]	9.9	8.4
Refractive index n	1.77 (at 550nm)	1.46 (at 550nm)

1.2.2 Modification of composite materials

Nanocomposite materials can be fabricated using various deposition techniques described in more detail in experimental chapter. It is often desired to modify and tailor their properties further after deposition. One of the post-processing techniques

widely used for such modification is laser annealing. Its effects on the composite materials have been studied extensively [20, 21, 22, 23, 24, 25, 26, 27, 28, 29, 30, 31]. The laser wavelength, fluence and pulse duration are the usual variable parameters of the laser annealing experiments. In most previous experiments, the laser wavelength is in a spectral region where the dielectric matrix is transparent, so that the laser light is primarily absorbed by the metal nanoparticles. There are also several experiments [25, 27, 31, 32] that make use of matrix absorption in the ultraviolet (UV) wavelength region. Surprisingly, before our work was published, there were no reported experiments on the effects of laser light in the infrared absorption region of the dielectric matrices.

Our results show that infrared (IR) laser annealing successfully modified nanocomposites consisting of Au and Ag nanoparticles embedded in a fused silica or Al_2O_3 matrix. The experiments demonstrate the unique effects of fast thermal heating of the matrix on the size and size distribution of embedded metal nanocrystals, using photons with energies far below the bulk bandgap of the matrix. We find that the ambient environment has no influence on the IR laser-induced ripening. The process differs from that found in UV laser annealing of transparent substrates, where most of the laser energy is absorbed by the nanoparticles and nanoparticle ripening is assisted by free-electron heating. Also in case of silicate glasses[33], where there is strong matrix absorption of UV light, the primary interaction is non-thermal, such as electron-hole pair creation followed by thermalization processes. However, what we have demonstrated is true rapid *thermal* annealing, where the nanocomposite material is fully in thermal equilibrium. This opens the door to direct writing of waveguides

and other interesting structures in metal-dielectric nanocomposites. In addition, since the optical penetration depth in many dielectrics such as fused silica and Al_2O_3 is a strong function of wavelength in the 7-10 μm region, the infrared laser annealing can be easily used to control annealing depth in these nanocomposites [34, 35].

1.3 Coherent phonons

A phonon is a collective vibration of the atoms in a crystalline solid. Many physical properties of solids, including thermal and electrical conductivities, are determined and strongly influenced by phonons. In insulators, phonons are the primary mechanism of heat conduction. They are also responsible for the sound in solids, particularly the long-wavelength acoustic phonons. Coherently excited acoustic phonons are used in depth-profiling measurements[36, 37]. The advantages of these measurements are high sensitivity, applicability to opaque materials, and non-destructive. Lasers are commonly used to generate and detect coherent phonons (sound waves) through photoacoustic effect, which can be a result of several different processes such as electrostriction in polarizable materials, thermal expansion, ablation and breakdown[38].

Time-resolved pump-probe spectroscopy utilizes pulsed lasers and the lock-in noise reduction technique, and is often used in photoacoustic measurements due to its high-sensitivity. The samples studied using this technique are not only simple, single-material films[39, 40, 41, 42, 43], but also multilayer structures of various compositions[44, 45, 46, 47, 48, 49, 50]. The longitudinal sound velocity, phonon attenuation, electron diffusion, electron-electron and electron-phonon scattering are some of the properties studied in the simple films. In the case of multilayer films,

the effective elastic constant and sound velocity were examined. The multilayers are usually composed of two material films alternately deposited on a substrate, thus creating a periodic superlattice. The periodicity of these structures causes folding of the phonon dispersion curve, which gives rise to minibranches separated by gaps at the zone boundaries. The band gaps are a direct consequence of the difference in elastic properties of the constituent layers and represent a frequency region in which no propagating phonon modes exist. However, theory predicts that localized surface modes can exist in the gaps when the superlattice is semi-infinite[51, 52].

In metallic superlattices[49, 53, 54], softening of the longitudinal elastic constant with decreasing thickness $d_{1,2}$ of the constituent layers was observed. A similar effect was observed also in a metal/dielectric superlattice[46, 55]. This elastic anomaly is generally ascribed to interfacial effects, however there are studies where no such anomaly in metal/dielectric system is observed[56].

1.3.1 Coherent acoustic phonon modes in superlattices

1.3.1.1 Modes of an infinite superlattice

The superlattice structure under consideration is made up of alternating layers of two different materials of thicknesses d_1 and d_2, densities ρ_1 and ρ_2 and longitudinal sound velocities v_1 and v_2 (Fig. 1.2). Since the dimensions of the laser-pulse excited area are significantly greater then the thickness of the multilayer, only the motion in normal z direction to the surface needs to be considered. Thus the problem becomes

one dimensional and the equation of elasticity is

$$\rho(z)\frac{\partial^2 u(z,t)}{\partial t^2} = \frac{\partial \sigma(z,t)}{\partial z}, \tag{1.10}$$

where u is the displacement in the z direction, and σ is the zz component of the elastic stress tensor which is related to u by

$$\sigma(z,t) = \rho v^2 \eta(z,t) = \rho v^2 \frac{\partial u(z,t)}{\partial z}. \tag{1.11}$$

$\eta(= \partial u/\partial z)$ is the zz component of the elastic strain tensor and v is longitudinal sound velocity. We look for a traveling wave solution in the form

$$u(z,t) = u(z)e^{-i\omega t}. \tag{1.12}$$

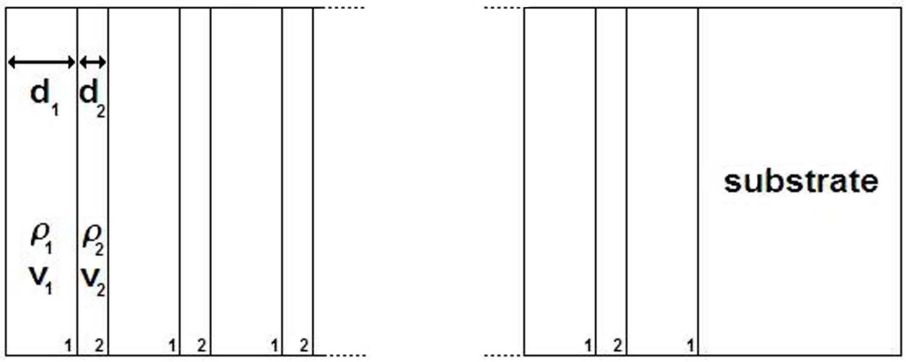

Figure 1.2: Schematic of the superlattice structure.

Let the mth layer of the multilayer begin at $z = z_m$. Then the general solution of

the wave equation in this layer can be written in the form

$$u(z) = A_m \sin[k_m(z - z_m)] + B_m \cos[k_m(z - z_m)], \tag{1.13}$$

where A_m and B_m are amplitudes and k_m is equal to ω/v_1 or ω/v_2 depending on the layer. The displacement and the stress must be continuous at any interface between two layers; these boundary conditions therefore relate A_{m+1} and B_{m+1} to A_m and B_m, and so on. It is possible to express the propagation of the fields across a bilayer with the use of a transfer matrix T defined by[51, 52, 48]

$$\begin{bmatrix} A_{m+2} \\ B_{m+2} \end{bmatrix} = T \begin{bmatrix} A_m \\ B_m \end{bmatrix}. \tag{1.14}$$

The elements of T are

$$T_{11} = a_1 a_2 - p^{-1} b_1 b_2, \tag{1.15}$$

$$T_{12} = -b_1 a_2 - p^{-1} a_1 b_2, \tag{1.16}$$

$$T_{21} = b_1 a_2 - p a_1 b_2, \tag{1.17}$$

$$T_{22} = a_1 a_2 - p b_1 b_2, \tag{1.18}$$

where $a_1 = \cos(k_1 d_1)$, $a_2 = \cos(k_2 d_2)$, $b_1 = \sin(k_1 d_1)$, $b_2 = \sin(k_2 d_2)$, and $p = Z_1/Z_2$, where $Z_i = \rho_i v_i$ is acoustic impedance. It can be shown that $\det T = 1$, so the eigenvalues of T must be expressible in the form $(e^{i\theta}, e^{-i\theta})$. Applying Bloch's theorem for a propagating mode in this infinite superlattice, it is natural to define θ in the

form

$$\theta = qd, \tag{1.19}$$

where q is the wave number, and $d = d_1 + d_2$ is the repeat distance. The trace of T is then

$$T_{11} + T_{22} = e^{iqd} + e^{-iqd} = 2\cos(qd). \tag{1.20}$$

This leads to the dispersion relation

$$\cos(qd) = \cos\left(\frac{\omega d_1}{v_1}\right)\cos\left(\frac{\omega d_2}{v_2}\right) - \frac{(1+p^2)}{2p}\sin\left(\frac{\omega d_1}{v_1}\right)\sin\left(\frac{\omega d_2}{v_2}\right). \tag{1.21}$$

which was first derived by Rytov[57]. It describes well the folding of the acoustic branch of the phonon spectrum in the superlattices. An example of the dispersion curve for an Au(5 nm)/Al_2O_3(45 nm) superlattice is shown in Fig.1.3. Parameters employed are the bulk values $\rho_2 = 19.3$ g/cm^3, $v_2 = 3.2$ nm/ps, $\rho_1 = 3.97$ g/cm^3 and the experimentally obtained velocity $v_1 = 7.3$ nm/ps. The real solutions of Eq. (1.21) are bulk modes, which propagate within the multilayer structure with an effective sound velocity $v_{\mathbf{eff}}$. An expansion of the dispersion relation as qd goes to zero (eqv. $\omega \to 0$) gives the following expression for $v_{\mathbf{eff}}$[42]

$$v_{\mathbf{eff}} = d\left(\frac{d_1^2}{v_1^2} + \frac{d_2^2}{v_2^2} + \left(\frac{(1+p^2)}{p}\right)\frac{d_1 d_2}{v_1 v_2}\right)^{-\frac{1}{2}}. \tag{1.22}$$

Note in Fig.1.3 the existence of frequency band gaps, in which the solution of Eq. (1.21) is imaginary and so no propagating phonon modes are allowed.

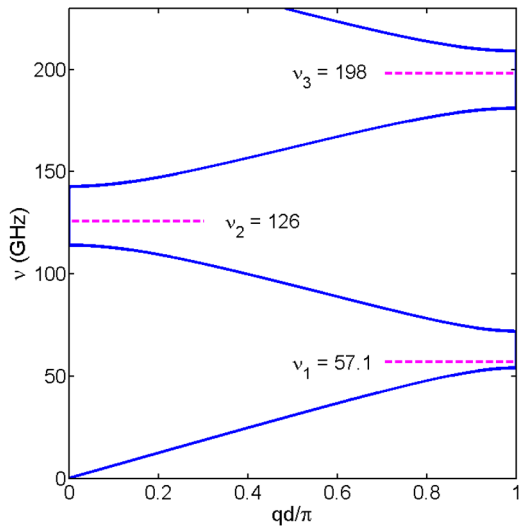

Figure 1.3: Dispersion of longitudinal acoustic phonons in a Au(5 nm)/Al_2O_3(45 nm) superlattice with first three surface modes marked with a dashed line.

1.3.1.2 Surface modes - case of a semi-infinite superlattice

Consider now a semi-infinite superlattice with a free surface at $z = 0$. In addition to the bulk modes of the infinite multilayer, the free surface makes surface-mode solutions possible. The subscript 1 refers to the material of top layer, as in Fig. 1.2. To derive the conditions of a surface mode, suppose the eigenvectors of T are $\phi^{(1)}$ and $\phi^{(2)}$[44]. The amplitudes A_1, B_1 in the first layer can be expressed in the form

$$\begin{bmatrix} A_1 \\ B_1 \end{bmatrix} = C_1\phi^{(1)} + C_2\phi^{(2)}, \tag{1.23}$$

Then in the $(2n+1)$st layer the amplitudes are

$$\begin{bmatrix} A_{2n+1} \\ B_{2n+1} \end{bmatrix} = C_1\lambda_1^n\phi^{(1)} + C_2\lambda_2^n\phi^{(2)}, \tag{1.24}$$

where λ_1 $(= e^{iqd})$ and λ_2 $(= e^{-iqd})$ are the eigenvalues of T. For these amplitudes to vanish for large n, q must be complex. In the case Im(q)>0, then $|\lambda_1| < 1$ and $|\lambda_2| > 1$. From (1.24), it is necessary that $C_2 = 0$, which means that the amplitudes (A_1, B_1) must be an eigenvector of T corresponding to the eigenvalue λ_1. Equation (1.13) together with the boundary condition of vanishing stress at the free surface leads to $A_1 = 0$. Consequently, the conditions for the existence of a surface mode are that the transfer matrix T has an eigenvector (0,1), and the magnitude of its associated eigenvalue is less then 1. The eigenvector requirement is equivalent to the condition $T_{12} = 0$, which gives[48, 44, 51]

$$p\tan(\omega d_1/v_1) + \tan(\omega d_2/v_2) = 0. \tag{1.25}$$

The surface mode frequencies are the solutions of this equation. Further, $\lambda_1 = T_{22}$ so that

$$\lambda_1 = \frac{\cos(\omega d_1/v_1)}{\cos(\omega d_2/v_2)}. \tag{1.26}$$

If $p < 1$ it can be shown that, for all frequencies which are solutions of Eq. (1.25), $|\lambda_1| < 1$ as required. However, if $p > 1$, $|\lambda_1| > 1$ always holds so there are no surface modes. Hence, surface modes exist only when the acoustic impedance of the first

layer ($\rho_1 v_1$) of the superlattice is smaller than the impedance of the second layer. The eigenvalue λ_1 is related to the exponential decay length l of the surface mode by[44]

$$l = -d/\ln(|\lambda_1|). \tag{1.27}$$

The surface mode frequencies calculated using Eq. (1.25) are marked with dashed horizontal lines in Fig. 1.3.

1.3.1.3 Excitability and detectability of the normal modes

Pu[47] derived expressions for the excitability and detectability of normal vibration modes. Looking for a solution to the elasticity equation in the form $u(z,t) = u_n(z)e^{-i\omega_n t}$, Eqs. (1.10) and (1.11) become

$$-\omega_n^2 \rho(z) u_n(z) = \frac{d}{dz}\sigma_n(z). \tag{1.28}$$

The ω_n and $u_n(z)$ are the eigenvalues and eigenfunctions of Eq. (1.28). The boundary conditions of continuity of displacement and stress at all interfaces apply here as well, thus the frequencies ω_n also obey the Rytov dispersion relation Eq. (1.21). It can be shown[47] that functions $\{u_n\}$ form a complete set, and so any arbitrary function can be expanded in these normal modes.

An ultrafast laser pulse generates a thermal stress $\sigma_T(z,t)$ within the superlattice[39]

$$\sigma_T(z,t) = -3B\beta\Delta T(z,t), \tag{1.29}$$

where B and β are the bulk modulus and the coefficient of thermal expansion, respectively. ΔT is the temperature rise induced by the laser. This modifies Eqs. (1.11) and (1.10) to

$$\sigma(z,t) = \rho v^2 \eta(z,t) = \rho v^2 \frac{\partial u(z,t)}{\partial z} + \sigma_T(z,t) \tag{1.30}$$

and

$$\rho(z)\frac{\partial^2 u(z,t)}{\partial t^2} = \frac{\partial}{\partial z}\left(\rho(z)v^2(z)\frac{\partial u(z,t)}{\partial z}\right) + \frac{\partial \sigma_T(z,t)}{\partial z}. \tag{1.31}$$

The thermal stress term in Eq. (1.31) represents a distributed-body force, which initiates the superlattice vibrations. The solution $u(z,t)$ can be expanded in a series of normal modes:

$$u(z,t) = \sum_n a_n(t) u_n(z). \tag{1.32}$$

The time-dependent coefficients $a_n(t)$ embody the time-varying character of the expansion needed to represent $u(z,t)$. The expansion is substituted into Eq. (1.31) and then applying Eq. (1.28) together with the orthogonality and normality relations, gives

$$\frac{\partial^2 a_n(t)}{\partial t^2} + \omega_n^2 a_n(t) = Q_n(t), \tag{1.33}$$

where

$$Q_n(t) = \int \frac{\partial \sigma_T(z,t)}{\partial z} u_n(z) dz. \tag{1.34}$$

Eq. (1.33) is simply the equation of motion for a harmonic oscillator driven by a time-varying force. The driving force $Q_n(t)$ is the overlap integral of the distributed-body force $\partial\sigma_T(z,t)/\partial z$ with the eigendisplacement $u_n(z)$. Integration by parts recasts it

into[47]

$$Q_n(t) = -\int \sigma_T(z,t)\eta_n(z)dz. \tag{1.35}$$

This spatial overlap integral evaluates the degree of waveform matching between the thermal stress σ_T and the strain pattern of the normal modes, and defines the optical *excitability* by ultrafast lasers for each normal mode. It is important to note that the coefficients of excitation $a_n(t)$ are affected by the temporal profile as well as the spatial pattern of the thermal stress. If the thermal stress were set up instantaneously, this step-like process would produce equal excitation amplitudes for all the frequencies ω_n that can be excited. However, in reality the establishment of the thermal stress is slowed down by energy transfer from electrons to phonons. This causes the excitation amplitude to diminish rapidly as the phonon frequency increases.

To calculate the photoelastic response $\Delta R(t)$, the strain wave solution $\eta(z,t)$ is multiplied by the depth dependent "sensitivity function" $f(z)$ and integrated over the entire superlattice:[44, 39]

$$\Delta R(t) = \int \eta(z,t)f(z)dz. \tag{1.36}$$

Applying the normal mode expansion gives

$$\Delta R(t) = \int \left(\sum_n a_n(t)\eta_n(z)\right) f(z)dz = \sum_n a_n(t)F_n, \tag{1.37}$$

where

$$F_n = \int \eta_n(z)f(z)dz. \tag{1.38}$$

F_n is a spatial overlap integral between the strain pattern η_n and the optical sensitivity function $f(z)$. It represents the optical *detectability* for each mode.

The sensitivity function $f(z)$ determines how strain at different depths below the surface of the superlattice contributes to the change in reflectivity $\Delta R(t)$. It was originally derived by Thomsen *et al.* correct to first order in the strain:[39]

$$f(z) = f_0 \left[\frac{\partial n}{\partial \eta} \sin \left[\frac{4\pi n z}{\lambda} - \phi \right] + \frac{\partial \kappa}{\partial \eta} \cos \left[\frac{4\pi n z}{\lambda} - \phi \right] \right] e^{-z/\zeta}, \tag{1.39}$$

where

$$f_0 = 8 \frac{\omega [n^2(n^2+\kappa^2-1)^2 + \kappa^2(n^2+\kappa^2+1)^2]^{1/2}}{c[(n+1)^2+\kappa^2]^2}, \tag{1.40}$$

$$\tan \phi = \frac{\kappa(n^2+\kappa^2+1)}{n(n^2+\kappa^2-1)}. \tag{1.41}$$

Here λ is the wavelength of light in free space, n and κ are the real and imaginary parts of the index of refraction, ζ is the absorption length ($\zeta = \alpha^{-1} = c/2\omega\kappa$), and ϕ lies between 0 and $\pi/2$. The general form of f is an exponentially-damped oscillation with nonzero phase at the surface $z = 0$; the periodicity of f is half the wavelength of light in the material, and $\partial n/\partial \eta$ and $\partial \kappa/\partial \eta$ are the photoelastic constants. They are wavelength dependent and not readily available even for many basic materials. For Au, we assume $\partial n/\partial \eta = \partial \kappa/\partial \eta$[40] and using Garfinkel's[58] piezoreflectivity data we estimate that $\partial n/\partial \eta < 10^{-3}$. This value of the Au photoelastic constant is much smaller than those of some other metals such as Ni and Cr[59]. However, in the multilayers we studied it is also important to know the photoelastic constant of Al_2O_3. Since $\partial n/\partial \eta$ of amorphous Al_2O_3 is not known, a calculation of $\Delta R(t) =$

$\int \eta(z,t)f(z)dz$ was performed while varying the ratio of the photoelastic constants of Au and Al_2O_3.

In order to observe the oscillatory signal in calculated $\Delta R(t)$ as in the experiment, the photoelastic constant of Al_2O_3 have to be smaller then for Au. Fig. 1.4(a) shows the sensitivity function calculated with the ratio $(\partial n/\partial \eta_{Au})/(\partial n/\partial \eta_{Al_2O_3}) = 5$. It also shows the strain patterns of the first two surface modes of Au(5 nm)/Al_2O_3(45 nm) superlattice (Fig. 1.4(b),(c)) demonstrating their spatial extension into the superlattice. The overlap integral between the strain patterns and the sensitivity function above define the detectability which is calculated numerically using such data.

The function $\Delta R(t) = \int \eta(z,t)f(z)dz$ accounts for the bulk photoelastic effect. However, it was shown by Matsuda *et al.*[60] that in case of semitransparent multilayers, the motion of the interfaces can make equally important contribution to $\Delta R(t)$. The reflectance change due to the motion of interfaces is given by

$$\sum_{j=1}^{N+1} E_j^2[\epsilon^{(j-1)} - \epsilon^{(j)}]u(z_{j-1}), \tag{1.42}$$

where $\epsilon^{(j-1)}$ and $\epsilon^{(j)}$ are the dielectric constants of the (j-1)th and the jth layer, respectively. z_{j-1} is the z coordinate of the (j-1)th interface. E_j is the total electric field at that interface and N is the number of periods in the superlattice. The contribution of interface motion is obviously proportional to the difference in the dielectric constants of adjacent layers. In order to be able to distinguish whether the bulk photoelastic effect or the interface motion is dominant, the precise values of the photo elastic constants need to be known.

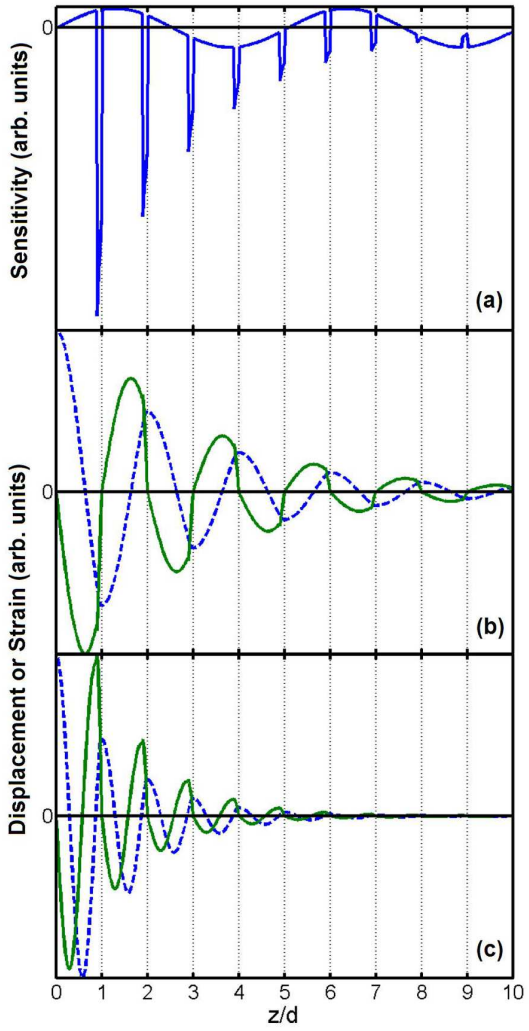

Figure 1.4: The optical sensitivity function $f(z)$ of Au(5 nm)/Al_2O_3(45 nm) superlattice (a). The strain (full line) and displacement (dashed line) patterns of the first (b) and the second (c) surface mode.

Overall, the theory can describe the phonon dispersion relation in superlattice structures very well. However, due to the fact that we are unable to deconvolute the contributions from the photoelastic effect and interface motion, we cannot use our experimental data to estimate the photoelastic constants of the constituent materials of the superlattices.

CHAPTER II

EXPERIMENTAL TOOLS AND TECHNIQUES

The preparation methods of composite materials, together with the annealing, characterization and spectroscopy techniques used in this work, are described in this chapter.

2.1 Composite materials - preparation methods

Deposition of a multilayer structure with alternating metal and dielectric matrix layers [61], co-sputtering [62], ion-exchange [63] and ion implantation [2] are some of the most commonly used deposition techniques for preparing metal/dielectric composites.

2.1.1 Implantation

Ion implantation is a widely used and versatile method due to its ability to incorporate nearly any material or even any combination of the materials into a given substrate. It is suitable for fabrication of metal nanoparticles in dielectric matrices, in which case implantation is usually followed by annealing to induce phase separation and nanoparticle formation. Figure 2.1 shows a schematic of a typical ion implantation system. Its main parts are the ion source, pre-acceleration section, mass analyzing magnet followed by additional acceleration and finally the target region. Depending on the accelerator system, energies of implanted ions can vary from several

keV up to $\sim$ 10MeV. The implantation energy is one of several important parameters determining the projected range; the other crucial parameters are the mass of the implanted ions and the mass of the target constituent atoms. The projected range is the average depth of the implanted ions and it can be calculated with several available computer programs. A typical calculation using SRIM 2008 is shown in Fig.2.2, for 300 keV Au ions, quartz substrate and 10^5 incident ions. The Au ion concentration profile has a Gaussian shape, which is typical for a single-layer substrate. The calculation can be verified by measuring the concentration profile in a real sample using Rutherford backscattering spectrometry (RBS).

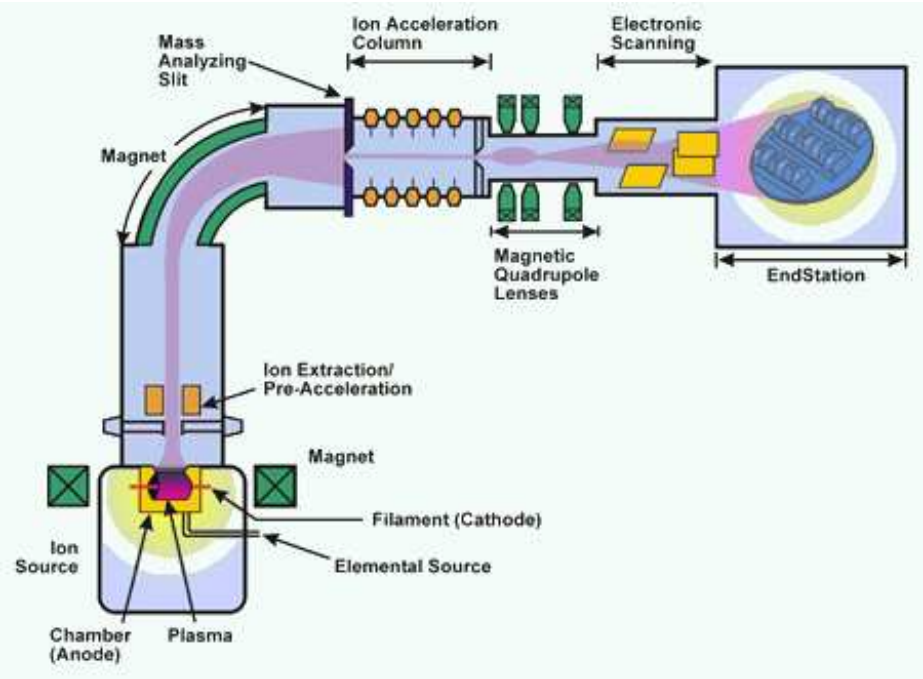

Figure 2.1: Schematic of ion implantation system.

Nuclear and electronic stopping are the two energy loss processes that stop the implanted ion inside the target. Nuclear stopping is caused by collisions of the incoming ion with the target nuclei, while the electronic energy loss is more complicated since there are several dissipation channels, such as direct kinetic energy transfer to target electrons or excitation, even ionization, of target atoms [64]. Several different processes occur in the target during the ion implantation. First of all, many defects are created and target amorphisation is possible at higher ion doses. Another important issue at high ion doses is sputtering, which can significantly influence the concentration profile of the implanted ions, particularly during low-energy implantation. Despite some potential drawbacks associated with these processes, ion implantation has many advantages that make it a viable research and application tool.

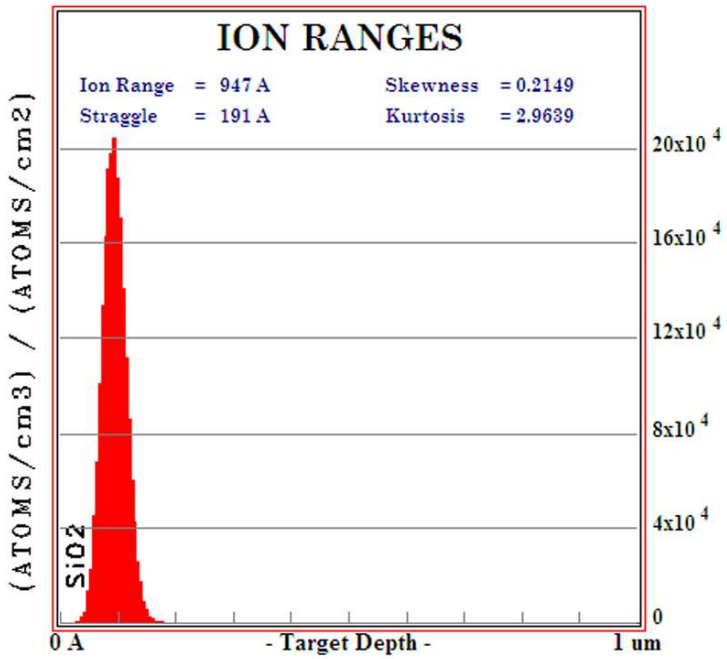

Figure 2.2: Ion range calculation for 300keV Au ions into SiO_2 substrate (10^5 atoms).

In general, the main advantages of ion implantation are the high degree of control over mean implantation depth and concentration, the high purity of the doped (implanted) layer and the possibility to reach high values of the metal-filling factor. While ion implantation offers some unique advantages for the formation of metal nanocrystals (MNCs), Meldrum [65] *et al* have identified two significant problems with MNCs formed using ion implantation. The first is the size distributions of the MNCs formed; the second is the position of the MNCs within the implanted layer. The first effect results from the Gaussian distribution of the implanted ions. Since the SPR spectral position depends on the particle size, the absorption spectrum in a real sample is a superposition of many individual SPR bands which correspond to particles of different sizes. The size dispersion leads to a broadening of the total SPR absorption band accompanied by a decrease in its intensity [3]. One of the ways to make the concentration profile more uniform is to implant metal ions at multiple energies. However, to achieve concentration uniformity over depth range of several hundred nanometers high-energy (MeV) implantation is necessary. Another way to increase uniformity of the size distribution of metal nanoparticles in an ion-implanted dielectric matrix is the use of laser annealing possibly followed by furnace annealing.

In our experiments, Corning 7940 Type III fused-silica substrates were implanted with Au^+ and Ag^+ ions and c-cut sapphire substrate was implanted with Au^+ at Oak Ridge National Laboratory using Tandem and Nova implanters. The silica substrates were kept at 400 °C, while sapphire substrate was kept at liquid nitrogen temperature during implantation. The current densities were maintained below 10 μA. The dose of $6x10^{16}$ ions/cm^2 was the same for both metals in silica samples. The dose of

$12x10^{16}$ Au ions/cm^2 was implanted into Al_2O_3 sample. The implantation energy was 1.1 MeV for Au ions and 305 keV for Ag ions in SiO_2 and 2.75 MeV for Au ions in Al_2O_3. The projected ranges, calculated using SRIM 2008 program, were then 267 nm, 132 nm and 370 nm, respectively.

2.1.2 Physical vapor deposition

The term *physical vapor deposition* covers many deposition techniques, including sputtering, thermal evaporation, electron beam (e-beam) evaporation, pulsed laser deposition and molecular beam epitaxy. All of our multilayer samples were prepared using a system equipped with both thermal and e-beam evaporation at the University of Alberta. The deposition system consists of a bell jar, a vacuum system with a diffusion and rough pump as its main components, an electron beam gun with all the electronics required for its operation, a simpler electronic system for control of the thermal evaporation element and a handful of pressure, temperature and film thickness detectors. An image of the system with the open bell jar is shown in Fig. 2.3(left). The vacuum system is not visible in this image. The right-hand image of Fig. 2.3 shows a close-up view of the e-beam gun with a crucible in the center that contains already melted Al_2O_3; slightly higher and to the left is the shielded tungsten boat used for metal deposition.

Overall, the deposition process is not very fast; on average, only two samples were prepared per day. The deposition steps are as follows. First, the bell jar is vented and opened. Two substrates are mounted onto the sample holder. The samples are placed far enough from each other so that the shutter can be used to cover one of

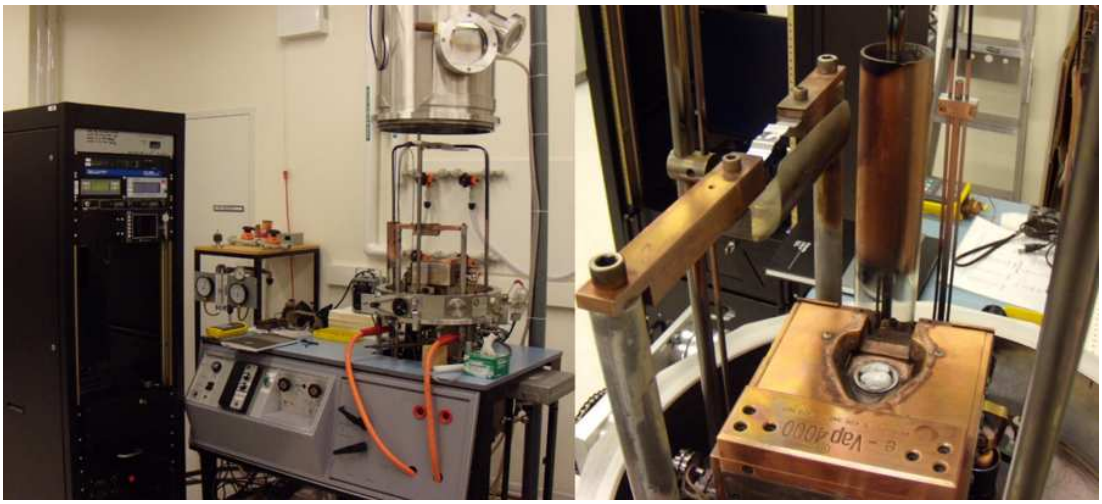

Figure 2.3: Left: Image of the whole deposition system with the bell jar open. Right: Closer look at the electron beam gun and the tungsten boat.

them during certain stages of deposition. The crucible of the e-beam gun is filled with pellets of high purity aluminum oxide (99.99% Al_2O_3, K. J. Lesker). The tungsten boat is mounted between two posts capable of carrying high current and then filled with small pellets of the used metal (99.999% Au or 99.99% Ag, both K. J. Lesker). A small metal plate is mounted under the boat to prevent the deposition of Al_2O_3 onto it. Operation and lifetime of two quartz-crystal microbalance (QCM) detectors is checked before the bell jar is closed. After it is closed, the oil pump is used to bring the vacuum down to the level at which the diffusion pump can be engaged. Even before the valve between the chamber and the diffusion pump is opened, the cold trap above the pump has to be cooled down to liquid nitrogen (LN) temperature. The cold trap improves the vacuum quality by freezing out water vapor and has to be refilled with liquid nitrogen every roughly 30 minutes. If not, the pressure inside

the chamber deteriorates quite rapidly.

Once the diffusion pump is at work, it takes around 3 hours to reach optimal vacuum level of 10^{-7} Torr. It is usual to switch on the high-voltage electronics of the e-beam gun roughly half an hour before starting deposition so that it has time to reach its operating temperature and stabilize. The e-beam gun and also the bell jar have to be water cooled during the gun operation due to excessive heating. The beam of electrons from a hot filament is guided using a strong magnetic field onto the material that is being deposited. The electron beam is scanned across a set area. The material inside the crucible must be slowly heated in order to prevent it from *jumping out* due to thermal stress. Before deposition begins, the Al_2O_3 pellets are first melted and kept at high temperature for couple of minutes so that the material can degas. During this process, the pressure can rise to 10^{-4} Torr, and it is necessary to watch the melting Al_2O_3 using welding safety glasses. When the pressure drops below 10^{-6} Torr, the Al_2O_3 is heated up further until the QCMs detectors read non-zero rate of deposition. This rate can be set to a desired value by tweaking the e-beam gun controls, usually 0.2-0.3 nm/s for Al_2O_3 deposition. Once the rate stabilizes, the shutter is moved away from in front of the samples and a film of desired thickness is deposited, and the shutter is then closed again.

In the course of multilayer preparation, the Al_2O_3 film is usually followed by metal layer deposition. The e-beam gun is slowly switched off until no deposition rate is detected,and the tungsten boat is slowly heated up using electrical current. The metal inside eventually melts and starts to evaporate, which is again monitored by QCMs. The settings of QCMs have to be adjusted to each given material in order to obtain

realistic film thickness measurements. The metals are usually deposited at the rate of 0.05 nm/s. The rate is stabilized before the substrates are uncovered. To prepare two different samples in one pump-down cycle, only one sample is uncovered first and a film of certain thickness is deposited. Then both samples are unblocked and an additional film is deposited, after which the shutter is closed again. In this manner, it is possible to prepare two samples with different metal thickness. Similar procedure can be followed also during Al_2O_3 deposition. The current to the tungsten boat is slowly switched off, stoping the metal deposition. The process of the multilayer preparation continues with another Al_2O_3 film deposition followed by another metal film until the desired number of periods is reached. The top and final layer is always Al_2O_3. After the multilayer is finished, the e-beam gun electronics is switched off and the whole system is left to cool down for half an hour. The diffusion pump valve is then closed, the bell jar is vented, opened and the samples are retrieved.

2.2 Annealing techniques

Annealing is a widely used method for processing materials. It is a heating process aimed at achieving the desired modifications of the treated materials. There are several different annealing techniques of which two were used in this work: furnace and laser annealing. The major differences between these two annealing techniques are the duration of annealing, the rate of heating and the affected area. In case of furnace annealing, the process usually takes a few hours and the whole sample is subjected to the same temperature conditions. On the other hand, laser annealing can be as short as a single laser pulse, which is e.g. 4 μs long in case of the free

electron laser. Also since the laser beam can be easily focused, the annealing process can be highly localized, which is advantageous for certain applications where the thermal stress effects need to be minimized. However, this might turn out to be a disadvantage in applications where large areas have to be annealed.

2.2.1 Furnace annealing

Various types of furnaces are used for annealing purposes. A tube furnace was used in this work. Tube furnaces are very versatile, due to the range of annealing temperatures and the availability of control of the type and pressure of the gas inside the tube. The maximum temperature at which a typical tube furnace can operate is around 2000°C, usually limited by the tube material capabilities. For example, a high-purity alumina tube can withstand temperatures up to 1800°C. The annealing process using the tube furnace usually consists of several steps. First, the furnace is heated up to a predefined temperature. The samples are then placed inside the temperature stable region of the tube. The type, pressure and flow of the gas are set. The samples are left inside for a required amount of time, which can vary anywhere from a few minutes up to several hours, possibly even days. After the annealing the samples can be taken out and allowed to cool immediately to room temperature. However, sometimes it is very important to control the cooling process, which is possible using a programmable furnace in which one can set not only the cooling rate, but also the heating rate when needed.

2.2.2 Laser annealing

Laser annealing experiments on composite materials study changes of the shape, size, size distribution, and morphological structure of the metal nanoparticles in metal/dielectric composites. The laser wavelength, pulse duration and power density are typically the variable parameters of these experiments. The common feature of most annealing experiments is that the applied laser light is in a spectral region in which the dielectric matrix is transparent, which means that the laser light is primarily absorbed by the metal nanoparticles. Some experiments even choose a wavelength that is close to SPR of the metal nanoparticles in order to enhance the absorption by the particles, and so the effect on them. On the other hand, there were several experiments that used the laser light at wavelengths of the matrix absorption in the ultraviolet region[25, 27, 31, 32]. For example, when high-power excimer ArF (193 nm) laser pulses were applied to the float glass with silver particles, a decrease in the reflectance intensity was observed[31]. The suggested explanation was that the silver particles in glass can be dissolved, thus creating a new silver-rich metastable glass phase, which can potentially be further processed to precipitate out new silver nanoparticles under well specified and controlled conditions. Even though the excimer laser technique gives a variety of possibilities for controlled change of optical properties of implanted dielectrics, there are still many questions concerning the nature of the interaction of the laser light with the composite materials, and the search for fundamental understanding is a subject of many ongoing studies.

2.2.2.1 UV and visible pulsed laser annealing

Most laser annealing experiments in the UV and visible wavelength range were done on composite materials which contained silver as the metal component. This is probably due to the fact that silver-dielectric (mostly glass) composite may be produced easily by several different techniques such as ion implantation, ion exchange or co-evaporation. The main results of the laser annealing experiments differ based on the parameters of the annealing process. For Ag/silica composites, a dissolution of Ag particles into the glass or their separation into smaller ones is often observed [32]. A change of shape of the Ag particles, which can significantly shift the SPR peak and thus change the color of the sample, have been also observed [66]. Of course, many other metals (e.g. K, Fe, Cu, Au) and various matrices were tested such as Al_2O_3 and polymers. Recently, the effects of laser annealing on semiconducting CdSe nanoparticles in SiO_2 have been reported [25] and particle formation was observed. This shows that the laser annealing process is a versatile method of modifying composite materials, with many variable parameters that can be adjusted to achieve useful and applicable results.

2.2.2.2 Infrared pulsed laser annealing

In the infrared absorption spectral region of the dielectric matrix, the laser light is predominantly absorbed by the matrix rather than metal nanoparticles because of their small volume fraction. The availability of pulsed laser light in wavelength range of 2-10 μm from a free-electron laser provides a unique opportunity of doing experi-

ments to study the effects of the interaction of infrared radiation with the composite materials, in particular the effects of exciting the matrix on the microstructure of imbedded metal nanocrystals.

In our experiment, Au and Ag implanted SiO_2 samples and Au implanted Al_2O_3 were annealed using the infrared laser beam generated by a picosecond free electron laser (FEL) [67]. Our primary wavelength for SiO_2 was 8 μm, at which the metal implanted layer (Fig. 2.4) was well within the $1/e$ absorption length ($\sim$ 3.4 μm). The wavelength of 9 μm was used for laser annealing of the sapphire sample. The absorption coefficient of alumina at 9 μm wavelength is $\sim 10^2$ cm^{-1} [16], so in this case the Au implanted layer was also well within the $1/e$ absorption length. The FEL beam was scanned across the surface of the sample at approximately 1 mm/s (Fig. 2.5). A CaF_2 lens with a focal length of 500 mm was used for focusing. The spot diameter at the surface was $\sim$ 300 μm, allowing for a good overlap of two consecutive macropulses. The energy of individual macropulses was measured in front of the window of the vacuum chamber using Molectron power meter with a pyroelectric sensor. The energy per pulse used for the annealing was in the range from 3 to 10 mJ, and was adjusted by a polarizer. The angle of incidence of the laser beam on target was 45°; the scanning was accomplished using a rotational stage and by rocking the mirror M1. Some annealing experiments were carried out in vacuum, at a pressure of 4.10^{-2} Torr, to compare the effects of infrared laser annealing in air and in vacuum.

The other annealing setup used a 3D motorized stage. The sample was mounted on the stage and scanned in 2D with a stepping speed that provided good overlap of

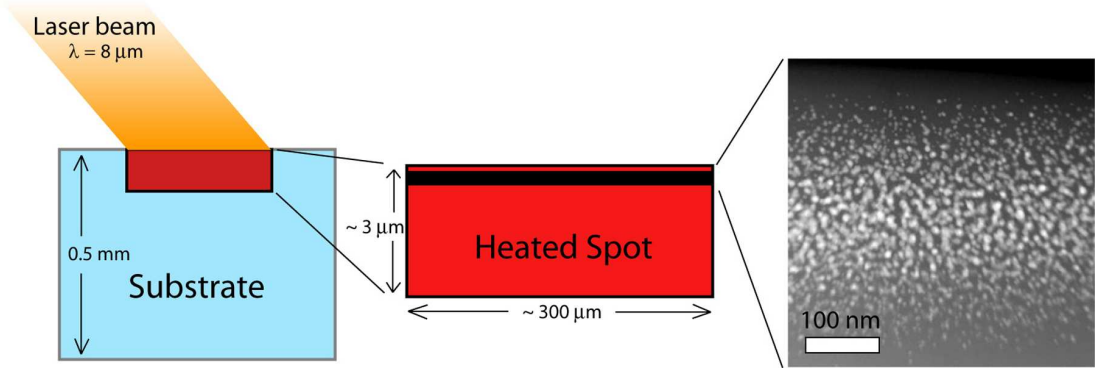

Figure 2.4: Schematic of the metal implanted layer within the laser heated beamspot.

the consecutive pulses. In this setup, the laser beam was stationary and struck the substrate at nearly normal incidence. The beam was focused by a ZnSe lens with a focal length of 125 mm, to a spot diameter $\sim$ 50 μm at the surface. The availability of a small carbon dioxide (CO_2) laser, which operates in continuous wave (cw) mode

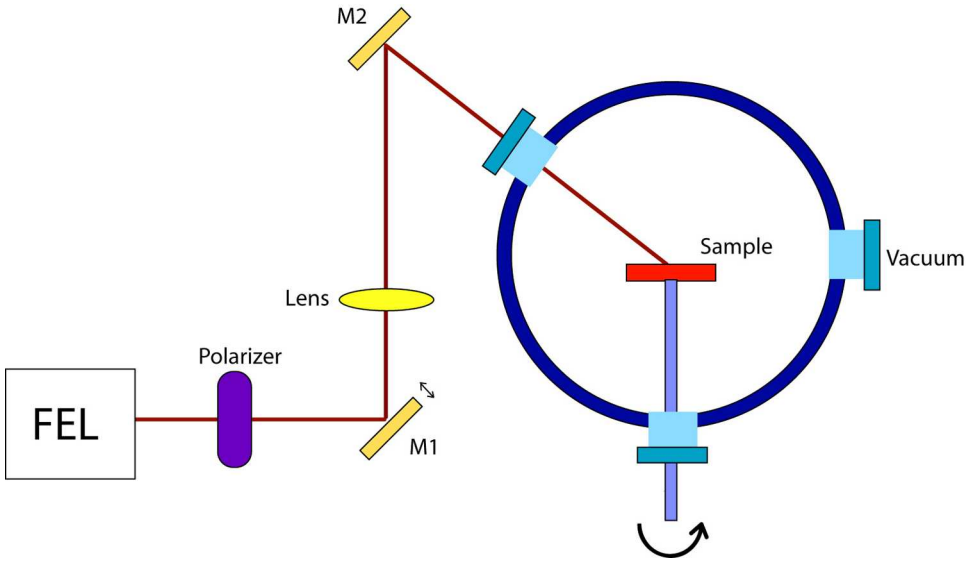

Figure 2.5: Schematic of the free-electron laser annealing setup.

at 10.6 μm wavelength with maximum output power of $\sim$10W, allowed us to perform a few annealing experiments that were compared to the results obtained by pulsed FEL laser annealing.

2.2.2.3 Free-electron laser

The Vanderbilt Mark-III free electron laser (FEL) was used to anneal the samples at different fluences. The FEL is tunable in the mid-infrared from 2 to 10 μm and the spatial mode structure of the emitted IR beam is TEM. The pulse structure of the FEL output beam is defined by the pulse structure of the klystron that powers the relativistic electron beam (Fig. 2.6). The electrons are extracted from a lanthanum hexaboride thermionic cathode by a 2.865 GHz microwave field in a resonant cavity, then passed through an analyzing magnet and introduced into a three-meter long radio-frequency accelerator section. This produces a train of electron pulses which, after compression, are a few picoseconds long and are separated by approximately 350 ps. This train extends for about a 4 μs macropulse at a repetition rate of 30 Hz. The electrons are accelerated to about 43 MeV by the linear accelerator, and traverse a periodic magnetic field (wiggler), in which a spatially periodic magnetic field is created by cobalt-samarium magnets arranged so that their polarities alternate between north and south orientations[67]. Acceleration of the relativistic electrons in the wiggler field leads to emission of electromagnetic radiation strongly peaked in the forward direction; amplification of this radiation occurs by purely classical electromagnetic field effects that bunch the electron beam and lead to additional photon emission.

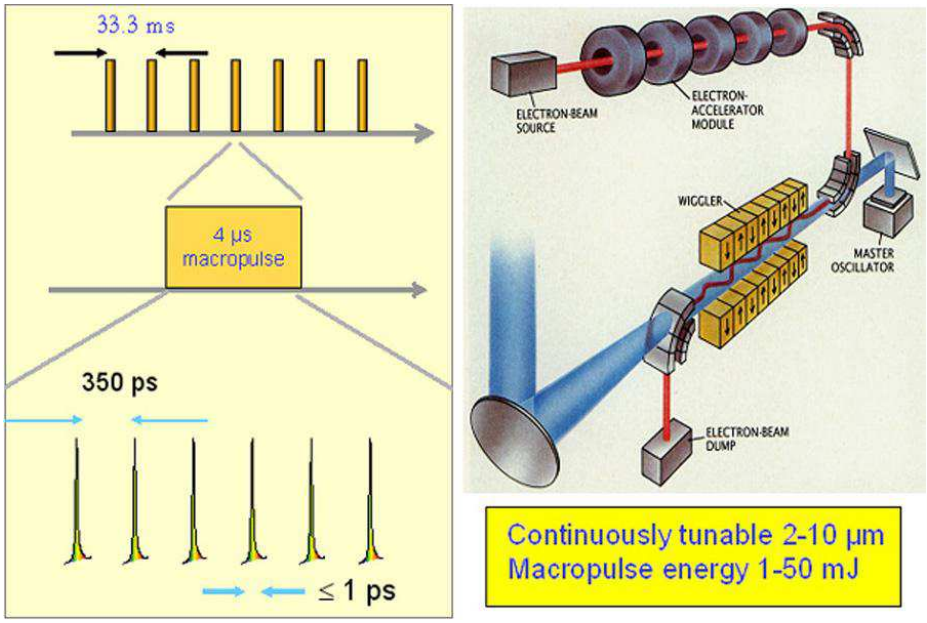

Figure 2.6: Simple schematic of the FEL and its pulse structure.

2.3 Transmission electron microscopy

Transmission electron microscopy (TEM) is a widely used high resolution microscopy technique, using a beam of accelerated electrons that are passed through an ultrathin sample. Transmitted electrons are focused and then projected onto a screen forming an image. Since TEM is very suitable for determining the structure of studied material, it was applied in our work to look at the structure of the superlattices. The requirement of the ultrathin sample is a disadvantage of this technique because sample preparation is a complex and often tedious procedure.

Figure 2.7 shows some of the preparation steps needed to look at the sample in cross-section. The steps precede the actual imaging and quite often they have to be repeated because as the sample gets thinner, it also becomes more fragile and can

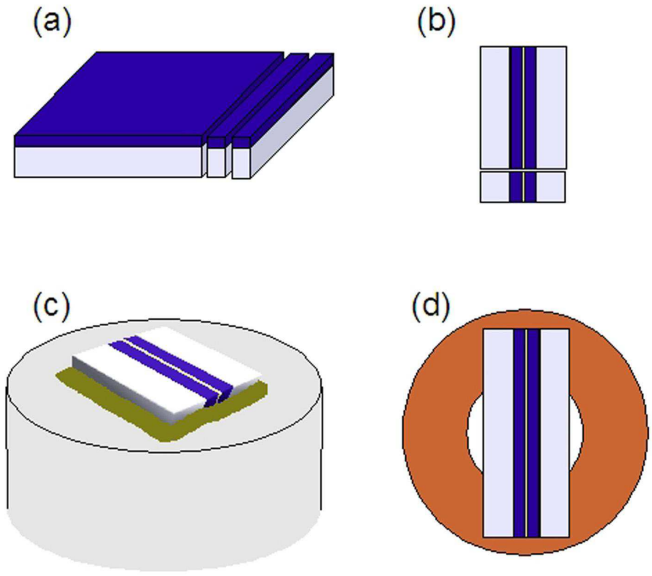

Figure 2.7: Cross-sectional TEM sample preparation steps.

crack easily. At first, two pieces of roughly the same width ($\sim$ 2 mm) are cut from the side of the sample using a diamond saw (Fig. 2.7(a)). These are glued together with multilayer sides facing using an epoxy (Fig. 2.7(b)) and then the resulting structure is cut into $\sim$3 mm bars. The bar is mounted onto a lapping stub using a heat-sensitive wax (Fig. 2.7(c)) and mechanically thinned using a grinder to about 200 μm thickness. The sample is then mounted onto a TEM copper grid (Fig. 2.7(d)) with epoxy, while making sure no epoxy gets into the aperture. The structure is attached to a tripod polisher and the sample is thinned further down to a few micrometers thickness using a diamond impregnated paper with progressively reducing grit size. This is a critical step and the sample has to be checked with a microscope frequently. The final thinning step is a low-angle ion-milling procedure, which can last anywhere

from 15 minutes up to several hours depending on how well the sample was thinned in the previous step. The main advantages of low-angle milling are large thin area, reduced artifacts such as amorphousness and contamination, and applicability to films composed of materials with very different milling speeds, which is especially relevant to our samples. The milling process has to be watched closely as well, because it can easily destroy the sample if applied for too long. The sample is ready when a small hole appears in the center of the sample. The area around the edges of the hole is then thin enough for TEM imaging.

2.4 Time-resolved spectroscopy

Time-resolved spectroscopy, also often referred to as pump-probe spectroscopy, is a powerful experimental technique for studying various relaxation processes in many materials. It is widely used not only in physics, but with diverse adaptations also in chemistry and biology. In this work, the pump-probe technique is used to study the vibrational properties of metal/dielectric superlattices. Figure 2.8 shows a schematic of one of the simpler pump-probe setups measuring differential transient reflectivity ΔR. Pulsed beam coming from a Ti:Sapphire laser is split using a beam splitter (BS) into pump and probe beams.

The pump beam is used to cause excitation in the studied material and thus needs to be on average at least 10 times more powerful then the probe beam at the sample surface. The pump beam is modulated at a particular frequency by an acousto-optic modulator (AOM), which makes it possible to take advantage of the lock-in detection technique, to greatly improve signal-to-noise ratio (SNR). This

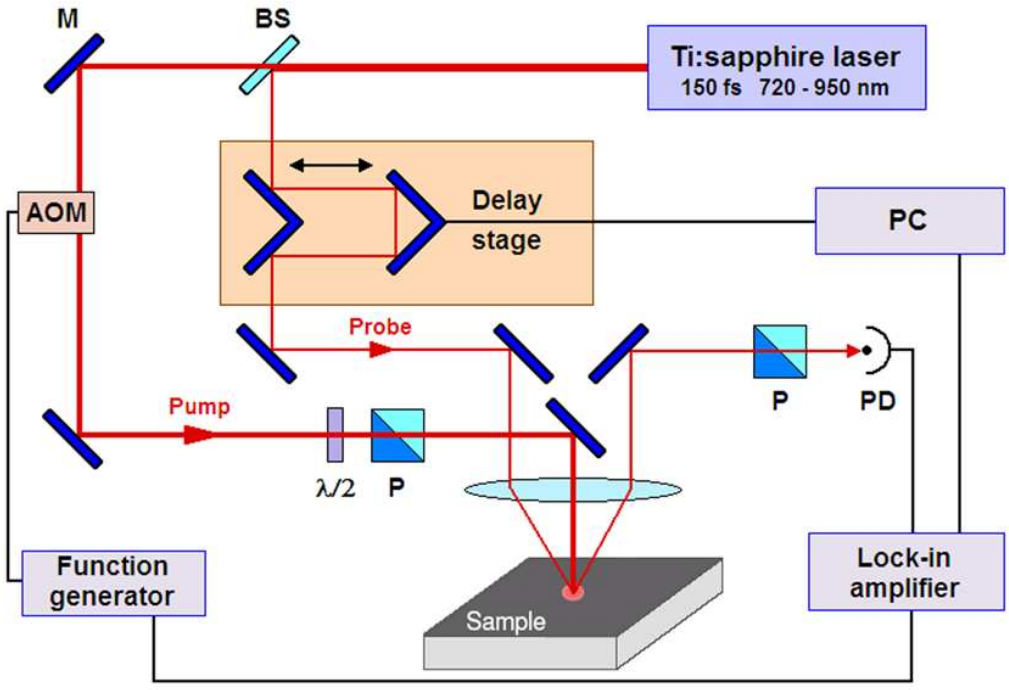

Figure 2.8: Schematic of pump-probe setup in reflection mode (AOM - acousto-optic modulator, BS - beam splitter, M - mirror, P - polarizer, $\lambda/2$ - half-wave plate, PD - photo detector).

consequently leads to the ability of detecting significantly smaller signals that would otherwise be undetectable. Signals on the order of $\sim 10^{-5}$ can be detected, which is right at the order of the usual photo-induced optical property change. In case the pump and probe beams have the same wavelength as in this particular setup, the beams can interfere during their overlap on the sample introducing additional signal to the real response. This effect is known as the coherence artifact. To eliminate this effect, the pump and probe beams need to be cross-polarized, which is achieved by rotating the pump beam polarization by 90° using a half-wave plate ($\lambda/2$).

A close-in view of the sample surface is obtained by a CCD camera connected to

a monitor, which allows proper alignment of the pump and probe beam. These are both focused by a lens onto the surface of the sample to a spot size of $\sim$100μm; their overlap is critical for maximizing the optical signal. The time-resolving capability of the pump-probe spectroscopy comes from the delay stage in the probe arm of the setup, since the time delay between the pump and probe pulse can be varied by moving the stage. So by changing the path length of the probe arm, the time of arrival of the probe pulse at the sample surface changes with respect to the pump-pulse arrival. The maximum time span of the measurement is determined by the traveling length of the stage; in our setup, the time span is $\sim$1 ns.

The probe pulse contains the information about the change in optical reflectivity after its reflection from the sample surface. However, there is also a lot of scattered light from the pump pulse that contributes to the noise. To minimize this noise, a polarizer oriented orthogonally to the pump polarization is used in front of the photo-detector (PD). The output signal from the photo-detector is usually pre-amplified and filtered before it goes to the lock-in amplifier. A computer reads the data from the lock-in amplifier and stores them into data files; it also controls the delay stage and relates its position with the measured signal. All the instruments are interconnected using a GPIB interface and controlled using a program written in LabView.

The many accessible parameters of the pump-probe system can be adjusted to suit the nature of the material to be studied. For example, if the sample is transparent at a particular wavelength being used, it is possible to do the measurement in transmission mode just by moving one mirror, polarizer and photo-detector. Another quick adjustment is doubling the frequency of the pump or probe beam, which re-

quires two lenses and a nonlinear optical crystal. In recent years, probing at different wavelengths has become a much desired feature of pump-probe systems. It is achievable by generating a white light continuum from the probe beam using, for example, a photonic crystal fiber. The relevant wavelength is then obtained using a narrow bandpass color filter; alternatively, the entire spectrum on each shot can be acquired by a CCD-array spectrometer.

CHAPTER III

INFRARED LASER ANNEALING OF METAL/DIELECTRIC COMPOSITES

Experimental results from our pulsed infrared laser annealing of metal/dielectric composites are reported in this chapter. Fast nucleation and growth of Au nanoparticles in both SiO_2 and Al_2O_3 matrices are observed. An opposite effect, nanoparticle dissolution, of this rapid thermal annealing process is observed in Ag-implanted SiO_2.

3.1 Au in SiO_2 matrix

The Vanderbilt Mark-III free electron laser[67] (FEL) was used to anneal the samples at different fluences. The energy per pulse used for the annealing was in the range from 5 to 9 mJ, which corresponds to fluence range of 2.5 to 4.5 J/cm^2. The Au implanted layer was well within the $1/e$ absorption length for SiO_2 ($\sim$ 3.4 μm) at 8 μm wavelength. All optical absorption spectra were measured with a Cary 5000 UV-Vis-NIR dual-beam spectrophotometer in the 200-800 nm wavelength range with an analyzing beam of 5 and 1 mm in diameter for silica and alumina samples, respectively. The silica samples were also characterized using 1.8 MeV He^+ Rutherford backscattering spectrometry. The backscattering collection angle was 175° and the collected charge was 3 μC. The energy resolution was 22 keV and the beam current was kept under 10 nA. All the RBS data were normalized to channel 200 in order to compensate for variations in surface charging effects from sample to sample. Scanning transmission electron microscopy (STEM) was performed at the Oak Ridge National

Laboratory using 300 kV (VG Microscopes) HB603U scanning transmission electron microscope equipped with aberration corrector (Nion Co.). Mie theory was used to fit the optical spectra and the particle size data thus obtained were compared to the STEM data where available.

3.1.1 Effects of IR laser annealing

Figure 3.1 [22] shows the optical absorption spectra of the Au implanted samples after the laser annealing at different pulse energies. With increasing fluence, the intensity of the surface plasmon resonance (SPR) peak at 520 nm increases. This increase is similar to that observed in thermal annealing experiments [68] attributed to the increase in the mean particle diameter. Optical image of the samples is shown in Fig. 3.2. It allows one to relate the changes in optical spectra to changes in color.

Since there are clear indications that, in the case of furnace thermal annealing, the atmosphere strongly affects the clustering of gold atoms in silica [68], an experiment was performed to compare the laser annealing effects in air and in vacuum. The silica sample used for this experiment was sequentially implanted with Au^+ ions at doses of 7.10^{16}, 3.10^{16} and 2.10^{16} ions/cm^2. The implantation energies were 2.75, 1.6 and 1.05 MeV respectively and the substrate was kept at room temperature during implantation. The energy per macropulse used for this annealing was 8 mJ which is equivalent to a fluence of $\sim$4 J/cm^2. The results, shown in Figure 3.3, imply that the atmosphere has very little or no effect on the infrared laser annealing process. The small differences between the in air and in vacuum FEL annealed spectra are more likely caused by the pulse-energy fluctuations. The area annealing usually takes at

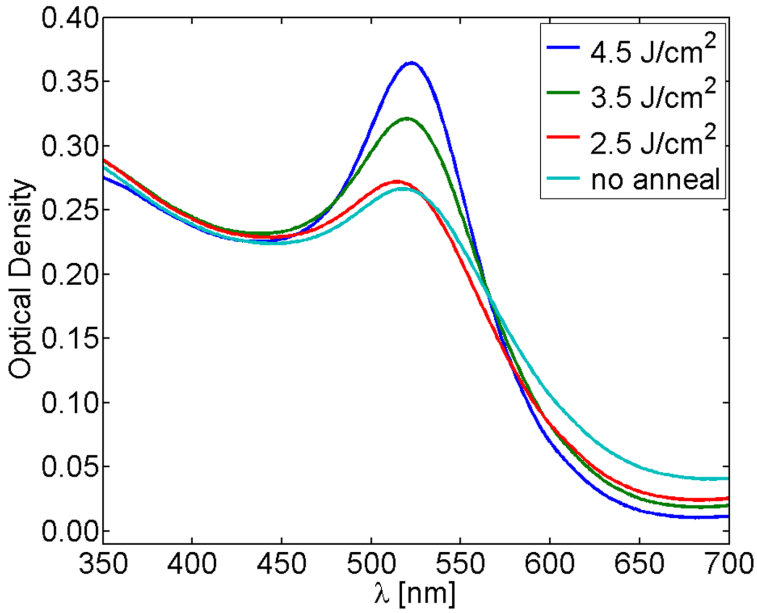

Figure 3.1: Optical absorption spectra of Au implanted samples laser annealed at different fluences.

least two minutes and the FEL pulse energy is known to fluctuate quite a lot at longer wavelengths. Actually, no difference was expected in air *vs* vacuum annealing because

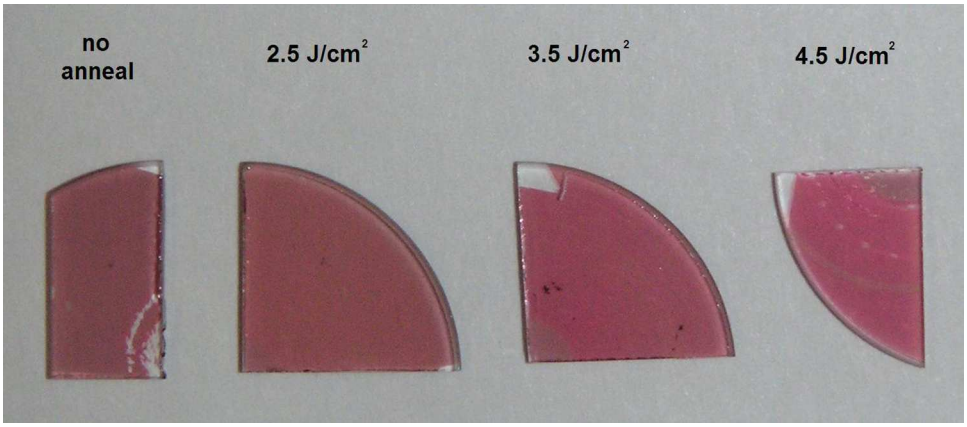

Figure 3.2: Optical image of Au implanted samples laser annealed at different fluences.

the pulsed laser annealing is a very fast process (4 μs per macropulse), so there is insufficient time for the atoms or molecules present in the atmosphere to diffuse into the matrix and influence the processes that are taking place there.

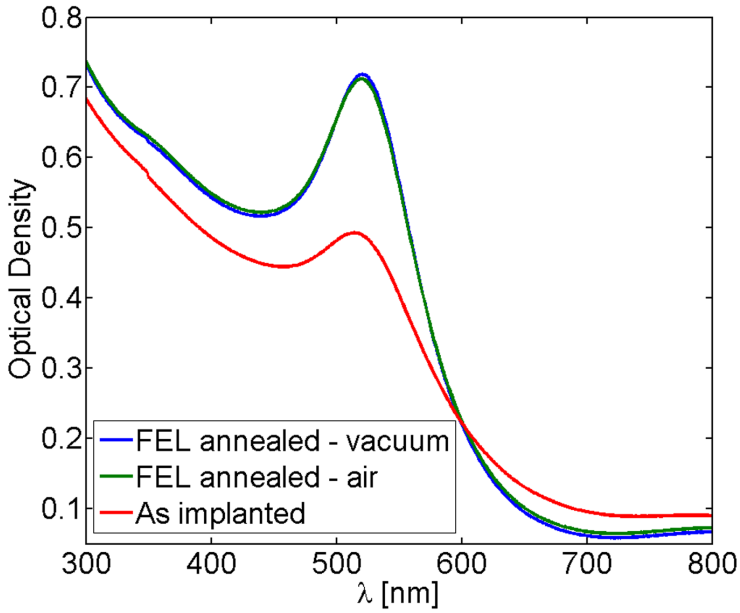

Figure 3.3: Optical absorption spectra of as-implanted and laser-annealed samples in air and vacuum.

The laser wavelength used in this experiment was 8 μm, well within the mid-infrared absorption region of fused silica which starts at a wavelength around 6 μm and peaks at 9.6 μm. The coupling is thermal, since the energy of 8 μm wavelength photons is close to the excitation energy of the Si-O bond vibrational mode. Moreover, the macropulse duration is comparable to the thermal diffusion time ($\sim$14μs) [19] for fused silica, so that the condition for thermal confinement of the laser en-

ergy is approximately satisfied. From the energy of the pulse and the basic thermal parameters of silica matrix, it is possible to make a simple estimate of the surface temperature during the laser annealing. For the maximum pulse energy (9mJ) used, the estimated temperature (∼2250K) is higher then the softening point of the fused silica (1958K) and is significantly higher then the temperatures used in furnace annealing [68]. The simple estimate agrees well with a 3D finite element model that was built and calculated in COMSOL, which predicts that the laser beam center area reaches temperatures above 2500 K. Figure 3.4 shows the surface temperature of the modeled 3D block (400x400x40 μm) at the end of FEL macropulse (t = 4 μs), which is when the temperature is highest. The heat transfer partial differential equations are at the core of the model and are solved in transient mode, so that the time evolution of temperature is obtained. The laser beam is modeled as a heating source within the modeled volume with a Gaussian shape, normal incidence and 300 μm diameter. It is assumed the absorption is not significantly affected by the presence of the metal-implanted layer right under the surface, so this layer is neglected overall in our model. The basic thermal properties of Corning 7940 fused silica used in the model are the thermal conductivity $k = 1.38$ W/cm K [19], the density $\rho = 2.2$ g/cm^3, the heat capacity $c = 0.74$ J/g K and the absorption coefficient $\alpha = 2.9\text{x}10^3$ cm^{-1} at the 8 μm wavelength[69].

The weakest point of this model is the assumption that the thermal properties do not change with rising temperature, especially because the absorption coefficient can change significantly with temperature. This assumption was necessary because the temperature dependence of the required variables is not readily available. If

the absorption coefficient is increasing with temperature, the maximum temperature reached would be even higher and the heating would be more confined near the surface area. On the other hand, if it is decreasing, the maximum temperature would be lower and the laser-affected area would be heated deeper and more evenly.

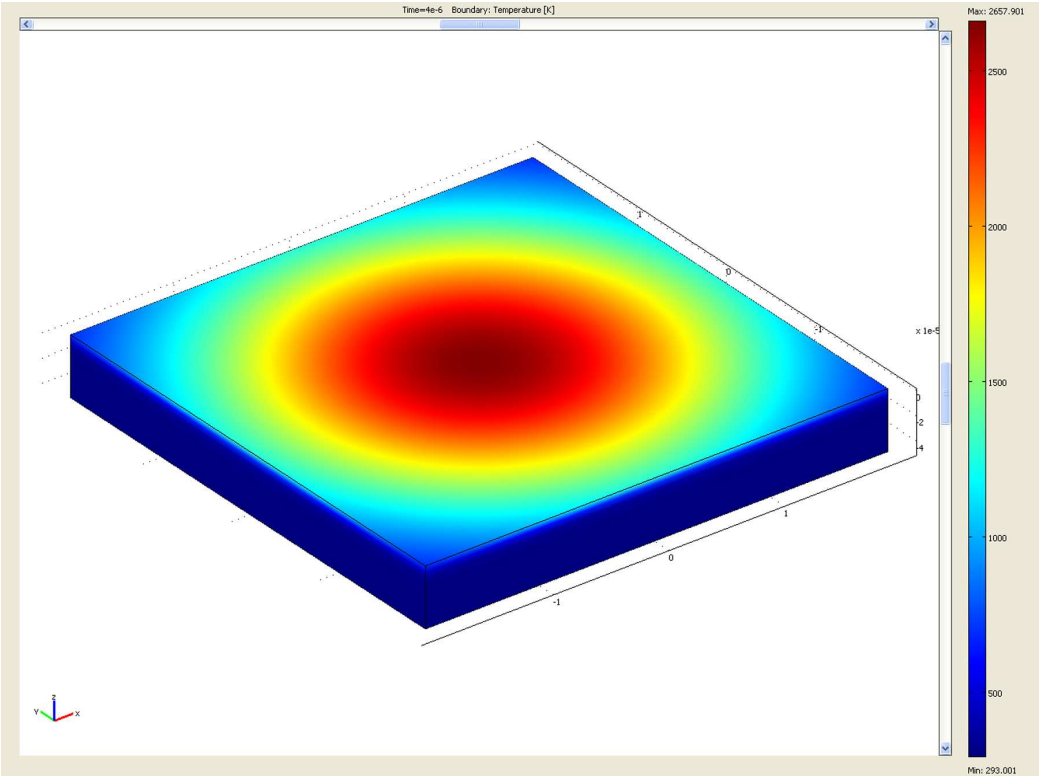

Figure 3.4: Surface temperature plot of the laser pulse hit block at the end of FEL macropulse (t = 4 μs). The maximum temperature reaches slightly above 2650 K.

In general, the high temperature is present only in the near-surface layer and is quenched rapidly due to thermal diffusion. For the temperature rise of ~2200K within the pulse duration of 4 μs, the heating rate is 5.5x10^8 K/s. Nanoparticle melting is expected, since the bulk gold (1340 K) melting temperature is lower then the esti-

mated temperature rise in the silica surface layer and the melting temperature of the nanoparticles is even lower than the bulk melting temperature due to thermodynamic size effects [70]. The temperature at which the Au particles and possibly also silica matrix melt, together with fast heating and cooling rates, allows rapid diffusion of Au atoms implanted in the near surface layer. Even though such conditions last for only very short time after the laser pulse, the time is evidently sufficient to cause significant growth of the Au nanoparticles, similar to the growth that occurs during furnace annealing in air[68].

RBS was used to study the effects of infrared laser annealing on the depth distribution of implanted Au ions. Figure 3.5 shows that laser treatment has no effects on the depth profile or amount of Au inside the matrix which is in an agreement with the fact that Au diffusivity in SiO_2 is low [71]. Using a simple backscattering analysis [72], the projected range was calculated for the as-implanted sample to be 260 nm and for the 4.5 J/cm^2 annealed one to be 252 nm. These results agree well with the value of 267 nm calculated by SRIM, noting that the calculation did not include surface sputtering.

Figure 3.6 shows the cross section STEM images and their processed counterparts of the as-implanted sample Fig.3.6(a) and the infrared pulsed laser annealed (fluency = 4.5 J/cm^2) sample Fig.3.6(b). The Au nanoparticles are easily identified as the darker spots on these bright field STEM images. In order to extract the nanoparticle size distributions, the images have to be processed. Since the actual thickness of the cross section sample is not known, it is possible to obtain only relative distributions. The image processing is done in MATLAB and it involves filtering and choosing the

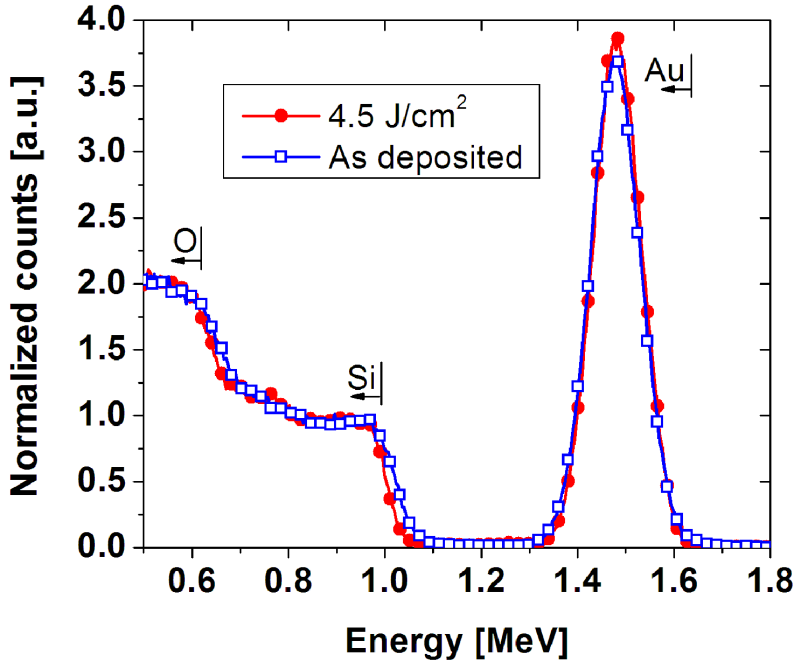

Figure 3.5: RBS measurements of Au implanted samples laser annealed at different fluences.

suitable grey-scale threshold that is used in conversion to black and white mode. The threshold is determined visually so that the white areas correlate with the particle sizes of the original images (Fig. 3.6). There are many overlapping particles in the images, which in reality might not be anywhere close to each other, so they are manually separated and adjusted for apparent size. The processed images are then analyzed and the number of pixels in each particle is recorded. The scale of the image is used to obtain the real size of one pixel, which is used to determine the nanoparticle sizes. The acquired data are statistically analyzed and the resultant nanoparticle size distributions for the two examined samples are shown in Fig. 3.7. The average cluster size changes from $\langle D \rangle = 2.4 \pm 1.2$ nm for the as-implanted sample (Fig. 3.7(a)) to

$\langle D \rangle$ = 6.5±2.5 nm for the laser annealed one (Fig. 3.7(b)). Another thing to notice is that the cluster density was reduced significantly ($\sim$ 5 times) by the annealing process. This suggests that the smaller size particles are dissolved into the matrix and then contribute to the growth of the larger clusters. A similar effect was observed in thermal annealing experiments performed in air atmosphere[73]. Interestingly, the width of the size distribution, stated as a fraction of the average diameter, actually narrows in the FEL-annealed sample, in contrast to what one usually observes during conventional thermal annealing.

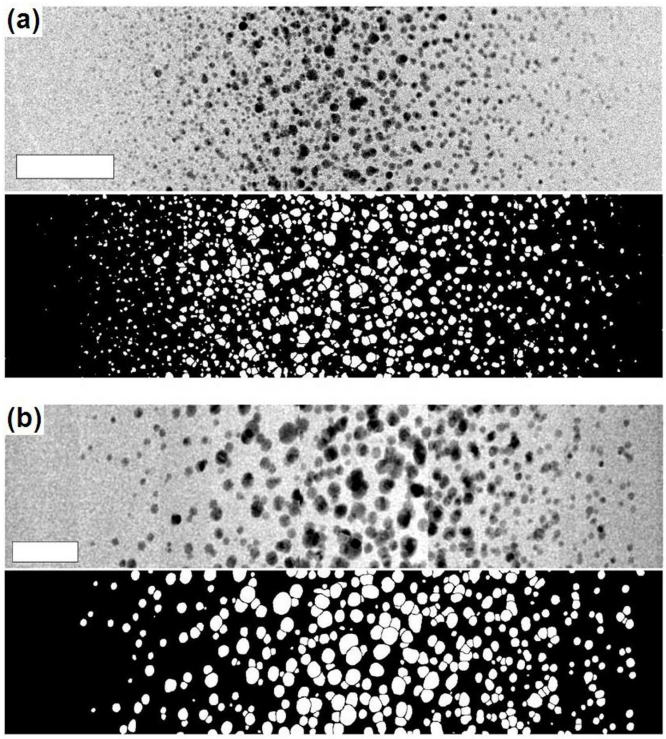

Figure 3.6: Cross-sectional bright-field STEM images (scale bar = 50 nm) of (a) the as-implanted sample and (b) the FEL annealed sample (fluency = 4.5 J/cm^2). The black and white images are the processed counterparts of the STEM images used to extract the nanoparticle size distributions.

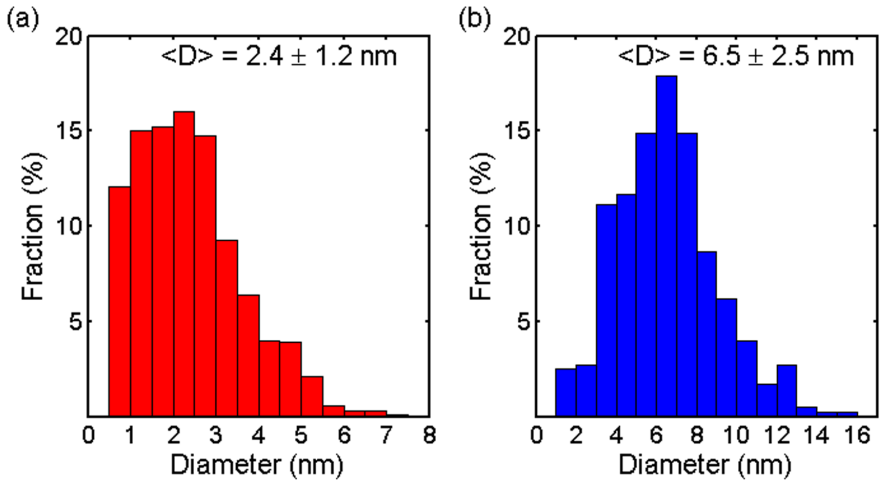

Figure 3.7: The cluster size distributions of (a) the as-implanted sample and (b) the FEL annealed sample (fluency = 4.5 J/cm^2) extracted from STEM images.

A nonlinear fit to the optical spectra was employed to extract the average diameter for comparison with the STEM analysis, using the procedure of Miotello[68]. The definition of the optical density

$$OD(\omega) = A \int_0^\infty dR f(R) \sigma(R, \omega) \tag{3.1}$$

was used as the fitting function, where the constant A is proportional to particle concentration and the thickness of the implanted layer. The extinction cross-section $\sigma(R, \omega)$ was calculated using the Mie theory with a finite-size correction to the Au bulk dielectric function [3]. $f(R)$ was assumed to be a log-normal distribution function. Fig. 3.8 shows the optical spectra of the two STEM analyzed samples along with the corresponding nonlinear fits[74]. The average cluster diameter extracted from the

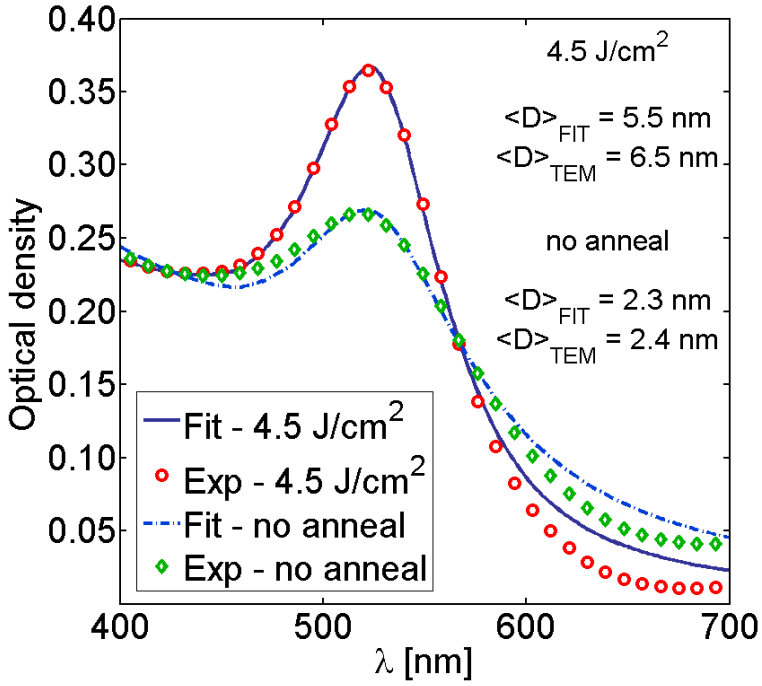

Figure 3.8: Optical absorption spectra of as-implanted and 4.5 J/cm^2 pulsed laser annealed sample. The dot-dashed and full lines represent the respective nonlinear fits. The average cluster diameter obtained from the fit is compared to the STEM extracted average diameter.

fitting process is $\langle D \rangle = 2.3$ nm for the as-implanted sample and $\langle D \rangle = 5.5$ nm for the laser annealed sample. These values correlate well with the STEM data. The slight discrepancy between the experimental and fitted average cluster diameters for the laser annealed sample could be caused by the fact that the size distribution (Fig. 3.7(b)) does not have exactly a log-normal shape. However, when we fit the optical spectra using a normal distribution, the extracted average cluster diameter $\langle D \rangle = 5.6$ nm is essentially the same as for the log-normal distribution fit. Another possible cause of the discrepancy is the interaction among nanoparticles, which have to be considered when the proximity of neighboring particles alters their local dielectric

environment. This particle-particle interaction is not included in Mie theory, so it is missing in our fitting procedure as well.

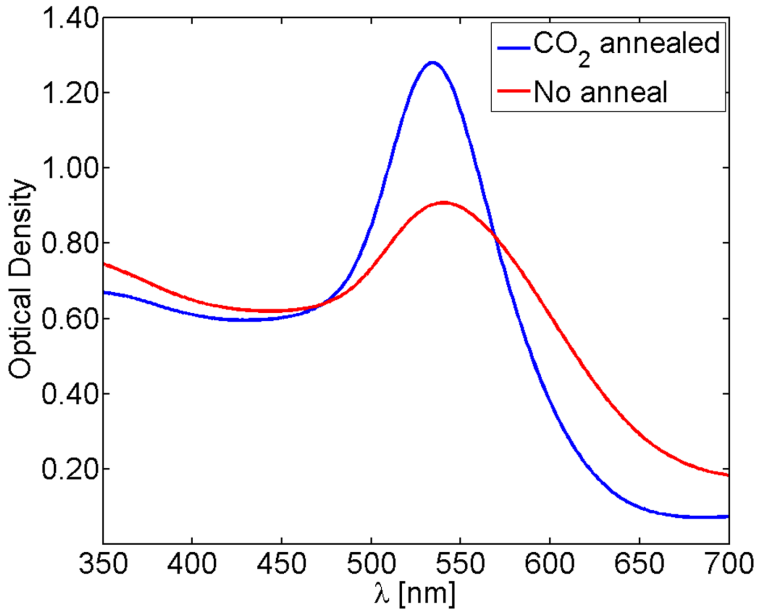

Figure 3.9: Optical absorption spectra of Au implanted sample annealed with CO_2 laser.

A few experiments were performed, in which the FEL was replaced by a small CO_2 laser operating in continuous wave (CW) mode. The sample used in these experiments was SiO_2 substrate implanted with $1.5x10^{17}$ Au ions at 1.1 MeV energy. The sample was kept at room temperature during implantation. The output power of the CO_2 laser was set to 4.5 W and the beam was focused using ZnSe lens down to a $\sim$50 μm spot. The sample was attached to our 3D moving stage setup and scanned in front of the laser beam. The CO_2 laser operates at 10.6 μm wavelength, where SiO_2 still has

strong absorption; annealing occurs at the laser beam spot where the sample surface is strongly heated. This hot spot is moved across the surface at a rate required for composite modification. The increase in intensity of the SPR peak is observed in Fig. 3.9 as the effect of the CO_2 laser annealing. The same effect was observed during the FEL laser annealing. This shows that CO_2 laser can also successfully modify Au/SiO_2 composite and suggests it could possibly substitute for the FEL laser. This is favorable for applications, because CO_2 lasers are already the most widely used lasers in industry.

3.2 Ag in SiO_2 matrix

The Ag implanted samples were FEL laser annealed the same way as the Au implanted samples. Optical spectroscopy and RBS analysis were performed. The analysis parameters are the same as for Au implanted samples and are described in detail in previous section.

3.2.1 Effects of IR laser annealing

The optical absorption spectra of the Ag implanted samples (Fig. 3.10) are significantly different from those of Au implanted samples (Fig. 3.1). The as-implanted sample has a strong SPR peak at 415 nm and a small shoulder at 530 nm. Increasing the laser annealing energy causes the shoulder peak to disappear completely and to shift the main SPR peak by $\sim$ 10 nm to lower wavelength. However, when the laser energy per macropulse is increased to 10 mJ (equivalent to fluence $\sim$5 J/cm^2), all spectral features are lost, together with the typical yellowish color (Fig. 3.11, bottom

right piece). This is attributed to reaching the ablation threshold for silica, which is around 5 J/cm^2, in our experimental setup.

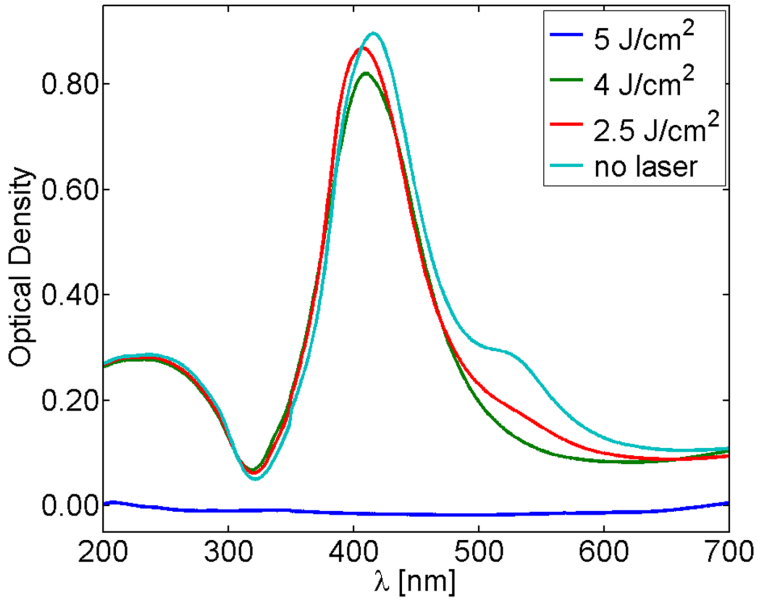

Figure 3.10: Optical absorption spectra of Ag implanted samples laser annealed at different fluences.

Figure 3.12 shows the RBS data for Ag implanted samples. The projected range for the as-implanted sample is only 27 nm, which is much lower then the SRIM calculated projected range 132 nm. The discrepancy is possibly caused by not including surface sputtering in the SRIM calculation; also the fact that the substrate was kept at 400 °C during implantation might allow Ag atoms diffuse closer to the surface. From the data for samples laser-annealed at laser fluences of 2.5 and 4 J/cm^2, it is clear that the laser treatment is causing Ag diffusion into the substrate, shifting the

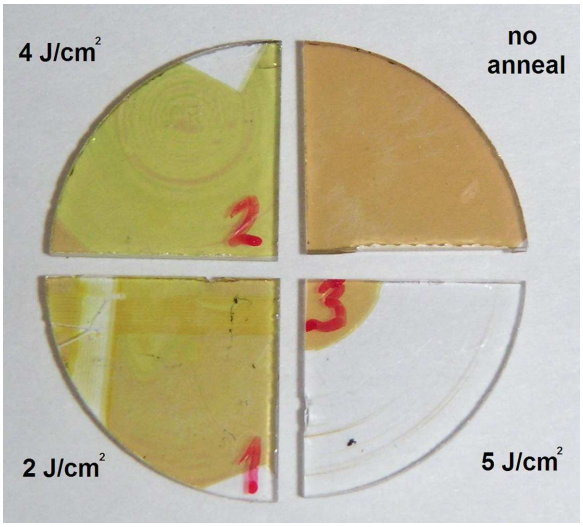

Figure 3.11: Optical image of Ag implanted samples laser annealed at different fluences.

RBS calculated projected ranges to 88 and 145 nm respectively. The amount of Ag present in the substrate does not seem to change significantly for the laser fluence below 5 J/cm^2. However, for fluences of 5 J/cm^2 and above, no Ag atoms were detected by RBS indicating that they were completely removed by the laser treatment. This finding correlates well with the optical measurements, where it was suggested that ablation takes place above that energy.

It has been shown in several studies that excimer-laser annealing causes a reduction of the size of the implanted silver nanoparticles in glass together with some dissolution of silver into the glass matrix [26, 29, 32]. The effects of infrared laser annealing are similar for Ag nanoparticles embedded in silica. The optical absorption data of the Ag implanted samples before and after infrared laser annealing suggest that the particles are getting smaller because the SPR peak is shifting to lower wave-

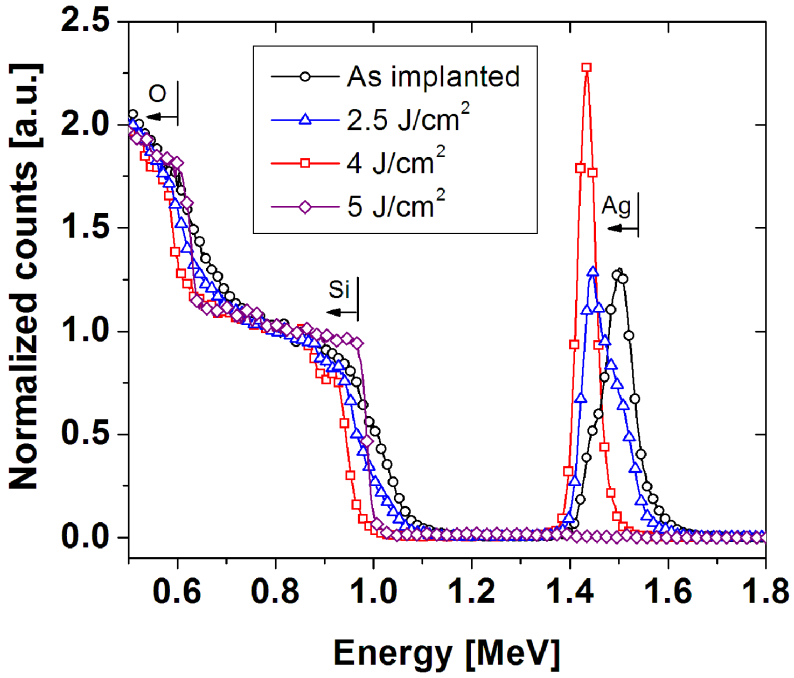

Figure 3.12: RBS measurements of Ag implanted samples laser annealed at different fluences.

lengths. There is also a visible drop in the SPR peak intensity, which is explained by the fact that some of the particles are dissolving into the matrix. This interpretation is supported by the RBS data, which show that the silver is diffusing deeper into the silica substrate upon laser treatment. The laser-assisted diffusion mechanism underlies the complete dissolution of the nanoparticles during the laser pulse and their re-growth in the cooling phase after the pulse. However, once the energy per pulse reaches the ablation threshold of the silica matrix, the silver-implanted layer is ablated.

3.3 Al_2O_3 matrix

The FEL wavelength of 9 μm was used for annealing of Au implanted sapphire sample. Optical spectroscopy and SEM were used to analyze the effects of FEL annealing.

Figure 3.13 shows the optical absorption spectra of the Au implanted sapphire sample. The optical spectra of the as-implanted sample do not show any SPR peak. The reason is that the sapphire substrate was kept at liquid nitrogen temperature during the implantation process, so the Au nanoparticles could not form. The spectra of the annealed samples clearly indicate that the effect of FEL laser annealing is similar to the effect of furnace annealing which was done in oxygen atmosphere for 2 hours at 1100°C. The presence of the SPR peak indicates that the infrared pulsed laser annealing is able to initiate the formation of Au nanoparticles in the Al_2O_3 matrix within the short time of the macropulse.

The drawback of rapid, high-temperature laser processing is that it causes surface cracking of the sapphire substrate (Fig.3.14). The thermal considerations in this case are very similar to the case of fused silica. However, the most significant difference is that sapphire is a crystal and its thermal expansion coefficient is 10 times larger than the one of silica (Table I.1). This means the localized heating caused by absorption of the laser pulse in the near surface layer generates a lot of thermal stress that is relieved by cracking, which is clearly visible in Fig. 3.14. Of course, such cracking is not a desirable effect and the future plan is to study the effect of infrared laser annealing on amorphous alumina samples, where the cracking is not expected to be

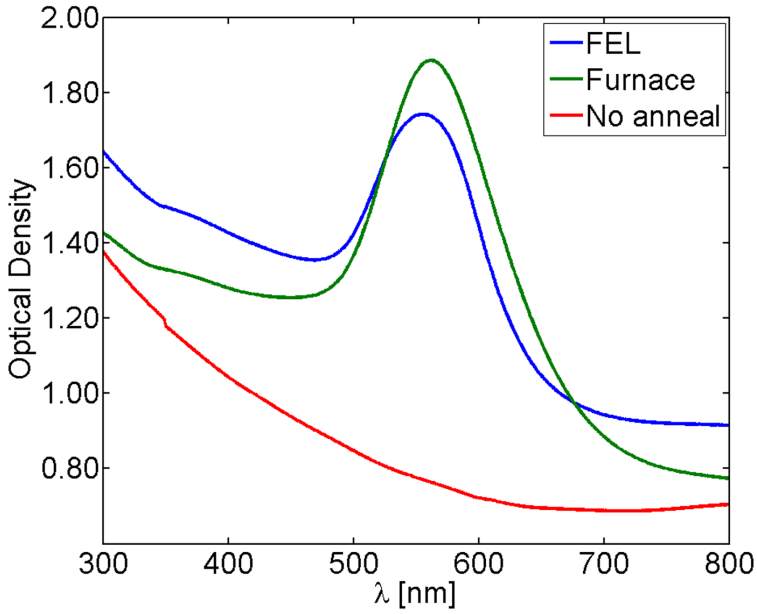

Figure 3.13: Optical absorption spectra of Au implanted Al_2O_3 sample, for FEL and furnace annealed cases.

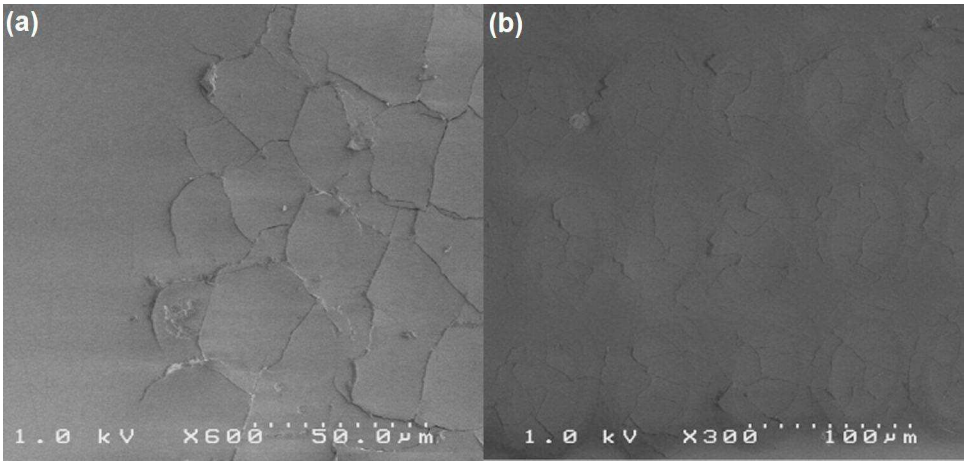

Figure 3.14: SEM images of FEL annealed Au/Al2O3 sample. Edge region of the laser annealed area (a) and a region where the laser pulses do not overlap (b).

so severe or possibly could be avoided completely.

3.4 Conclusions

Composite optical materials in general are interesting and promising materials for applications. They can be produced by several methods, but it would be useful if their optical properties could be adjusted or modified. The study of the effects of the infrared pulsed laser radiation, as a tool for such modification, is presented here. The optical absorption spectra of the metal implanted samples clearly indicate that the metal nanoparticles were successfully modified and formed using the infrared pulsed laser irradiation. The observed changes, which occur within the time duration of a laser pulse, are in case of Au implanted samples comparable to the effects of an hour-long furnace annealing at high temperatures. The speed of the infrared laser annealing and also the fact that its effects are not influenced by the surrounding atmosphere are advantageous properties. Further, the ability to localize the annealing effect and the existence of the broad infrared absorption wavelength region for most of the dielectric matrices are additional advantages that can make the infrared pulsed laser annealing a serviceable tool for the processing of nanocomposite optical materials.

CHAPTER IV

COHERENT ACOUSTIC PHONONS IN METAL/DIELECTRIC SUPERLATTICES

A time-resolved pump-probe technique was used to measure the photoinduced reflectivity change in superlattices. Optical absorption of the ultrashort pump pulse sets up a thermal stress that impulsively excites strain waves in the multilayer structure. These waves (coherent acoustic phonons) generate a change in reflectivity via the photoelastic effect, which is observed with a time-delayed probe pulse. Optical pulses of a mode-locked Ti:sapphire laser (Mira 900) at several wavelengths were used in our experiments. The full width at half maximum pulse duration is $\sim$120 fs and the repetition rate is 76 MHz. The pump beam is modulated by an acousto-optic (AO) modulator at a frequency of 53 kHz for lock-in detection. Pump and probe beams are both focused using the same lens onto a spot having a diameter of roughly 100 μm. The pump beam is at normal incidence to the sample surface, while the angle of incidence of the probe beam is less then 10°.

All samples in this work were prepared at the University of Alberta. The multilayer films were deposited on fused silica substrates kept at room temperature. The Al_2O_3 layers were deposited using electron beam evaporation and the Au layers using thermal evaporation from a tungsten boat. Since both of these evaporation techniques were available in our deposition system, the samples were inside the vacuum chamber during the entire deposition process. The vacuum prior to deposition was

10^{-7} Torr. The superlattices all start and also terminate with an Al_2O_3 layer. Both, the thickness of Al_2O_3 layers and the thickness of Au layers was varied. The number of periods in most of our samples is 10. Several samples with Ag metal films were also prepared. In order to determine the elastic properties of the amorphous Al_2O_3 layers, two samples of a single Al_2O_3 layer with thicknesses of 1640 and 2300 nm were prepared at first on SiO_2 substrate and capped with 15 nm of Au acting as a transducer. However, we were unsuccessful in obtaining usefull data from these samples, so another set of films with 260 and 410 nm thickness was deposited onto a Si $< 100 >$ substrate at room temperature and a thin 15 nm layer of Al was used as a transducer.

4.1 Dielectric characterization

Many different deposition techniques are used in preparation of multilayer structures. However, even when depositing the same material, the various deposition techniques cause the elastic properties of the films to differ. In order to build a realistic model of the superlattice, it is important to know the elastic properties of the Al_2O_3 films deposited using electron beam evaporation. Pump-probe measurement is very suitable method for determination of the sound velocity.

A basic schematic of such measurement is shown in Fig. 4.1. The sample consists of a layer of the material to be studied deposited on a substrate, plus a thin cap layer (< 20 nm) which acts as a transducer and is usually metal. The pump pulse heats up the cap layer and the thermal stress launches a strain pulse into the studied layer. Upon reaching the film/substrate interface, part of the strain pulse is transmitted into

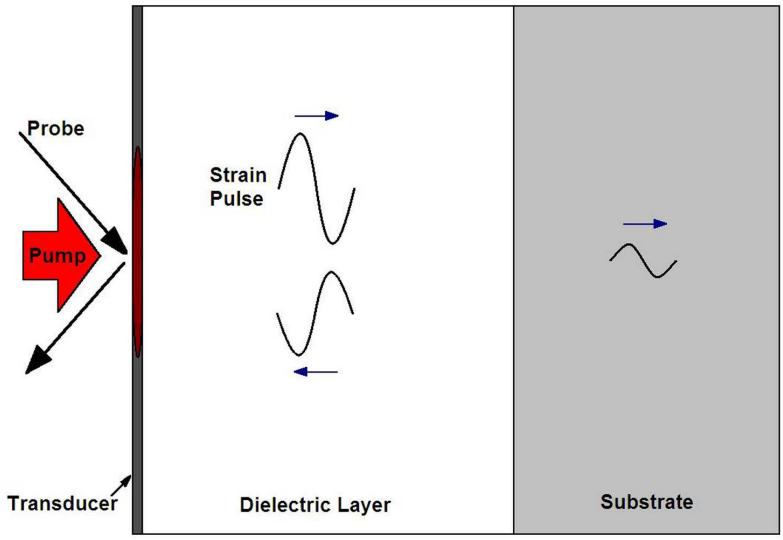

Figure 4.1: Schematic of the sound velocity measurement using pump-probe technique.

the substrate and the other part is reflected. It is important to maximize reflection at this interface, since the wanted signal is generated by the reflected part of the strain pulse upon arriving at the cap layer. The acoustic reflection coefficient r is defined by[75]

$$r = \frac{Z_2 - Z_1}{Z_2 + Z_1}, \tag{4.1}$$

where $Z_{1,2}$ are the acoustic impedances of the substrate and the film, respectively. A larger mismatch between the acoustic impedances results in larger reflection coefficient. The probe pulse detects the returning strain pulse as an echo through the photoelastic effect or through just the moving surface; the allusion to the echo is relevant since the strain pulse is sound in the solid material. The pulse can be further reflected at the surface and repeat its journey through the film. Thus under optimal

conditions several echoes can be observed, which greatly increases the measurement accuracy. In addition to the reflection coefficient, the attenuation of the strain pulse in the studied film is also an important factor. The attenuation is mostly consequence of phonon scattering and if it is significant, it can make the observation of even the first echo difficult.

4.1.1 Longitudinal sound velocity of Al_2O_3

At first, two samples with 1640 nm and 2300 nm thick Al_2O_3 films were prepared on SiO_2 substrate. A 15 nm thick Au layer was used as a transducer. Several attempts were made to observe an echo in these samples, however they were unsuccessful. Figure 4.2 shows a typical pump-probe signal from 1640 nm sample measured at 780 nm wavelength. The fast transient and slowly decaying thermal background are visible. There is an oscillatory signal detectable after thermal background subtraction (see inset in Fig. 4.2). The period of the oscillation is $\tau = 42.9$ ps. From our experience, this is consistent with a coherent acoustic phonon pulse propagating in a fused silica substrate. The oscillation period value can be used to calculate the sound velocity of SiO_2 using this expression $v_s = \lambda/2n\tau$,[76] where λ is the probing wavelength and n is the index of refraction. After putting in these values ($\lambda = 780$ nm and $n = 1.46$), the sound velocity is 6.2 nm/ps, which is in agreement with previous studies[76, 77]. Determining the time at which the oscillation starts allows us to measure the sound velocity in Al_2O_3 film, since that is the time when the strain pulse arrives at the Al_2O_3/SiO_2 interface. However, as seen in the inset of Fig. 4.2, the oscillation onset time is not very clearly set, so only a rough estimate of the Al_2O_3

sound velocity is possible using these samples. Assuming the onset time to be 220 ps and taking account of the Al_2O_3 film thickness, the estimated sound velocity is 7.45 nm/ps. This is a reasonable estimate when compared to the value of 6.7 nm/ps obtained by Rossignol[46] *et al.*, also considering that their Al_2O_3 films were prepared by sputtering.

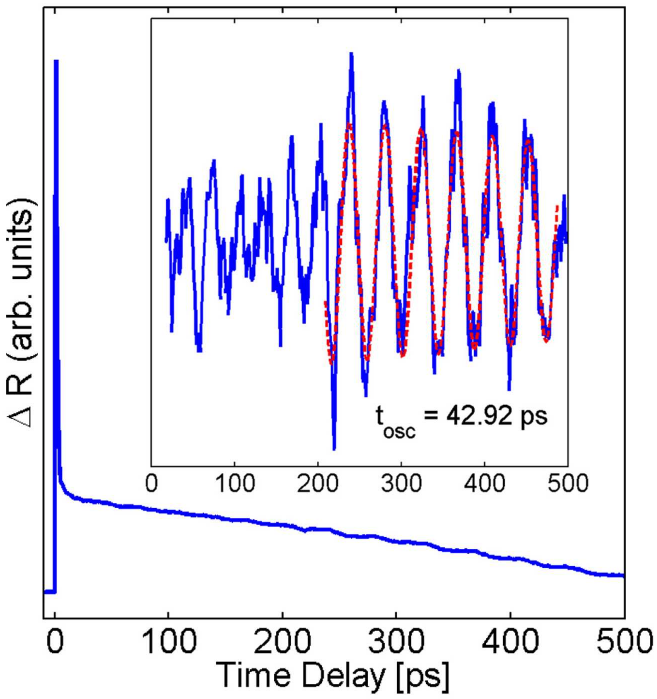

Figure 4.2: The measured $\Delta R(t)$ for 1640 nm Al_2O_3 film. Inset: The signal with thermal background subtracted. The oscillation appears once the strain pulse reaches SiO_2 substrate.

Several factors contributed to the fact that no echoes are observed in the first set of samples. First, the films are rather thick, and that combined with the attenuation

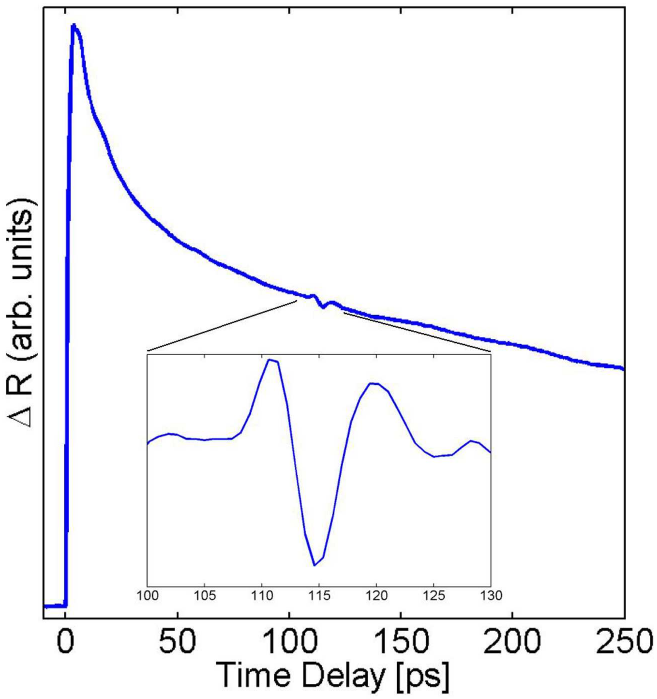

Figure 4.3: The measured $\Delta R(t)$ for 410nm Al_2O_3 film on Si substrate. Inset: Zoomed-in phonon echo signal.

can significantly weaken the strain pulse. Second, the reflection coefficient at the Al_2O_3/SiO_2 interface is not very high. Using these values for the density and velocity of sound for fused silica $\rho_{SiO_2} = 2.2$ g/cm^3 and $v_{SiO_2} = 5.97$ nm/ps[77], the calculated reflection coefficient is only -0.38. The minus sign means there is a π phase shift during the reflection. In order to improve the detectability of the acoustic echo, another set of samples was prepared, but with thinner Al_2O_3 films and on Si substrate. Also the metal used as a transducer was changed to Al due to its higher thermal expansion, which generates stronger strain pulses. The pump-probe signal for the 410 nm Al_2O_3 film sample is shown in Fig. 4.3. Only one acoustic echo is detected, but even that

allows more accurate sound velocity determination than the previous measurement of thick Al_2O_3 films. The strain pulse returns to the surface in a time of 112±3 ps, having traveled twice the thickness of the Al_2O_3 film, which was measured using a profilometer to be 410±20 nm. The calculated sound velocity is 7.3±0.4 nm/ps. This value is used in all theoretical calculations and modeling.

4.2 Au/Al_2O_3 superlattices

All multilayer samples were prepared at the University of Alberta. Initial films were deposited by graduate students from Prof. Meldrum's group. I prepared most of the samples analyzed in this work during my two week visit to Edmonton. Before performing the transient time-resolved spectroscopy, the samples were analyzed using profilometer, optical spectroscopy and few samples were also examined by TEM. The

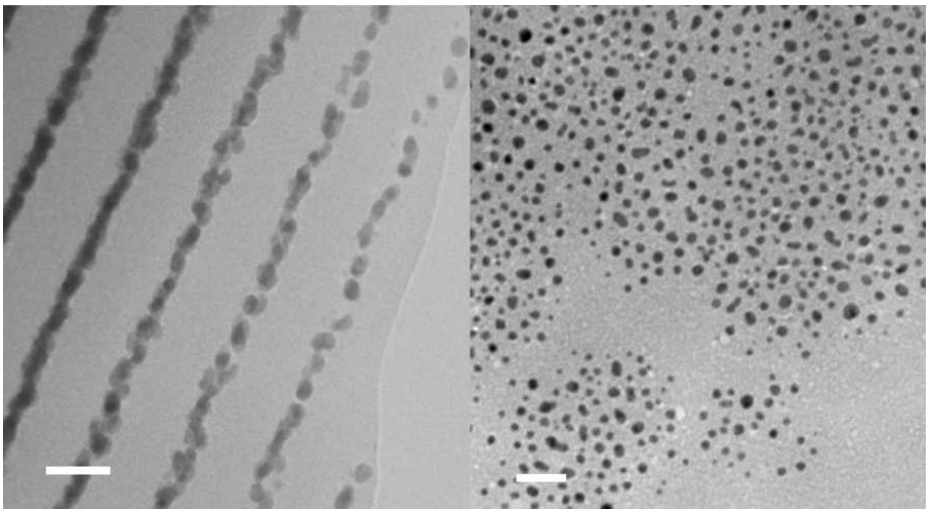

Figure 4.4: Cross-sectional (left) and planar (right) TEM images of Au(2 nm)/Al_2O_3(20 nm) multilayer (scale bars = 20 nm). The surface is parallel to the Au layers in the cross-sectional image (left).

main purpose of using TEM was to characterize the structure of the metal films in our multilayers. Figure 4.4 shows cross-sectional and planar TEM images of a Au(2 nm)/Al_2O_3(20 nm) superlattice (having 8 periods) that was prepared under same conditions as all our other films. The nanoparticle structure of the Au films is obvious. The size of the nanoparticles ranges up to 5 nm in diameter. It is well known and our own experience also shows that, under typical deposition conditions, gold does not form a continuous layer until its thickness is over 5 nm[78]. This leads to the conclusion that nearly all of our Au films have nanoparticle structure, in which the particles get closer together and slightly larger as the thickness of the film increases, gradually approaching a continuous layer. This assumption is supported by optical spectra shown in Fig. 4.5. The displayed data comes from a set of samples with constant Al_2O_3 film thickness of 45 nm and varying Au film thickness. The broad

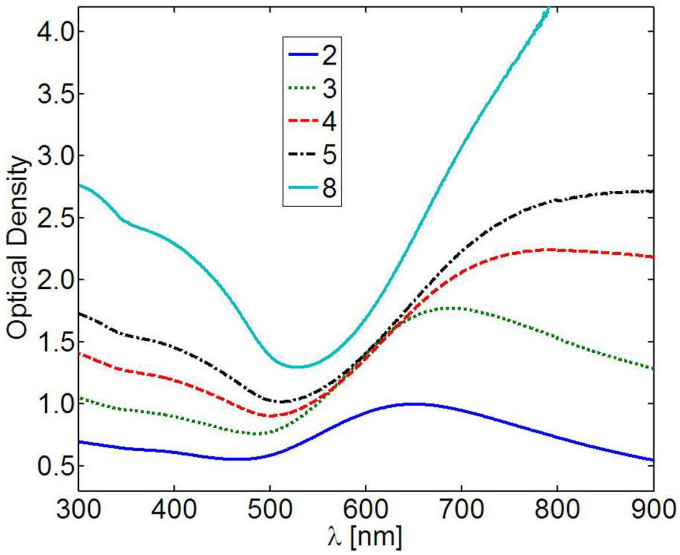

Figure 4.5: Optical spectra of the superlattices with various Au layer thicknesses. The legend represents the Au layer thickness in nm.

surface plasmon peak can be seen in the spectrum of the 2 nm Au layer superlattice at ∼650 nm. It is not only broad but also significantly red-shifted due to the interaction among the nanoparticles within each Au layer. The plasmon width and the red-shift increase together with increasing Au layer thickness.

The nanoparticle structure of the Au films is in sharp contrast with the theoretical model assumption of sharp smooth interfaces. However, our results, presented below, suggest that the nanoparticles do not significantly affect the overall elastic properties of the superlattices.

4.2.1 Au layer thickness effects

In this section, time-resolved optical spectroscopy data of a set of Au/Al_2O_3 superlattices with fixed thickness of all Al_2O_3 layers and varying Au layers thickness are presented and analyzed. The laser wavelength used in these measurements was 830 nm and the pump power was 40 mW unless stated otherwise. A typical fast transient signal within the first few picoseconds after the arrival of the pump pulse is observed in all samples. It is a consequence of the ultrafast excitation of electrons in Au layers and their thermalization through electron-electron interactions, which is then followed by electron-phonon interaction. This leads to heating of the gold layers and generation of thermal stress that initiates surface-mode vibrations.

Obtained transient signals $\Delta R(t)$ are shown in Fig. 4.6 and Fig. 4.7. Double exponential function described in more detail in Appendix A was used to fit the transient signals. Nonlinear least squares method was used and all fitting was done in MATLAB, utilizing mainly function *fit*. The left columns of the Figs. 4.6 and 4.7

display the first 40 ps of the transient signals for the superlattices with various Au layer thicknesses together with their fits and with the extracted rise and fall times. The rise and fall times vary only a little among different samples. It is because they are the characteristic of the metal layer material, gold in our case, and not its thickness. The rise time is related to the electron-electron (e-e) interaction, but is also strongly influenced by the convolution of pump and probe pulses. The fall time is determined mainly by the electron-phonon (e-p) interaction. Due to the nanoparticle structure of the Au layers and consequent high surface to volume ratio, the e-p interaction can be different then in bulk metal[79]. Reported e-p interaction time of Au is $\sim$1 ps[41]. This should be compared to the sum of the rise and fall time, rather then just the fall time, because the rise time is quite long and so the electrons are transferring their energy to phonons already during that time. The sum transient time is $\sim$1.3 ps, which correlates well with previous studies. It is also an onset time of thermal stress buildup.

The right columns of the Figs. 4.6 and 4.7 display the part of the transient signal starting at 5 (or more) ps. The slow photothermal response superimposed on the oscillatory signals was removed using smoothing. The oscillations, which are related to the surface modes, are clearly seen in all traces. Exponentially decaying cosine function, also described in Appendix A, was used to fit the data. The extracted period of the oscillations and the decay time τ are also shown. In general, the fitted curves overlap with the experimental data very well. Only in case of the 3 nm thick Au layer sample a slight discrepancy is observed. If the whole trace is fitted, then the fit curve gets out of phase after first few periods and does not fit well the rest

of the signal(see Fig. 4.6(b2) Fit 1). However, if the first few periods are omitted, the rest of the signal is fitted very well with a longer period. The possible origin of this faster oscillatory signal at the beginning is the propagating (bulk) modes as they move into the superlattice leaving the detection volume. Fast Fourier transform (FFT) was used in an attempt to distinguish the two frequency modes, however the data do not have many points so the resolution of FFT is not good enough. Overall, our data do not have very high density of points, because the measurements would otherwise be too long and could be affected by laser stability issues. Therefore, we decided to use oscillation fitting, rather then FFT, for determination of the surface mode frequencies for all samples.

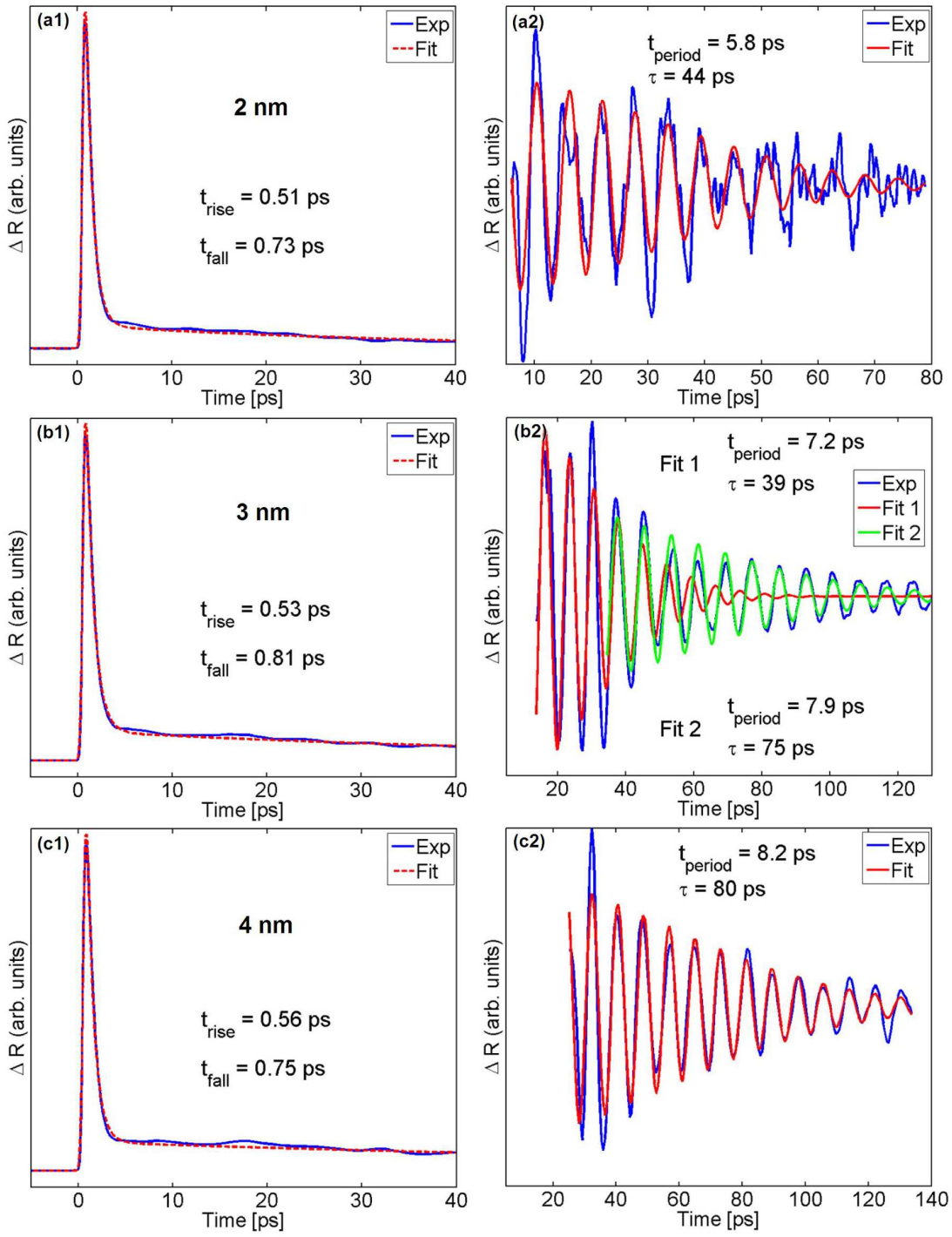

Figure 4.6: (a1),(b1) and (c1) show the measured $\Delta R(t)$ for Au(2, 3 and 4 nm)/Al_2O_3(45 nm) superlattices together with the fitted curves and the obtained rise and fall times. Thermal background subtracted oscillatory part of the signals fitted with exponentially decaying cosine function (a2, b2 and c2). Also shown is the period of the oscillation and the decay rate extracted from the fit.

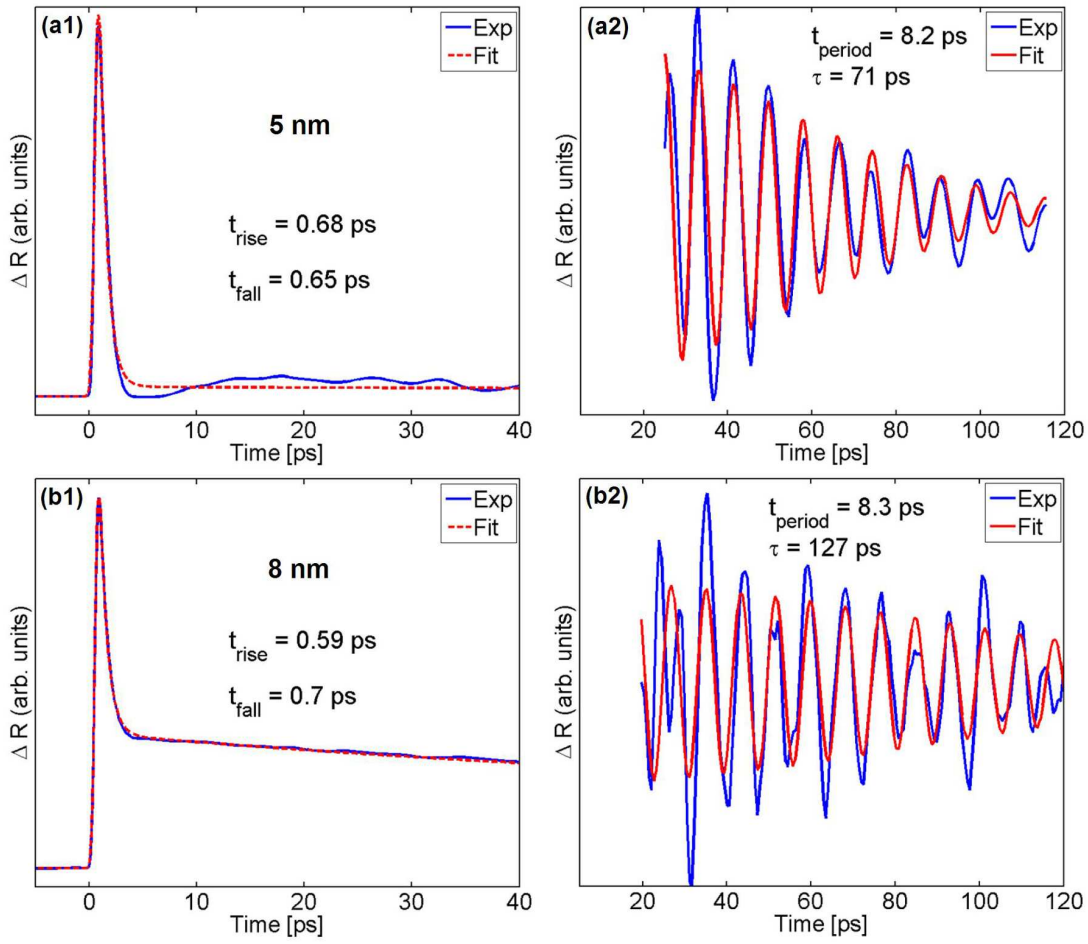

Figure 4.7: (a1) and (b1) show the measured $\Delta R(t)$ for Au(5 and 8 nm)/Al_2O_3(45 nm) superlattices together with the fitted curves and the obtained rise and fall times. Thermal background subtracted oscillatory part of the signals fitted with exponentially decaying cosine function (a2 and b2). Also shown is the period of the oscillation and the decay rate extracted from the fit.

Before proceeding to a comparison between theory and experiment, it is useful to look at all oscillatory signals together. The part of the transient signals starting at 10 ps is zoomed-in and shown in Fig. 4.8. All the signals are normalized to the peak value of the fast transient. The trace for the sample with 5 nm Au layers is offset slightly for clarity and the 8 nm trace was shifted down considerably. The amplitude of the oscillations increases with increasing Au layer thickness up to 5 nm. However, the amplitude is significantly smaller for the 8 nm sample. The thermal background is much different for this sample as well. This is probably caused by the fact that the 8 nm Au film is more like a continuous film rather then a film composed of separate nanoparticles.

The experimental results, after the conversion to frequencies, are compared to the theoretical calculations of equations (1.21) and (1.27). They are listed together in Table IV.1. The first surface mode, which exists in the first zone-boundary ($q = \pi/d$) band gap was detected only in samples with the Au layer thickness of 4 and 5 nm. However, the second surface mode, which is in the first zone-center ($q = 2\pi/d$) band gap, was observed for all Au layer thicknesses. The highest observed frequency was 172.4 GHz. Any higher frequency modes are not observed largely due to mode selection rule[80]. The rule is as follows: The stress pattern and the sensitivity function both have the periodicity of the superlattice. However, the waveforms ($\eta(z)$) of all zone-boundary surface modes (n = 1,3,5,...) invert from one period to the next (see Fig. 1.4(b)), so they couple poorly with the stress pattern and the sensitivity function. The same applies to the even zone-center modes (n = 4,8,12,...) because they are approximately antisymmetric within each sublayer. Therefore only the odd

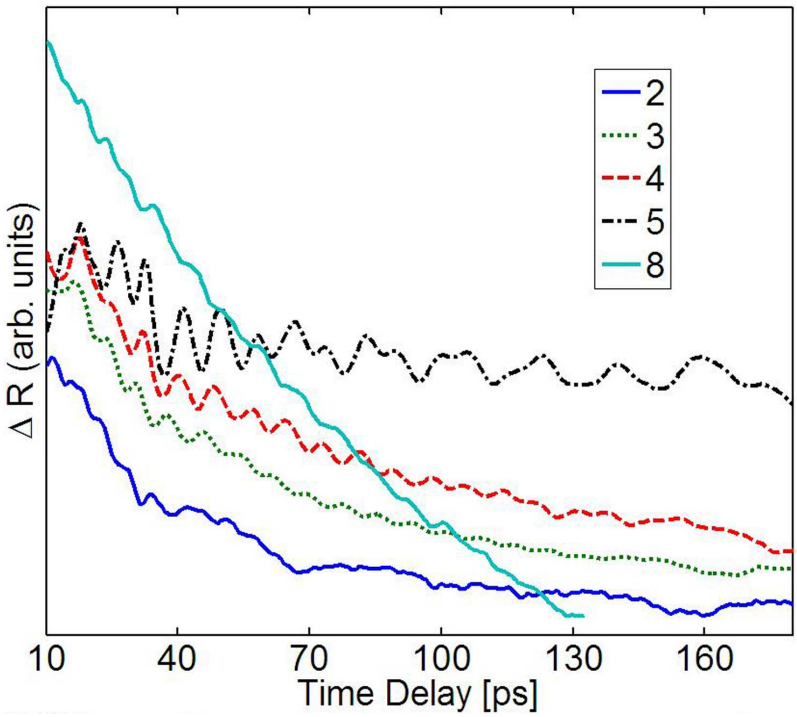

Figure 4.8: Zoomed-in oscillatory signal for all Au layer thicknesses. The 5 nm trace was slightly offset for clarity and the 8 nm trace was shifted downward.

zone-center surface modes (n = 2,6,10,...) are preferably excited and observed. In addition, the coupling coefficient is roughly proportional to $(1/n)$, so the higher modes are less likely to be detected[80]. Furthermore, the speed of the onset of the thermal stress (∼1.3 ps - 0.8 THz) puts a limit on the highest excited frequency. The selection rule is slightly relaxed for the first surface mode due to its short decay length. Also the damping rate of this mode is the lowest among all surface mode, which makes it easier to be detected.

In most cases, the experimental frequencies ν_{exp} agree to within a few percent with the theoretical ones ν_{th}. There is, however, a large discrepancy between theory

and experiment for the 2 nm Au layer thickness sample. One of the possible causes of this discrepancy is the nanoparticle structure of the gold layers (Fig. 4.4). However, it seems that even though all the Au films have likely nanoparticle structure, starting at 3 nm thickness, it does not significantly affect the overall elastic properties of the superlattice as a whole. Looking at Table IV.1, the theoretical frequencies for Au layers > 3 nm are slightly larger than the experimental ones. This was observed in several other studies[48, 46, 80], which explored the possible origin of the discrepancy in modified elastic properties of thin films, surface modifications of the constituent layers or the accuracy of the layer thicknesses. The nanoparticle structure of our Au films can affect all of these properties.

Table IV.1: Theoretical and experimental surface-mode frequencies of Au/Al_2O_3(45 nm) superlattices. d_{Au} is the gold layer thickness. ν_1 and ν_2 are the frequencies of the first and second surface mode, respectively. l_1 and l_2 are their decay lengths. d is the repeat distance. τ_1 and τ_2 are the decay times of the respective surface modes. [1]Pump at 800nm, probe at 400 nm.

	Theory				*Experiment*			
d_{Au} (nm)	ν_1 (GHz)	$\frac{l_1}{d}$	ν_2 (GHz)	$\frac{l_2}{d}$	ν_1 (GHz)	τ_1 (ps)	ν_2 (GHz)	τ_2 (ps)
2	67.6	9.2	138.7	3.0	-	-	172.4	44
3	63.2	5.2	133.0	2.0	-	-	126.6	75
4	59.8	3.7	129.0	1.6	59.1[1]	~ 400	122	80
5	57.1	2.9	126.0	1.4	53.9	~ 500	122	71
8	51.4	1.9	118.0	1.4	-	-	120.5	127

The exponential decay length defined by equation (1.27) is related to the penetration depth of a particular surface mode into the superlattice. Fig. 1.4 (b) and

(c) show the strain patterns of the first two surface modes of Au(5 nm)/Al_2O_3(45 nm) multilayer. In a study of metallic multilayers[48], it was suggested that the most likely source of damping of the surface modes is a process that occurs at the free surface of the structure. It is related to the scattering and absorption of phonons at surfaces. Qualitatively, the surface mode is considered to be a wave that travels into the structure a distance on the order of the exponential decay length l (see Eq. (1.27)), and then returns to the surface of the multilayer where it is reflected. Let v be the velocity of the wave, then this wave undergoes on the order of $v/2l$ reflections at the free surface in unit time. Assuming the reflection coefficient r is less then 1, the attenuation of the surface mode per unit time can be expressed in the form[48]

$$\alpha = (1 - r)\frac{v}{2l}. \tag{4.2}$$

So the attenuation rate is inversely proportional to the decay length and it is also the inverse of the decay time τ. That means that the longer the decay length of a given surface mode is, the longer its decay time should be. Assuming v and r do no vary significantly with varying Au layer thickness, we can make a comparison between the different superlattices. In the data on the second surface mode in Table IV.1, the trend of longer decay length means longer decay time, is not observed. This implies that the damping of the second surface mode in these samples is not driven by the scattering and absorption of the phonons at the free surface. The damping is likely dominated by scattering at the nanoparticle Au films. Since data for the first surface mode are available only for two samples, it is not possible to make a similar conclusion

about the causes of its damping, but it can be seen that the first surface mode decays more slowly then the second one. This is mainly due to the lower frequency of the first surface mode, which is equivalent to longer wavelengths and therefore less scattering.

There are several possible reasons why the first surface mode is only observed in the 4 and 5 nm Au layer thick samples. The decay lengths of the first mode shown in Table IV.1 are increasing with decreasing Au layer thickness, which means that the modes are extending deeper into the superlattice. However, our multilayers have only 10 periods, which might not be enough for the first surface mode in the 2 and 3 nm Au layer thick samples. Further, we used the equations (1.35) and (1.38) to evaluate the optical excitability and detectability of the surface modes. However, in order to be able to calculate the excitability of the surface modes, the superlattices have to be modeled and the thermal stress $\sigma_T(z,t)$, which is needed in Eq. (1.35), calculated.

The finite element analysis (COMSOL) was used to model the multilayer structures. Figure 4.9 shows an example of the temperature distribution of the Au(5 nm)/Al_2O_3(45 nm) superlattice right after the heat pulse. The heating of the Au layers in the model was chosen so that it corresponds to the experimental conditions such as light absorption in each Au layer and the thermal stress onset time of 1 ps. In general, the model is 2D because of the computational limits. The cross section of the superlattice is the main input into the model. The size of the modeled area is a variable parameter, but increasing it also rapidly increases the time it takes to finish the computation. The structural mechanics and heat transfer modules of the COMSOL multiphysics software was used in modeling. The structural mechanics module models the stress and strain generation by thermal expansion and their time evolu-

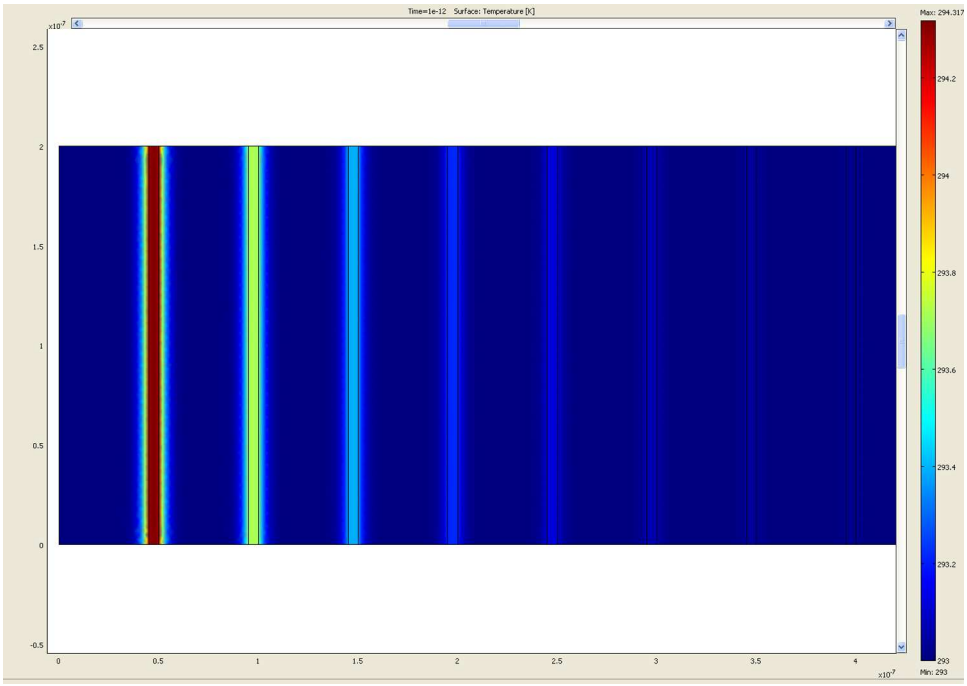

Figure 4.9: Temperature distribution in the Au(5 nm)/Al_2O_3(45 nm) superlattice at the end of heat pulse t = 1 ps.

tion. The heat transfer module models the heating of the Au layers, based on the experimental absorption of the pump laser pulse, and also models the temperature time evolution in the whole multilayer. The Au films were modeled as continuous films with sharp interfaces and bulk gold properties, such as density, thermal expansion, conductivity and Young's modulus, were used. In case of the Al_2O_3 films, bulk sapphire properties were used for the density, thermal expansion and conductivity, however Young's modulus was derived from the experimentally measured sound velocity. Separate boundary conditions were set up for the heat transfer and structural modules. In order to keep the model simple and manageable, the boundary condition was set to *thermal insulation* on the outside edges of the modeled multilayer.

This is a reasonable assumption because only a small central part of the pulse laser affected area is modeled, which is not influenced by the heat diffusion on the laser beam edges within the simulated time (< 200 ps). The heat diffusion at the free surface is neglected because the temperature rise is usually very small (< 2 K, see Fig. 4.10). The outside edge boundary condition was set to *free* for the stress (strain) calculation, meaning the edges can move freely without any external forces applied. At first, setting *fixed* was used, but then all the stress was concentrated near the edges and corners of the modeled volume, making the observation of the strain pulse propagation impossible. The *free* boundary condition should not significantly affect the strain pulse propagation in the direction normal to the surface, taking again into consideration the fact that just the central part of the laser pulse heated area is modeled.

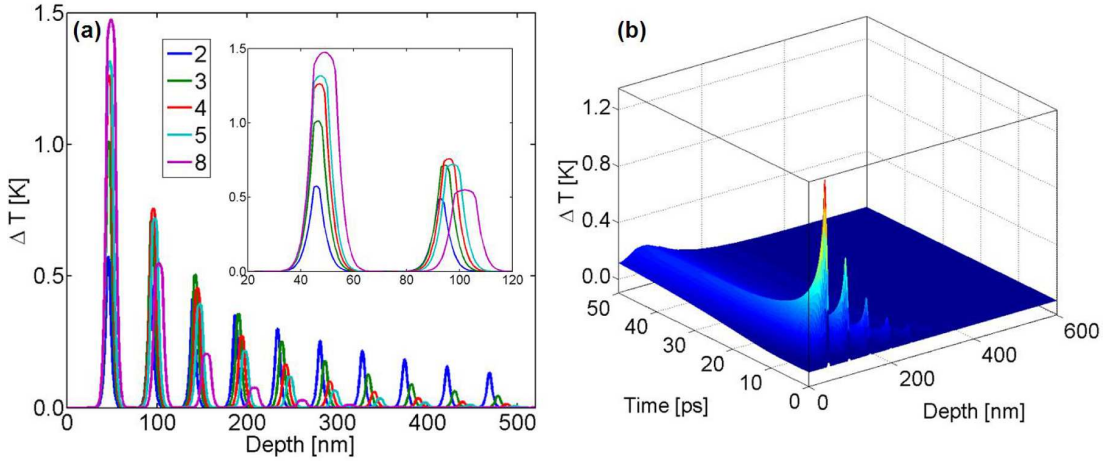

Figure 4.10: (a) Comparison between the temperature change ΔT of the Au/Al_2O_3(45 nm) superlattices at the end of heat pulse t = 1 ps. Inset: Zoomed in region of the first two Au layers. (b) 3D plot of the temperature distribution in Au(5 nm)/Al_2O_3(45 nm) superlattice.

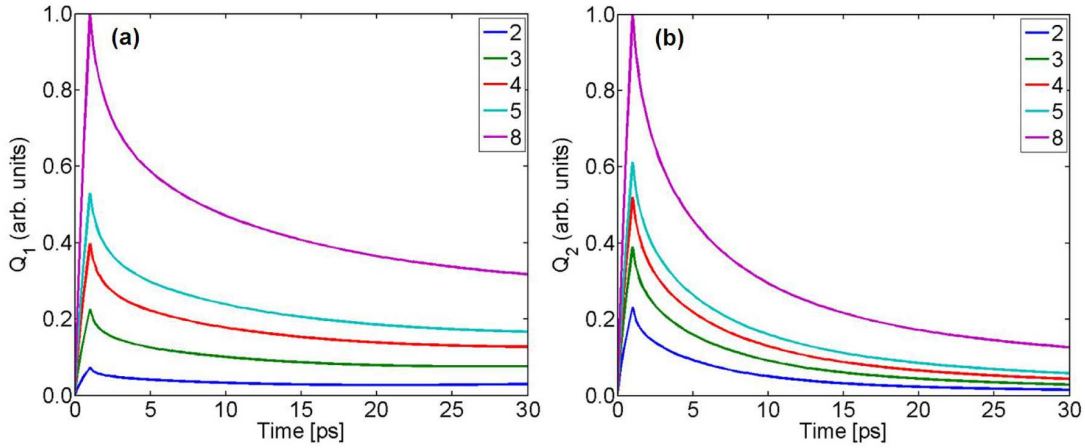

Figure 4.11: Excitability $Q_n(t)$ of the first (a) and second (b) surface mode of the Au/Al_2O_3(45 nm) superlattices.

Each experimental superlattice was also modeled using COMSOL. Figure 4.10(a) shows a comparison between the temperature change ΔT of the Au/Al_2O_3(45 nm) superlattices at the end of the heat pulse t = 1 ps, which is when the maximum temperature rise occurs. Part (b) of the same figure shows an example 3D plot of the temperature distribution. The obtained temperature difference $\delta T(z,t)$ was used to calculate the thermal stress $\sigma_T(z,t)$ using Eq. (1.29). The thermal stress was then used in Eq. (1.35) to numerically calculate $Q_n(t)$. The excitability $Q_n(t)$ of the first and second surface mode of the studied superlattices is plotted in Fig. 4.11(a) and (b), respectively. The data are normalized to the maximum value of the respective surface mode excitabilities of the Au(5 nm)/Al_2O_3(45 nm) superlattice. The temporal evolution of $Q_n(t)$ is very similar among different superallitces, only the intensity seems to be increasing with Au layer thickness. Notice that the maximum

of the optical excitability increases more rapidly for the first surface mode. This can be observed also in Table IV.2, where the maximum values of Q_n normalized to the maximum values of 8 nm Au layers Q_{n_8} are shown. The ratio of the excitability between the surface modes favors the second one, $Q_2/Q_1 \approx 6$. The trend seen in the optical excitability is also observed in the optical detectability (see Table IV.2) which was calculated using Eq. (1.38). Overall, the optical excitability and detectability provide another possible explanation why is the first surface mode observed only in the 4 and 5 nm Au layer thick samples. However, they contradict the data from the 8 nm Au layer thick sample. No first surface mode is observed in this superlattice and the second surface mode is very weak, comparable to the 2 nm sample. The origin of this discrepancy is likely related to the fact that at 8 nm thickness, Au layers are becoming continuous. This influences the thermal relaxation process, which is indicated by a different slope of the after transient pump-probe signal in Fig. 4.8. This result is however not yet fully understood.

The surface modes that lie in the phononic band gap are not the only modes that can be excited and detected in the superlattice structure. The normal modes with real q can be excited simultaneously with them as well. In a perfect multilayer with sharp interfaces, these normal modes are Bloch waves. They propagate freely without any scattering or reflections at the interfaces. In the case of a semi-infinite superlattice, the normal modes propagate into the film and are not detected since they leave the detection sensitive surface region. However, in the case of finite superlattices the normal modes can get reflected from the substrate interface and return to the surface where they can be detected. We observe such modes in our Au(5 nm)/Al_2O_3(45 nm)

Table IV.2: Excitability and detectability of the surface modes. Excitability is time dependent function, so only its maximum from within first 50 ps window is presented. For comparison, all values are normalized to the values of Au(8 nm)/Al_2O_3(45 nm) superlattice.

d_{Au} (nm)	$\frac{Q_{1_M}}{Q_{1_{M_8}}}$	$\frac{Q_{2_M}}{Q_{2_{M_8}}}$	$\frac{F_1}{F_{1_8}}$	$\frac{F_1}{F_{1_8}}$
2	0.07	0.23	0.15	0.47
3	0.23	0.39	0.25	0.53
4	0.40	0.52	0.42	0.6
5	0.53	0.61	0.58	0.69
8	1	1	1	1

sample. Figure 4.12 shows the background-subtracted signal past the fast transient peak. The signal was fitted using a least squares fitting routine and was successfully decomposed into an exponentially decaying cosine function representing the first surface mode and the two echoes that represent the propagating normal modes arriving at the surface after being reflected at the substrate interface. The Fourier transform is used to analyze the frequency components of the measured signal (Fig. 4.13). The sharp peak of the first surface mode and the broader peak of the second surface mode can be easily identified in Fig. 4.13. The broad peak at lower frequencies below the first surface mode represents the propagating normal modes that consist of the modes on the lowest minibranch of the zone-folded longitudinal phonon dispersion curve shown in Fig. 1.3. The Fourier transform of the echo signal alone, shown in Fig. 4.13 as a dashed curve, confirms that the broad peak consists of these normal modes.

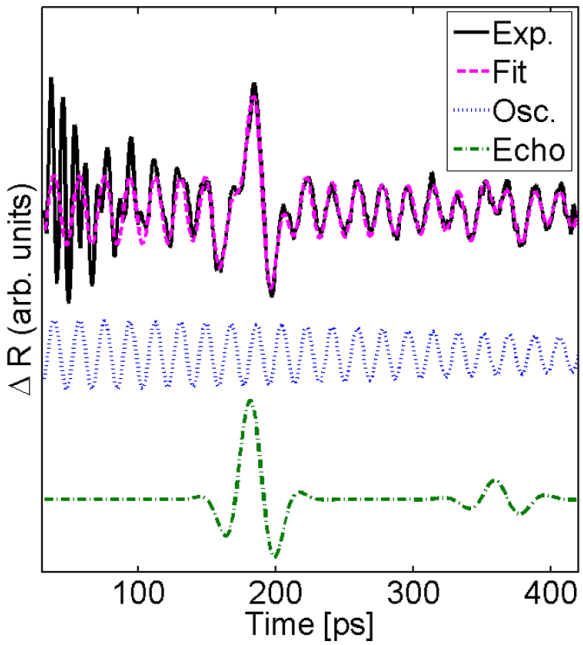

Figure 4.12: Zoomed-in oscillatory trace with thermal signal subtracted of Au(5 nm)/Al_2O_3(45 nm) superlattice and its fit. Fitted curve, obtained using least squares fitting, is decomposed into its exponentially decaying cosine function (Osci. - dotted curve) and the two echoes (Echo - dot-dashed curve).

The main cause of the decreasing amplitude of the echoes is the reflection at the Al_2O_3/SiO_2 interface. The acoustic reflection coefficient r is defined in Eq. (4.1). Using these values for the density and velocity of sound for fused silica $\rho_{SiO_2} = 2.2$ g/cm^3 and $v_{SiO_2} = 5.97$ nm/ps[77], the calculated reflection coefficient is -0.38. The minus sign means there is a π phase shift during the reflection. The ratio of the amplitudes of the second echo to the first one is only 0.2, which suggests there is another damping mechanism that attenuates the stress pulse as it propagates in the superlattice. The most likely cause of this attenuation is the phonon scattering at the Au layers.

The normal modes travel through the superlattice at an effective sound velocity given by[42] Eq. (1.22). The evaluation of that expression for our Au(5 nm)/Al_2O_3(45 nm) superlattice yields 6.2 nm/ps. It is possible to compare this to an experimental value obtained from the ratio $2l/t$, where l is the thickness of the whole superlattice and t is the time difference between the two echoes. The thickness of the superlattice, measured by profilometry, is $l = 540 \pm 20$ nm. The echoes are separated by $t = 179.4 \pm 4$ ps. That leads to the effective sound velocity of 6 ± 0.3 nm/ps. Within the margin of error, this is in agreement with the theoretical prediction.

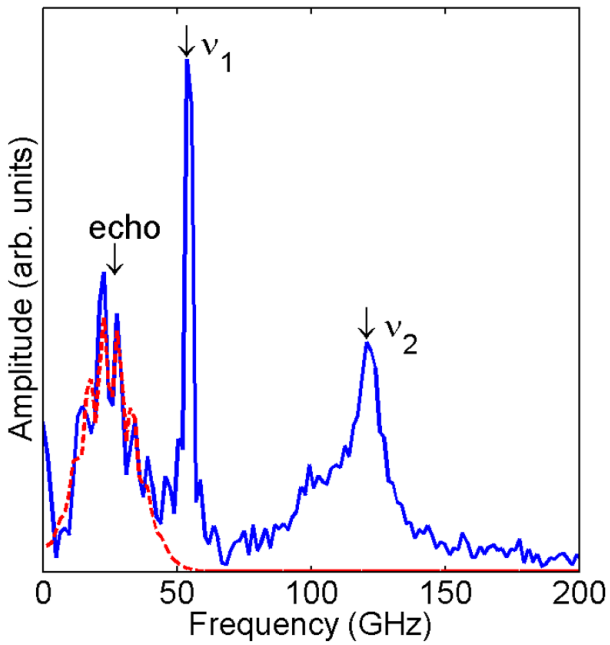

Figure 4.13: The Fourier transform spectra of the background subtracted signal of the Au(5 nm)/Al_2O_3(45 nm) superlattice. The dashed curve represents the Fourier transform of the echo signal only.

4.2.2 Al_2O_3 layer thickness effects

In addition to the study of the effects of varying Au layer thickness reported in previous section, a similar study was performed on samples with varying Al_2O_3 layer thickness. However, before we discovered that with the Au layer thickness of 5 nm the first surface mode can be easily observed, a set of samples with only 2 nm thick gold layers was prepared. Therefore, only the second surface mode was observed in these samples. Originally, the planned thicknesses of the Al_2O_3 layers were supposed to be 10, 20, 30 and 40 nm and during the deposition the quartz crystal thickness monitor (QCM) was showing these values. Only later we realized that the QCM was not calibrated for Al_2O_3 deposition before, so the tooling factor was not known. It resulted in all Al_2O_3 films being thicker by $\sim 60\%$. The profilometer was used to determine the thickness of the Al_2O_3 layers. The actual thicknesses are 17, 30, 45 and 58 nm.

The transient signals $\Delta R(t)$ are shown in Fig. 4.14 and Fig. 4.15. The data were obtained using the laser at 740 nm wavelength and 40mW pump power. The fitting procedures used were the same as for the varying Au layer thickness samples. The left columns of the Figs. 4.14 and 4.15 display the first 40 ps of the transient signals for the superlattices together with their fits and with the extracted rise and fall times. The rise and fall times vary only a little among different samples. However, notice the significant difference between the fall times reported here ($\sim 0.8ps$) and the fall times shown in Figs. 4.6 and 4.7 ($\sim 1.3ps$). Since the fall time is a measure of the electron-phonon interaction, it should not be affected by the wavelength of the light

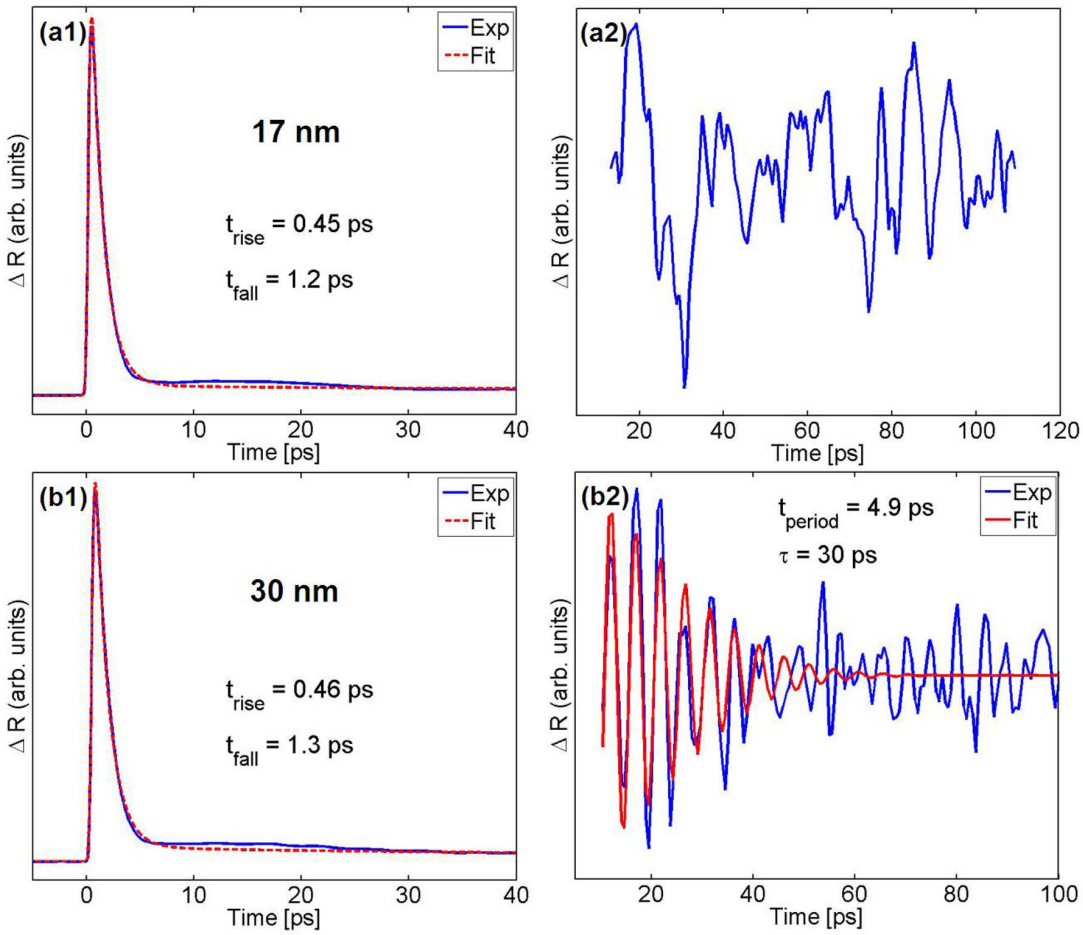

Figure 4.14: (a1) and (b1) show the measured $\Delta R(t)$ for Au(2 nm)/Al_2O_3(17 and 30 nm) superlattices together with the fitted curves and the obtained rise and fall times. Thermal background subtracted oscillatory part of the signal fitted with exponentially decaying cosine function (b2). Also shown is the period of the oscillation and the decay rate extracted from the fit.

used for such measurement. On the other hand, looking at the optical spectra of these samples (Fig. 4.16), it is clear that by shifting the pump wavelength from 830 nm to 740 nm, the absorption of the films increased significantly due to moving closer to the surface plasmon resonance peak. So at the same pump power of 40 mW, the excitation of the Au layers is stronger at 740 nm and consequently the relaxation

through e-p interaction takes longer.

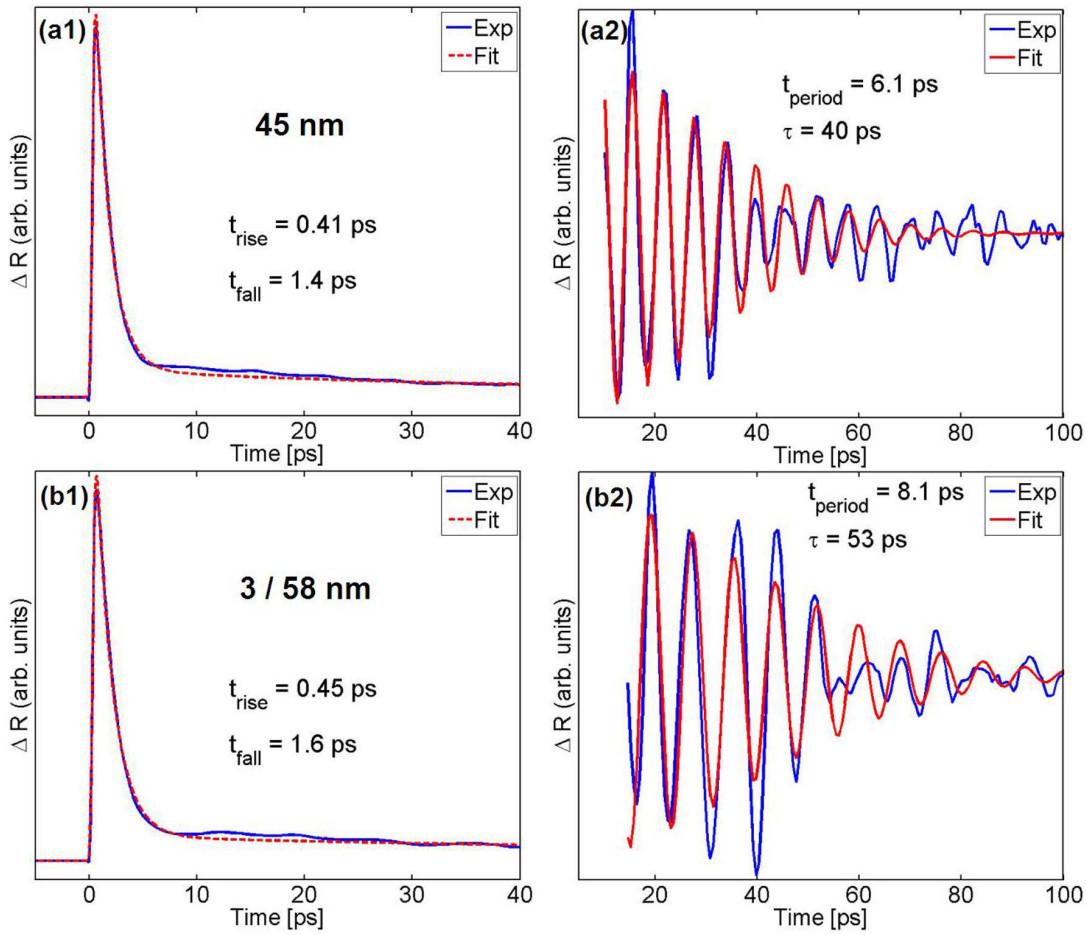

Figure 4.15: (a1) and (b1) show the measured $\Delta R(t)$ for Au(2 and 3 nm)/Al_2O_3(45 and 58 nm) superlattices together with the fitted curves and the obtained rise and fall times. Thermal background subtracted oscillatory part of the signals fitted with exponentially decaying cosine function (a2 and b2). Also shown is the period of the oscillation and the decay rate extracted from the fit.

Figure 4.16 does not include the spectrum of the Au(3 nm)/Al_2O_3(58 nm) sample because of its thicker Au layers. The SPR peak at ∼650 nm is a dominant feature of the spectra. However, there are slight differences between the samples even though they contain the same amount of Au. Our experience with annealing of Au/dielectric composites suggests that the SPR peak intensity is related to the size of the nanoparticles, so that stronger peak means bigger nanoparticles. This would suggest that the sample with the thinnest Al_2O_3 (17 nm) films has the largest particles. It is likely the consequence of larger surface roughness of the thinner Al_2O_3 films, which promotes the nucleation and growth of the nanoparticles.

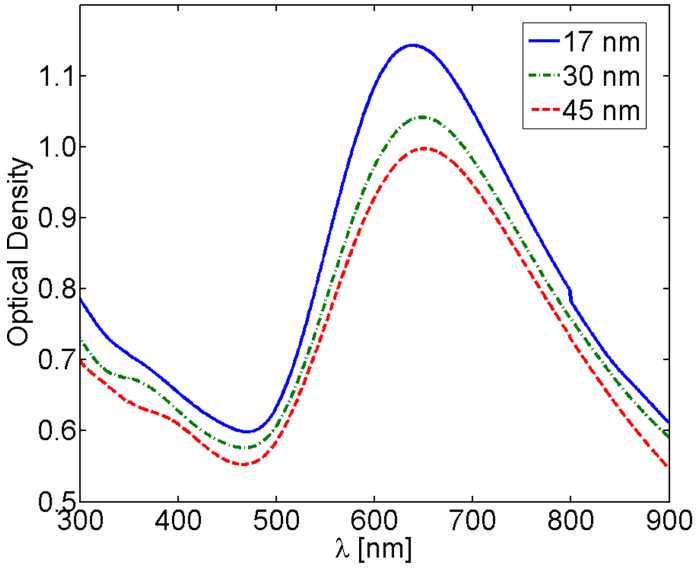

Figure 4.16: Optical spectra of the superlattices with various Al_2O_3 layer thicknesses. The legend represents the Al_2O_3 layer thickness in nm.

The right columns of the Figs. 4.14 and 4.15 display the part of the transient

signal starting at 5 (or more) ps with the slow photothermal response removed by smoothing. No first surface modes are detected in these samples. The cause of that was extensively discussed in previous section. The oscillations, which are related to the second surface mode, are observed in samples with thicker Al_2O_3 layers. However, no oscillation was detected in the sample with 17 nm thick Al_2O_3 films (Fig. 4.14(a2)). This is probably due to the rather high frequency of the second surface mode in this sample (Tab. IV.3), which leads to so low excitability, that the mode can not be detected. For the other samples, exponentially decaying cosine function was used to fit the oscillatory signals. The extracted period of the oscillations and the decay time τ are shown. In general, the fitted curves overlap with the experimental data well.

Table IV.3: Theoretical and experimental surface-mode frequencies of Au(2 nm)/Al_2O_3 superlattices. $d_{Al_2O_3}$ is the alumina layer thickness. ν_1 and ν_2 are the frequencies of the first and second surface mode, respectively. l_1 and l_2 are their decay lengths. d is the repeat distance. τ_2 is the decay time of the second surface mode. [2]The Au layer thickness is 3 nm.

	Theory				*Experiment*	
$d_{Al_2O_3}$ (nm)	ν_1 (GHz)	$\frac{l_1}{\mathrm{d}}$	ν_2 (GHz)	$\frac{l_2}{\mathrm{d}}$	ν_2 (GHz)	τ_2 (ps)
17	149	2.7	331	1.4	-	-
30	95	5.2	200	2.0	204	30
45	67.6	9.2	139	3.0	164	40
58[2]	51.2	7.4	106	2.5	123.5	53

The periods, obtained from fitting, are converted to frequencies and then compared to the theoretical calculations in Table IV.3. In the case of 30 nm thick Al_2O_3

layer sample, the experimental frequency ν_{exp} agrees very well with the theoretical one ν_{th}. This is an unexpected result, because a large discrepancy was observed previously in the Au(2 nm)/Al_2O_3(45 nm) sample which was attributed to the nanoparticle structure of the Au layers. Here, the data from the two samples with thicker Al_2O_3 layers also have large discrepancy, as expected. The second surface mode frequency for the Au(2 nm)/Al_2O_3(45 nm) sample reported here (164 GHz) is slightly different from the frequency obtained using 830 nm wavelength (172.4 GHz, Tab. IV.1). This deviation could be caused by the change in excitation intensity due to the absorption difference at the given wavelengths, even though our pump power dependence measurements at 830 nm wavelength do not detect any change in the surface mode frequency. Other possible cause of the deviation is the close presence of the surface plasmon resonance. One might also suggest the wavelength, but our extensive wavelength dependent measurements of the Au(5 nm)/Al_2O_3(45 nm) sample (Tab. IV.4) did not detect any dependence of the first or second surface mode frequency on

Table IV.4: Wavelength dependence of the surface-mode frequencies of Au(5 nm)/Al_2O_3(45 nm) superlattice. ν_1 and ν_2 are the frequencies of the first and second surface mode, respectively.

λ (nm)	ν_1 (GHz)	ν_2 (GHz)
740	54.9	125.9
770	54.5	122.4
790	54.4	122.5
810	54.4	123.5
830	54.5	122.9
850	54.5	123.3

pump-probe wavelength.

4.3 Ag/Al_2O_3 superlattices

Two superlattices, where Au is replaced with Ag and Al_2O_3 layer thickness is 45 nm, were fabricated in order to look at the effects of changing elastic properties of the metal layers. The bulk properties of Ag used in calculations are density $\rho = 10.49$ g/cm^3 and sound velocity $v_s = 2.6$ nm/ps. From the theoretical point of view, a very interesting situation occurs. The acoustic impedance of silver ($Z_{Ag} = 27.3$) is slightly smaller than the impedance of Al_2O_3 ($Z_{Al_2O_3} = 29$). According to the theory (Sec. 1.3), no surface modes should exist in such structure. However, as can be seen in Fig. 4.17, the second surface mode was detected in both samples. The possible reasons for observing the surface mode are the uncertainty in determination of the sound velocity of Al_2O_3 layers and the nanoparticle structure of the Ag layers, which is apparent in the strong purple coloration of both samples and in the related optical spectra (Fig. 4.18). The SPR peak for single silver nanoparticle is usually narrow and at around 400 nm wavelength, but the peaks in the spectra are broad and heavily red shifted. This is due to the interaction among nanoparticles within each Ag layer.

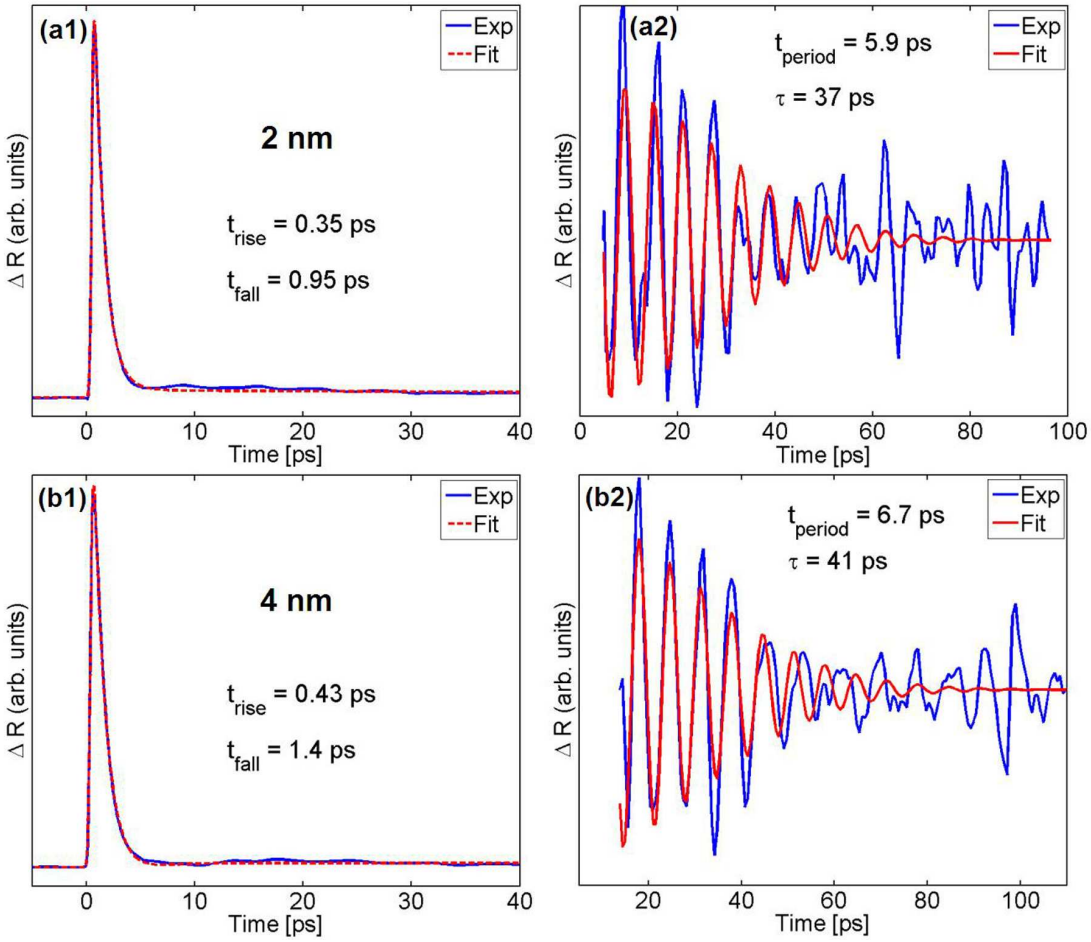

Figure 4.17: (a1) and (b1) show the measured $\Delta R(t)$ for Ag(2 and 4 nm)/Al_2O_3(45 nm) superlattices together with the fitted curves and the obtained rise and fall times. Thermal background subtracted oscillatory part of the signals fitted with exponentially decaying cosine function are shown in (a2) and (b2). Also shown is the period of the oscillation and the decay rate extracted from the fit.

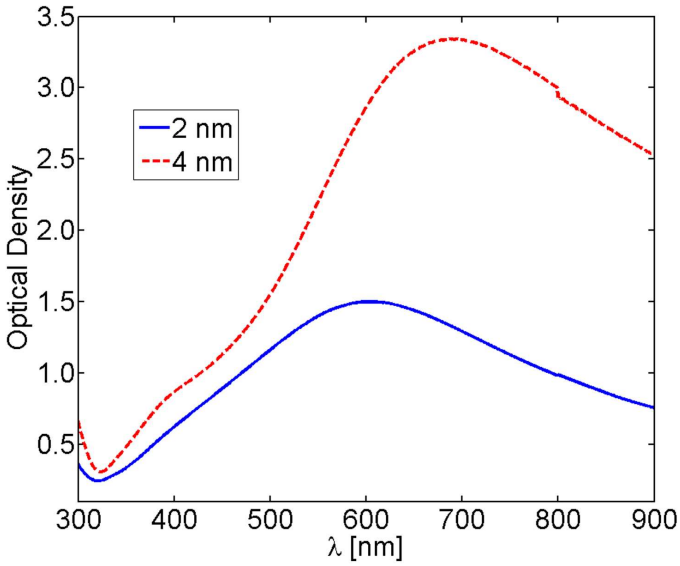

Figure 4.18: Optical spectra of the Ag(2 and 4 nm)/Al_2O_3(45 nm) superlattices. The legend represents the Ag layer thickness in nm.

Figure 4.17 shows the transient signals together with their fits. The wavelength of 740 nm and 40 mW pump power were used to obtain these data. The fall time of the sample with 4 nm thick Ag layers is noticeably longer, which is mainly due to significantly stronger absorption at the given wavelength (see Fig. 4.18). The experimentally determined frequencies of the second surface mode are 169.5 and 149.3 GHz for the samples with 2 and 4 nm Ag thick layers, respectively. The surface mode theory for semi-infinite superlattice can not be used to calculate the mode frequencies because of the fact that Ag impedance is smaller then the impedance of the Al_2O_3, which is the top most layer in all our superlattices. However, the dispersion relation (1.21) can be used to find at least the position of the zone center band gap, which is where the second surface mode should be. The middle frequencies of the first zone

center band gap are 144.3 and 129.7 GHz in the 2 and 4 nm thick Ag layer samples, respectively, while the width of the bang gaps is less then 4 GHz. That means there exists quite large discrepancy between the experimental results and the theory. The possible causes are again the nanoparticle structure of the metal layers and its effects on their apparent elastic properties, and the before mentioned uncertainty in the measured value of Al_2O_3 sound velocity.

4.4 Annealing effects

A set of Au(1 and 2 nm)/Al_2O_3(20 and 40 nm) multilayers was prepared before the other superlattices to study the effects of annealing on their optical properties. These samples were not perfect superlattices because the thickness of the Al_2O_3 layers at the substrate and on the top was always 50 nm regardless of thickness of the layers between the metal films. They contain only 8 Au layers. The samples were cut using a low speed saw with a diamond blade into several pieces. A piece of each sample was then annealed in a furnace at 900°C for 2 hours. One set was annealed in oxygen (O_2) atmosphere and another one in argon (Ar). In general, no significant difference was observed between the two annealing atmospheres. Figure 4.19 shows the optical spectra of the Au(2 nm)/Al_2O_3(40 nm) superlattice before and after O_2 annealing. The SPR peak of Au nanoparticles increases a little and gets narrower after annealing. This suggests that the nanoparticles grow slightly and they become more homogeneous in size.

Very interesting phenomenon was observed when the transient time-resolved spectroscopy was applied to the samples with 2 nm thick Au layers. Figure 4.20 shows

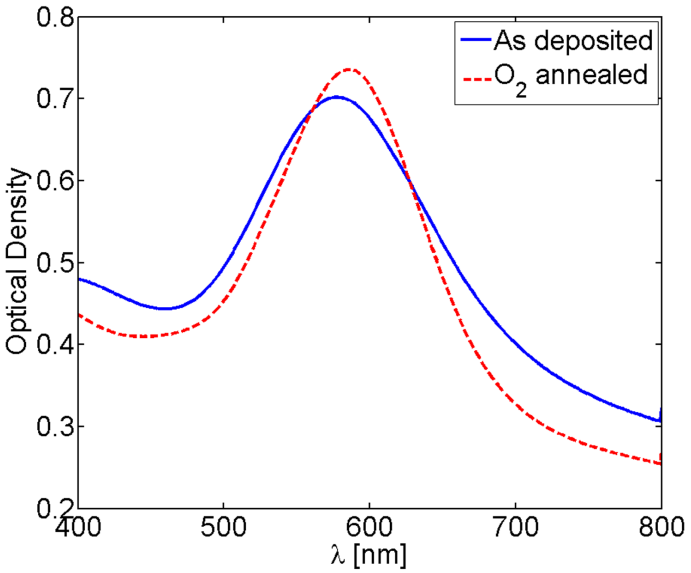

Figure 4.19: Optical spectra of the Au(2 nm)/Al_2O_3(40 nm) superlattice. Comparison between as deposited and O_2 annealed sample.

the transient signals of as deposited (not annealed)(a1,a2) and O_2 annealed (b1,b2) Au(2 nm)/Al_2O_3(40 nm) multilayer. The measurements were done using 770 nm wavelength in transmission configuration. Notice that the oscillatory signal of a surface mode is observed in as deposited sample (Fig. 4.20(a2)), even though the top Al_2O_3 layer is of slightly different thickness. Furthermore, no oscillation is detected in annealed sample even if FFT analysis is used (Fig. 4.20(b2)). There is also a significant change in the fast transient part of the pump-probe data. This suggest that the annealing modified the interaction (interface) between the Au nanoparticles and the surrounding matrix. Interestingly, the transient signal of the annealed sample greatly resembles the signal from as deposited Au(8 nm)/Al_2O_3(45 nm) superlattice (Fig. 4.7(b1)). These signals are directly compared in Fig. 4.21. The similarities are the

fall time and the slow decay of the thermal signal after the fast transient. However, there are a lot of sample and measurement related differences such as 2 nm thick Au layers *vs* 8 nm, measured in transmission *vs* reflection and the used wavelength of 770 nm *vs* 740 nm. So the apparent effect of annealing is that it makes the transient response of 2 nm Au films similar to as deposited 8 nm Au films.

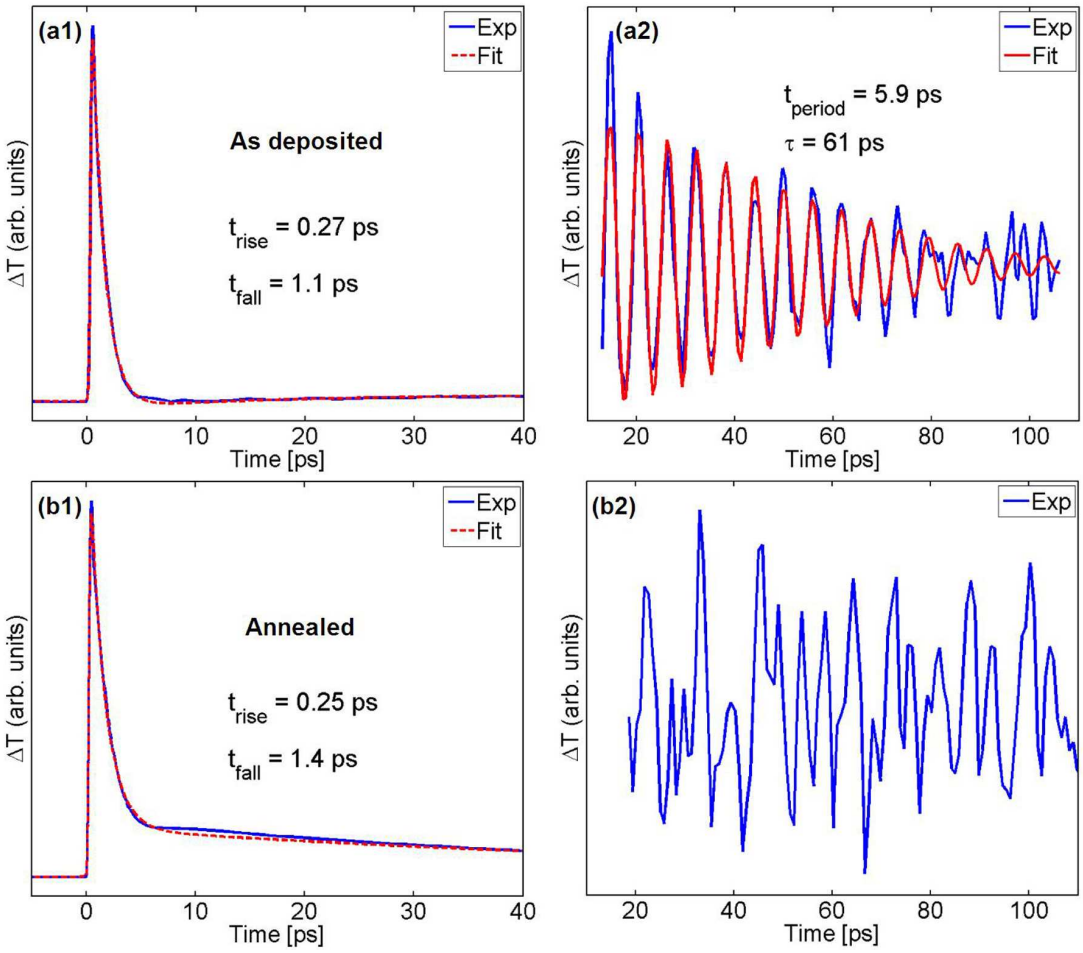

Figure 4.20: (a1) and (b1) show the measured $\Delta T(t)$ of the as deposited and O_2 annealed Au(2 nm)/Al_2O_3(40 nm) superlattice, respectively. The oscillatory part of the signal for the as deposited sample fitted with exponentially decaying cosine function is shown in (a2). No oscillation is detected in the annealed sample (b2).

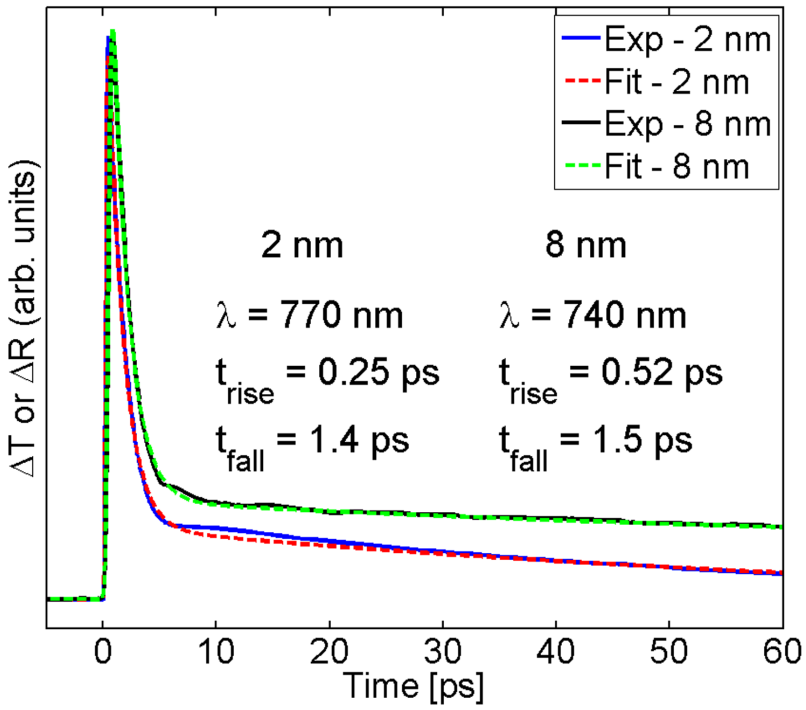

Figure 4.21: Comparison between the pump-probe signals of the O_2 annealed Au(2 nm)/Al_2O_3(40 nm) superlattice and the as deposited Au(8 nm)/Al_2O_3(45 nm) superlattice.

TEM analysis was utilized to help us understand the annealing effects. Figure 4.22 shows a comparison between as deposited Au(2 nm)/Al_2O_3(20 nm) multilayer (left) and O_2 annealed Au(2 nm)/Al_2O_3(40 nm) sample (right). The Au(2 nm)/Al_2O_3(20 nm) sample was analyzed right after deposition and then later on after annealing the sample with thicker Al_2O_3(40 nm) layers was chosen for analysis by mistake. However, the transient signals are nearly identical for the annealed Au(2 nm)/Al_2O_3(20 and 40 nm) samples. It is also assumed that the structure of the multilayers is not strongly affected by the thickness of the Al_2O_3 layers, so we think the comparison is possible. The main differences between the two TEM images are that the Au nanoparticles are

bigger in the annealed sample and there are also small bright patches in Al_2O_3 layers. The growth of the nanoparticles was expected and is also supported by the optical spectra (Fig. 4.19). The hypothesis about the bright patches is that they are areas of crystalline growth of Al_2O_3.

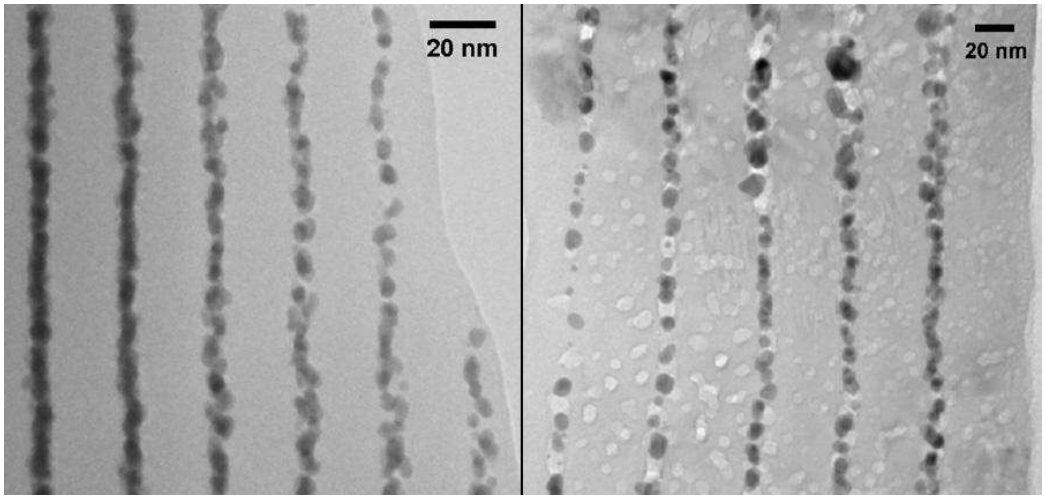

Figure 4.22: Cross-sectional TEM images. Left: Au(2 nm)/Al_2O_3(20 nm) as deposited multilayer. Right: Au(2 nm)/Al_2O_3(40 nm) O_2 annealed multilayer. The surface is parallel to the Au layers.

The existence of little crystals of Al_2O_3 within otherwise amorphous Al_2O_3 layers gives a possible explanation for the disappearance of the surface mode in the annealed Au(2 nm)/Al_2O_3(40 nm) sample. The Al_2O_3 layers become inhomogeneous and the crystals act as strong phonon scatterers, which can negatively affect coherent phonons. X-ray diffraction (XRD) was used to look for signs of crystallinity. Figure 4.23 shows 2θ scans of the as deposited and annealed Au(2 nm)/Al_2O_3(40 nm) superlattice together with a scan of the fused silica SiO_2 substrate. The result of annealing

is the growth of rather small and broad peak at 38°. This is a clear sign of a change in the crystalline structure of the sample, but it is not conclusive. The detection of several and much stronger peaks was expected, if those bright patches were assumed to be small Al_2O_3 crystals.

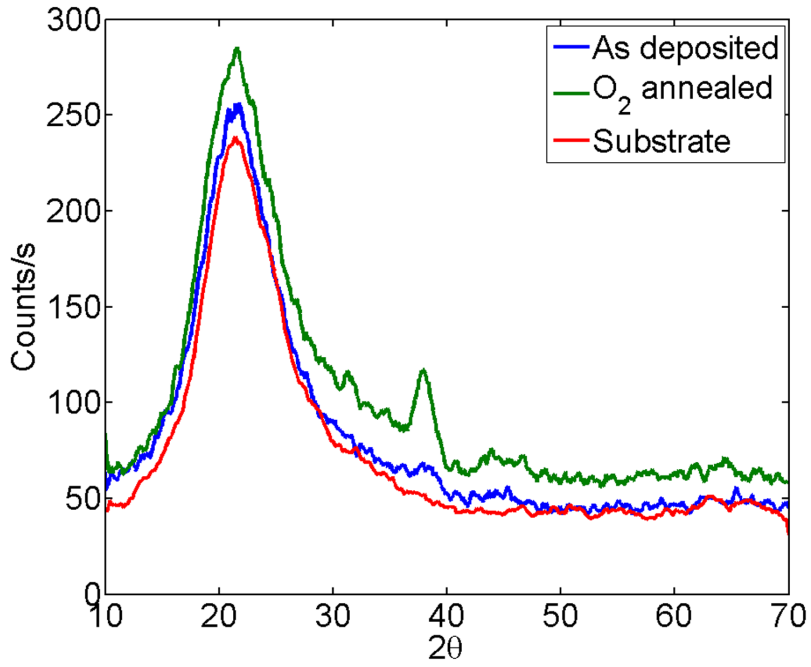

Figure 4.23: XRD spectra of the Au(2 nm)/Al_2O_3(40 nm) superlattice. Comparison between as deposited and O_2 annealed sample.

In addition to the crystalline structure of the Al_2O_3 layers, the annealing process seems to affect also the interface between the Au nanoparticles and the surrounding Al_2O_3 matrix. The change is observed in the long transient thermal decay of the annealed samples. As mentioned previously, this is similar to the response of a thick 8nm Au layer, which suggests that the metal/dielectric interfaces in these samples

are comparable. The experimental results indicate that the heat transfer across the metal/dielectric interface was worsened by annealing. That could negatively affect also the thermal stress coupling, which is another possible reason why the surface mode in the Au(2 nm)/Al_2O_3(40 nm) superlattice is not detected after annealing.

4.5 Conclusions

We performed a comprehensive study of metal/dielectric superlattices. The metals Au and Ag were used and Al_2O_3 was used as dielectric in our study. Several sets of multilayer films were prepared. At first, the interest was in optical properties and their possible modification by annealing. Later on, after the application of the ultrafast time-resolved spectroscopy and observation of an unexpected oscillatory signals, the existence of the surface mode vibrations in superlattice structures was understood to be the cause of the oscillations, which initiated the study of the metal and dielectric film thickness effects on these surface modes. Sets of samples with varying metal and dielectric film thickness were prepared. The samples were also analyzed using several other experimental techniques such as TEM, XRD and optical spectroscopy, to help us better understand the vibrational properties of the multilayer structures. Finite element modeling in COMSOL multiphysics software was used to simulate the thermal and structural behavior of the superlattices and the obtained data were used to evaluate the excitability and detectability of the surface modes. In order to make the modeling as realistic as possible, the elastic properties of the Al_2O_3 layers were also measured using time-resolved spectroscopy.

The Au(1 and 2 nm)/Al_2O_3(20 and 40 nm) samples were used to study the an-

nealing effects. The growth of the nanoparticles which constitute the Au layers was observed. Optical spectra also suggest that their size distribution becomes narrower. TEM and XRD analysis indicate a change in crystallinity of the multilayer occurs during annealing with small crystallites growing within Al_2O_3 layers. This is a possible reason why the surface mode is observed in as deposited Au(2 nm)/Al_2O_3(40 nm) sample, but not in annealed one. Further, the transient data suggest that the thermal coupling between the metal and surrounding dielectric matrix deteriorated during annealing.

Since our study focused mainly on Au/Al_2O_3 multilayers, only two samples where prepared, where Au was replaced by Ag. Only the second surface mode was observed in these samples, even though theoretically it should not be there since the acoustic impedance of Ag is smaller then the impedance of Al_2O_3. The possible cause of that is the nanoparticle structure of Ag films, which is strongly indicated by the surface plasmon resonance peak observed in the optical spectra. The preparation of large sets of samples at once has its disadvantages. Especially, when an interesting result from one set asks for a parameter change in the other, but such change is not possible any more because all samples are already prepared. This happened with the set of superlattices with varying thickness of Al_2O_3 layers. The thickness of the Au films was chosen to be 2 nm in this set. However, after measuring very interesting data with the Au(5 nm)/Al_2O_3(45 nm) sample, we would definitely opt for 5 nm thick Au layers. So, only the second surface modes were observed, but not in all samples. The mode was not detected in the sample with thinnest Al_2O_3 (17 nm) layers, probably due to its high frequency. There is a significant discrepancy between theory and

experiment for the samples with thicker Al_2O_3 (45 and 58 nm) layers, which is likely caused again by the nanoparticle structure of the metal layers.

The time-resolved pump-probe technique was successfully applied to study the surface acoustic modes of Au/Al_2O_3 multilayers with different Au layer thicknesses (2 to 8 nm). The second surface mode was observed in all samples, but the first surface mode was observed only in the samples with the 4 and 5 nm thick Au layers. The frequency of these modes was compared to the theory calculation and good agreement was generally found. The slight differences are not attributed to the softening of the effective longitudinal elastic constant, but to the effect of the nanoparticle structure of the Au films. The analytical expressions for the detectability and excitability were evaluated and provide an insight into the reasons why the first surface mode is observed only in the samples with thicker Au layers. However, the first surface mode is not detected in the sample with the thickest 8 nm Au layers. This is probably due to a different interaction between the metal and its dielectric surrounding, which is indicated by the altered transient signal. In addition to the surface modes, the normal phonon modes were observed in the $Au(5\ nm)/Al_2O_3(45\ nm)$ superlattice. They belong to the lowest minibranch of the zone-folded longitudinal phonon dispersion curve and travel in the form of a propagating pulse, which is reflected at the substrate and surface interfaces. Detecting two echoes of the pulse allowed us to experimentally determine the effective sound velocity in the superlattice.

The ultrafast pump-probe spectroscopy proved to be a very useful and effective technique for studying the strain generation and propagation in the metal/dielectric superlattices. It allowed us to study the effects of varying thickness of either con-

stituent of the multilayer structures. Our results show that the theoretical analysis of the superlattices works well for practically all our structures. This supports the usefulness of the theoretical modeling of superlattices in designing structures with predefined positions of the surface mode frequency peaks.

CHAPTER V

SUMMARY AND OUTLOOK

The major accomplishments of this research work are:

- Metal/dielectric composites were prepared by implantation and alternate layer deposition.
- Infrared pulsed laser annealing was used for modification of implanted composites.
- Nucleation and growth of Au nanoparticles in both SiO_2 and Al_2O_3 matrices, and dissolution of Ag nanoparticles in SiO_2 matrix were observed.
- Ultrafast time-resolved spectroscopy was applied to study the vibrational properties of metal/dielectric superlattices and surface acoustic phonon modes were detected in most of them.
- Effects of varying layer thickness of either constituent of the multilayer structures were studied.
- Experimental results were compared to theoretical analysis of acoustic phonon dispersion in superlattices. In general, good agreement was found between theory and experiment.

Superlattice structures are useful in diverse applications. One of the best known uses of the superlattice is a Bragg reflector (BR). In relation to light, it is a superlattice

composed of two materials of contrasting refractive index and thickness $\lambda/4$ that acts as a high quality mirror at normal incidence around the wavelength λ. The ability of the BR to reflect a photon of given wavelength comes from the appearance of the stop band (band gap) in the photon dispersion curve centered at the wavelength λ, which is the result of the periodic stacking. Now, based on the theory describing coherent phonons in superlattices (Section 1.3), similar band gaps are observed in phonon dispersion. Thus, the BR concept can be also applied to acoustic phonons, so that by putting together two mirrors it is possible to create a cavity. In the photon world, such a cavity, also known as Fabry-Pérot resonator, is at the heart of every laser. The main function of a resonant cavity is to provide space for wave propagation within the reflective mirrors, so as to support a standing wave with a particular wavelength, and hence frequency. To be useful, usually one of the mirrors must not reflect perfectly, so that some of the energy can exit the cavity. Applying the cavity concept to phonons could lead to a source of coherent monochromatic phonons.

An intriguing experiment was performed by Trigo *et al.*[81] by placing a phonon cavity inside an optical cavity. It allowed them to perform the first study of interaction between standing-wave photons and standing-wave phonons. Their GaAs/AlAs based structure grown by MBE was probed by Raman scattering experiments and the cavity-confined high frequency hyper-sound mode was successfully observed. This work initiated a lot of interest in acoustic nanocavities[82, 83], which opened the possibility of confinement and amplification of acoustic phonons in a broad spectral range.

The nanocavities are crucial to the development of coherent monochromatic acoustic sources which have potential applications in crystal dynamics studies, phonon

spectroscopy and high-resolution acoustic microscopy. The monochromatic phonon waves could also be used to drive the optical and electronic properties of devices at the picosecond time scale. Even stimulated emission of THz phonons in superlattice nanostructures under vertical electron transport has been reported[84]. This could be the basis of a SASER (sound amplification by stimulated emission of radiation). However, a recent report[85] shows that the thickness fluctuations of just 1/10 of a unit cell of GaAs are the main limitation on the performance of THz phonon cavities. This is discouraging news for metal/dielectric superlattices, since our results show that the interfaces between the two materials are not very smooth. Nevertheless, our results (Chapter IV) also suggest that at the studied frequency range ($<$ 200 GHz) the nanoparticle structure of the metal layers did not significantly affect the overall properties of the superlattices. So it might be an interesting experiment to design and prepare a phonon cavity resonant at $\sim$100 GHz based on metal and dielectric materials, and test its ability to operate as a source of coherent monochromatic phonons.

APPENDIX A

FITTING FUNCTIONS

MATLAB code used for fitting our pump-probe data is presented here. It contains functions for fitting the transient and oscillatory parts.

```
% Function used for fitting the transient part of the pump-probe signal
%%%%%%%%%%%%%%%%%%%%%%%%%%%%%%%%%%%%%%%%%%%%%%%%%%%%%%%%%%%%%%%%%%%%%%%%%%%%

function w = fitpumprobe(xdat,ydat,fitvec,low_fit,up_fit,varargin)

% Experimental data to be fitted
x = xdat; y = ydat;

% Create model for 'fit' function - double exponential
    % A and B are scaling constants
    % tr is the rise time of the transient
    % tau1 and tau2 are the decay constants of the exponential function
    % x0 moves the transient start to t = 0
    % c0 and c1 are offset constants
ppf   = fittype(
'A.*(1+erf(1.81*(x-x0)./tr-tr/(3.62*tau1))).*(exp(-(x-x0)./tau1)) +
B.*(1+erf(1.81*(x-x0)./tr-tr/(3.62*tau2))).*(exp(-(x-x0)./tau2)+c1)
+ c0','independent','x');

% Define specific options of the fit
% Includes initial parameter values and their limits
options = fitoptions('method','nonlinearleastsquares',...
                     'StartPoint',fitvec,...
                     'Lower',low_fit,...
                     'Upper',up_fit,...
                     'MaxFunEvals',2000);

% Call fit function
[fitmodel,goodness,output] = fit(x,y,ppf,options);

% Output
w = fitmodel;
%%%%%%%%%%%%%%%%%%%%%%%%%%%%%%%%%%%%%%%%%%%%%%%%%%%%%%%%%%%%%%%%%%%%%%%%%%%%
```

```
% Function used for fitting the oscillatory part of the pump-probe signal
%%%%%%%%%%%%%%%%%%%%%%%%%%%%%%%%%%%%%%%%%%%%%%%%%%%%%%%%%%%%%%%%%%%%%%%%

function w = fitoscillation(xdat,ydat,fitvec,low_fit,up_fit)

% Experimental data to be fitted
x = xdat; y = ydat;

% Create model for 'fit' function - exponentially decaying cosine
    % A (B,C) is a scaling constant
    % T (T2, T3) is the period of oscillation
    % theta (theta2, theta3) is the phase
    % tau (tau2,tau3) is the decay constant of the exponential function
    % c1 and c2 are offset constants
% Actually, only the first line of this function is needed for simple
% decaying oscillation fitting, the other two are used for echo fitting
% in sample Au(5 nm)/Al2O3(45 nm)
ppf   = fittype(
'A*cos(2*pi*x./T + theta).*exp(-(x)./tau) +
B*cos(2*pi*x./T2 + theta2).*exp(-((x-c1).^2)./(tau2)^2)+
C*cos(2*pi*x./T3 + theta3).*exp(-((x-c2).^2)./(tau3)^2)',
'independent','x');

% Define specific options of the fit
% Includes initial parameter values and their limits
options = fitoptions('method','nonlinearleastsquares',...
                     'StartPoint',fitvec,...
                     'Lower',low_fit,...
                     'Upper',up_fit);

% Call fit function
[fitmodel,goodness,output] = fit(x,y,ppf,options);

% Output
w = fitmodel;
%%%%%%%%%%%%%%%%%%%%%%%%%%%%%%%%%%%%%%%%%%%%%%%%%%%%%%%%%%%%%%%%%%%%%%%%

%%%%%%%%%%%%%%%%%%%%%%%%%%%%%%%%%%%%%%%%%%%%%%%%%%%%%%%%%%%%%%%%%%%%%%%%
% Model analysis of the pump-probe data of Au(5 nm)/Al2O3(45 nm) sample %
% measured at 830 nm wavelength                                         %
%%%%%%%%%%%%%%%%%%%%%%%%%%%%%%%%%%%%%%%%%%%%%%%%%%%%%%%%%%%%%%%%%%%%%%%%

clear all

% Load data
    D = load('5_45_830nm.dat');
```

```
% Assign x, y
    x = D(:,1);
    y = D(:,2);

% Level signal to 0, and bring x = 0 to transient start
    y = y - y(1);
    x = x + 221.9;

% Normalize the signal
    y = y./max(abs(y));


% Transient fitting
%%%%%%%%%%%%%%%%%%%%%%%%%%%%%%%%%%%%%%%%%%%%%%%%%%%%%%%%%%%%%%%%%%%%%%%%%%%%

    % fit parameter initial and limit vectors
    fitstart = [1 -1 0 1 1 42 0.25 0.5];
    low_fit = [0.1 -2 0 -10 0.1 0 0.1 -1];
    up_fit = [5 1 1 10 10 80 2 1];

    % Calling our fitpumpprobe function
    result = fitpumpprobe(x,y,fitstart,low_fit,up_fit);
    z = result(x);

    % Plotting the fit and experimental data
    figure(1), clf
        plot(x,y,x,z,'r--')
        xlabel('Time [ps]')
        ylabel('\Delta R (arb. units)')
        set(gca,'YLim',[-0.05 1.05])
        figset
        legend('Exp','Fit')


% Oscillation and echo fitting
%%%%%%%%%%%%%%%%%%%%%%%%%%%%%%%%%%%%%%%%%%%%%%%%%%%%%%%%%%%%%%%%%%%%%%%%%%%%

    % Removing the transient part of the signal
    s = 140; e = 0;
    xt = x(s:end-e);
    yt = y(s:end-e);

    % Removing the thermal background signal
    yt2 = smooth(yt,250);
    yt3 = yt - yt2;

    % fit parameter initial and limit vectors
```

```
fs_o = [0.4 2 3 18.3 36 36 180 360 500 22.4 27 1.7 3 1.8];
low_o = [0.2 0 0 15 10 10 150 340 300 5 0 -10 -20 -10];
up_o = [10 10 10 19 100 100 220 380 1000 40 40 20 20 20];

% Calling our fitoscillation function
result_o = fitoscillation(xt,yt3,fs_o,low_o,up_o);
fit_o = result_o(xt);

% Plotting the fit and experimental data
figure(2),clf
    plot(xt,yt3,'k',xt,fit_o,'--m')
    xlabel('Time [ps]')
    ylabel('\Delta R (arb. units)')
    figset
    legend('Exp','Fit')
```

[1] D. L. Feldheim and C. A. Foss. *Metal Nanoparticles: synthesis, characterization and applications*. Marcel Dekker, New York, 2002.

[2] R. F. Haglund Jr. Ion implantation as a tool in the synthesis of practical third-order nonlinear optical materials. *Materials Science and Engineering A*, 253(1-2):275–283, 1998.

[3] U. Kreibig and M. Vollmer. *Optical properties of metal nanoparticles*. Materials Science. Springer-Verlag, Berlin, 1995.

[4] G. Mie. Contributions to the optics of turbid media, especially colloidal metal suspensions. *Annalen der Physik*, 25(3):377–445, 1908.

[5] C. Kittel. *Introduction to solid state physics*. John Wiley & Sons, New York, 8th edition, 2005.

[6] E. Kaxiras. *Atomic and electronic structure of solids*. Cambridge, New York, 2003.

[7] C. F. Bohren and D. R. Huffman. *Absorption and scattering of light by small particles*. John Wiley & Sons, New York, 1983.

[8] Howard DeVoe. Optical properties of molecular aggregates. i. classical model of electronic absorption and refraction. *The Journal of Chemical Physics*, 41(2):393–400, 1964.

[9] E. M. Purcell and C. R. Pennypac. Scattering and absorption of light by non-spherical dielectric grains. *Astrophysical Journal*, 186(2):705–714, 1973.

[10] C. Hafner and R. Ballisti. The multiple multipole method (mmp). *Compel - The international journal for computation and mathematics in electrical and electronic engineering*, 2(1):1–7, 1983.

[11] P. Barber and C. Yeh. Scattering of electromagnetic waves by arbitrarily shaped dielectric bodies. *Appl. Opt.*, 14(12):2864–2872, 1975.

[12] Staffan Ström. On the integral equations for electromagnetic scattering. *American Journal of Physics*, 43(12):1060–1069, 1975.

[13] R. E. Hummel and P. Wissmann. *Handbook of optical properties*, volume 2. CRC Press, New York, 1995.

[14] M. Quinten and U. Kreibig. Optical properties of aggregates of small metal particles. *Surface Science*, 172(3):557 – 577, 1986.

[15] K. Kneipp, M. Moskovits, and H. Kneipp. *Topics in Applied Physics; Vol. 103: Surface Enhanced Raman Scattering, Physics and Applications*. Springer, New York, 2006.

[16] M. E. Thomas, R. I. Joseph, and W. J. Tropf. Infrared transmission properties of sapphire, spinel, yttria, and alon as a function of temperature and frequency. *Applied Optics*, 27(2):239–245, 1988.

[17] K. Wefers and C. Misra. *Oxides and Hydroxides of Aluminum*. Alcoa Laboratories, 1987.

[18] Daniel C. Harris. A peek into the history of sapphire crystal growth. volume 5078, pages 1–11. SPIE, 2003.

[19] P. Klocek. *Handbook of infrared optical materials*. Optical engineering. Marcel Dekker, New York, 1991.

[20] G. Battaglin, E. Borsella, E. Cattaruzza, F. Gonella, R. F. Haglund Jr., G. Mattei, P. Mazzoldi, D. H. Osborne, and R. Polloni. Highly nonlinear optical composites obtained in silica and soda-lime glasses by Ti ion implantation and laser annealing. *Nuclear Instruments & Methods in Physics Research B*, 141(1-4):274–278, 1998.

[21] G. Battaglin, E. Cattaruzza, C. D. Fernandez, G. De Marchi, F. Gonella, G. Mattei, C. Maurizio, P. Mazzoldi, A. Miotello, C. Sada, and F. D'Acapito. Influence of post-implantation thermal and laser annealing on the stability of metal-alloy nanoclusters in silica. *Nuclear Instruments & Methods in Physics Research B*, 175:410–416, 2001.

[22] A. Halabica, R. H. Magruder III, and R. F. Haglund Jr. Modification of noble metal nanoparticles in a silica matrix by pulsed tunable infrared laser irradiation. *Proceedings of SPIE*, 6458:645810, 2007.

[23] M. Ferrari, L. M. Gratton, A. Maddalena, M. Montagna, and C. Tosello. Preparation of silver nanoparticles in silica films by combined thermal and electron-beam deposition. *Journal of Non-Crystalline Solids*, 191(1-2):101–106, 1995.

[24] F. Gonella, G. Mattei, P. Mazzoldi, E. Cattaruzza, G. W. Arnold, G. Battaglin, P. Calvelli, R. Polloni, R. Bertoncello, and R. F. Haglund. Interaction of high-power laser light with silver nanocluster composite glasses. *Applied Physics Letters*, 69(20):3101–3103, 1996.

[25] P. Huber, H. Karl, and B. Stritzker. Synthesis and laser annealing of embedded CdSe-nanoparticles in SiO_2 by pulsed excimer laser radiation. *Applied Physics Letters*, 88(20):203123, 2006.

[26] I. Okur and P. D. Townsend. Laser annealing and in situ absorption measurement of float glass implanted with Ag ions. *Nuclear Instruments & Methods in Physics Research B*, 222(3-4):583–586, 2004.

[27] A. L. Stepanov. Ion synthesis of copper nanoparticles in sapphire and their modification by high-power excimer laser pulses: A review. *Technical Physics*, 50(3):285–297, 2005.

[28] A. L. Stepanov and D. E. Hole. Implantation and laser annealing of Cu nanoparticles in silica. *Surface & Coatings Technology*, 158:526–529, 2002.

[29] A. L. Stepanov and V. N. Popok. Nanosecond pulse laser and furnace annealing of silver nanoparticles formed by implantation in silicate glass. *Surface & Coatings Technology*, 185(1):30–37, 2004.

[30] P. Townsend and J. Olivares. Laser processing of insulator surfaces. *Applied Surface Science*, 110:275–282, 1997.

[31] R. A. Wood, P. D. Townsend, N. D. Skelland, D. E. Hole, J. Barton, and C. N. Afonso. Annealing of ion-implanted silver colloids in glass. *Journal of Applied Physics*, 74(9):5754–5756, 1993.

[32] A. L. Stepanov, D. E. Hole, A. A. Bukharaev, P. D. Townsend, and N. I. Nurgazizov. Reduction of the size of the implanted silver nanoparticles in float glass during excimer laser annealing. *Applied Surface Science*, 136(4):298–305, 1998.

[33] A. L. Stepanov. Laser annealing of glasses with implanted metal nanoparticles. In *Recent research developments in non-crystalline solids*, volume 3, pages 177–198. 2003.

[34] D. R. Ermer, M. R. Papantonakis, M. Baltz-Knorr, D. Nakazawa, and R. F. Haglund Jr. Ablation of dielectric materials during laser irradiation involving strong vibrational coupling. *Applied Physics A*, 70:633–635, 2000.

[35] R. F. Haglund Jr. and D. R. Ermer. Explosive vaporization in fused silica initiated by a tunable infrared laser. *Applied Surface Science*, 168:258, 2000.

[36] A. Steigerwald, Y. Xu, J. Qi, J. Gregory, X. Liu, J. K. Furdyna, K. Varga, A. B. Hmelo, G. Lüpke, L. C. Feldman, and N. Tolk. Semiconductor point defect concentration profiles measured using coherent acoustic phonon waves. *Applied Physics Letters*, 94(11):111910, 2009.

[37] J. K. Miller, J. Qi, Y. Xu, Y.-J. Cho, X. Liu, J. K. Furdyna, I. Perakis, T. V. Shahbazyan, and N. Tolk. Near-bandgap wavelength dependence of long-lived traveling coherent longitudinal acoustic phonons in GaSb-GaAs heterostructures. *Physical Review B (Condensed Matter and Materials Physics)*, 74(11):113313, 2006.

[38] Mandelis A. *Photoacoustic and Thermal Wave Phenomena in Semiconductors*. Elsevier, New York, 1987.

[39] C. Thomsen, H. T. Grahn, H. J. Maris, and J. Tauc. Surface generation and detection of phonons by picosecond light pulses. *Phys. Rev. B*, 34(6):4129–4138, Sep 1986.

[40] O. B. Wright. Ultrafast nonequilibrium stress generation in gold and silver. *Phys. Rev. B*, 49(14):9985–9988, Apr 1994.

[41] O. B. Wright and V. E. Gusev. Ultrafast acoustic phonon generation in gold. *Physica B*, 219&220:770, 1996.

[42] B. Bonello, B. Perrin, E. Romatet, and J. C. Jeannet. Application of the picosecond ultrasonic technique to the study of elastic and time-resolved thermal properties of materials. *Ultrasonics*, 35:223, 1997.

[43] H.-N. Lin, R. J. Stoner, H. J. Maris, J. M. E. Harper, Jr. C. Cabral, J.-M. Halbout, and G. W. Rubloff. Nondestructive detection of titanium disilicide phase transformation by picosecond ultrasonics. *Applied Physics Letters*, 61(22):2700–2702, 1992.

[44] H. T. Grahn, H. J. Maris, J. Tauc, and B. Abeles. Time-resolved study of vibrations of a-Ge:H/a-Si:H multilayers. *Phys. Rev. B*, 38(9):6066–6074, Sep 1988.

[45] Aishi Yamamoto, Tomobumi Mishina, Yasuaki Masumoto, and Masaaki Nakayama. Coherent oscillation of zone-folded phonon modes in GaAs-AlAs superlattices. *Phys. Rev. Lett.*, 73(5):740–743, Aug 1994.

[46] Clément Rossignol, Bernard Perrin, Bernard Bonello, Philippe Djemia, Philippe Moch, and Hervé Hurdequint. Elastic properties of ultrathin permalloy/alumina multilayer films using picosecond ultrasonics and Brillouin light scattering. *Phys. Rev. B*, 70(9):094102, Sep 2004.

[47] Nen-Wen Pu. Ultrafast excitation and detection of acoustic phonon modes in superlattices. *Phys. Rev. B*, 72(11):115428, Sep 2005.

[48] Wei Chen, Yu Lu, Humphrey J. Maris, and Gang Xiao. Picosecond ultrasonic study of localized phonon surface modes in Al/Ag superlattices. *Phys. Rev. B*, 50(19):14506–14515, Nov 1994.

[49] Bruce M. Clemens and Gary L. Eesley. Relationship between interfacial strain and the elastic response of multilayer metal films. *Phys. Rev. Lett.*, 61(20):2356–2359, Nov 1988.

[50] Albrecht Bartels, Thomas Dekorsy, Heinrich Kurz, and Klaus Köhler. Coherent zone-folded longitudinal acoustic phonons in semiconductor superlattices: Excitation and detection. *Phys. Rev. Lett.*, 82(5):1044–1047, Feb 1999.

[51] R. E. Camley, B. Djafari-Rouhani, L. Dobrzynski, and A. A. Maradudin. Transverse elastic waves in periodically layered infinite and semi-infinite media. *Phys. Rev. B*, 27(12):7318–7329, Jun 1983.

[52] B. Djafari-Rouhani, L. Dobrzynski, O. Hardouin Duparc, R. E. Camley, and A. A. Maradudin. Sagittal elastic waves in infinite and semi-infinite superlattices. *Phys. Rev. B*, 28(4):1711–1720, Aug 1983.

[53] R. Danner, R. P. Huebener, C. S. L. Chun, M. Grimsditch, and Ivan K. Schuller. Surface acoustic waves in Ni/V superlattices. *Phys. Rev. B*, 33(6):3696–3701, Mar 1986.

[54] J. A. Bell, W. R. Bennett, R. Zanoni, G. I. Stegeman, C. M. Falco, and F. Nizzoli. Elastic constants of Mo/Ta superlattices measured by Brillouin scattering. *Phys. Rev. B*, 35(8):4127–4130, Mar 1987.

[55] W. J. Meng, G. L. Eesley, and K. A. Svinarich. Structural and elastic properties of zirconium nitride/aluminum nitride multilayers. *Phys. Rev. B*, 42(7):4881–4884, Sep 1990.

[56] R. Bhadra, M. Grimsditch, J. Murduck, and Ivan K. Schuller. Elastic constants of metal-insulator superlattices. *Applied Physics Letters*, 54(15):1409–1411, 1989.

[57] S. M. Rytov. *Akust. Zh.*, 2:71, 1956.

[58] M. Garfinkel, J. J. Tiemann, and W. E. Engeler. Piezoreflectivity of the noble metals. *Phys. Rev.*, 148(2):695–706, Aug 1966.

[59] T. Saito, O. Matsuda, and O. B. Wright. Picosecond acoustic phonon pulse generation in nickel and chromium. *Phys. Rev. B*, 67(20):205421, May 2003.

[60] O. Matsuda and O. B. Wright. Reflection and transmission of light in multilayers perturbed by picosecond strain pulse propagation. *J. Opt. Soc. Am. B*, 19:3028–3041, 2002.

[61] J. C. Pivin. Mixing of noble metals in oxides and formation of colloids by ion irradiation. *Materials Science and Engineering A*, 293(1-2):30–38, 2000.

[62] G. Battaglin, V. Bello, E. Cattaruzza, F. Gonella, G. Mattei, P. Mazzoldi, R. Polloni, C. Sada, and B. F. Scremin. RF magnetron co-sputtering deposition of Cu-based nanocomposite silica films for optical applications. *Journal of Non-Crystalline Solids*, 345:689–693, 2004.

[63] G. Battaglin, E. Cattaruzza, F. Gonella, R. Pollini, F. D'Acapito, S. Colonna, G. Mattei, C. Maurizio, P. Mazzoldi, S. Padovani, C. Sada, A. Quaranta, and A. Longo. Silver nanocluster formation in ion-exchanged glasses by annealing, ion beam and laser beam irradiation: An EXAFS study. *Nuclear Instruments & Methods in Physics Research B*, 200:185–190, 2003.

[64] P. D. Townsend, P. J. Chandler, and L. Zhang. *Optical Effects of Ion Implantation*. Cambridge, Cambridge, 1994.

[65] A. Meldrum, R. F. Haglund Jr., L. A. Boatner, and C. W. White. Nanocomposite materials formed by ion implantation. *Advanced Materials*, 13(19):1431–1444, 2001.

[66] A. Podlipensky, A. Abdolvand, G. Seifert, and H. Graener. Femtosecond laser assisted production of dichroitic 3D structures in composite glass containing Ag nanoparticles. *Applied Physics A*, 80(8):1647–1652, 2005.

[67] G. S. Edwards, D. Evertson, W. Gabella, R. Grant, T. L. King, J. Kozub, M. Mendenhall, J. Shen, R. Shores, S. Storms, and R. H. Traeger. Free-electron lasers: Reliability, performance, and beam delivery. *IEEE Journal of Selected Topics in Quantum Electronics*, 2(4):810–817, 1996.

[68] A. Miotello, G. De Marchi, G. Mattei, P. Mazzoldi, and C. Sada. Clustering of gold atoms in ion-implanted silica after thermal annealing in different atmospheres. *Physical Review B*, 63(7):075409, 2001.

[69] D. N. Nikogosyan. *Properties of optical and laser-related materials: a handbook*. John Wiley & Sons Ltd., New York, 1997.

[70] R. Kofman, P. Cheyssac, A. Aouaj, Y. Lereah, G. Deutscher, T. Bendavid, J. M. Penisson, and A. Bourret. Surface melting enhanced by curvature effects. *Surface Science*, 303(1-2):231–246, 1994.

[71] D. R. Collins, D. K. Schroder, and C. T. Sah. Gold diffusivities in SiO_2 and Si using MOS structure. *Applied Physics Letters*, 8(12):323, 1966.

[72] Wei-Kan Chu, J. W. Mayer, and M. Nicolet. *Backscattering spectrometry*. Academic Press, New York, 1978.

[73] G. De Marchi, G. Mattei, P. Mazzoldi, C. Sada, and A. Miotello. Two stages in the kinetics of gold cluster growth in ion-implanted silica during isothermal annealing in oxidizing atmosphere. *Journal of Applied Physics*, 92(8):4249–4254, 2002.

[74] A. Halabica, J. C. Idrobo, S. T. Pantelides, R. H. Magruder, III, S. J. Pennycook, and R. F. Haglund Jr. Pulsed infrared laser annealing of gold nanoparticles embedded in a silica matrix. *Journal of Applied Physics*, 103(8):083545, 2008.

[75] L. E. Kinsler, A. R. Frey, A. B. Coppens, and J. V. Sanders. *Fundamentals of Acoustics*. John Wiley&Sons, New York, 1981.

[76] H. N. Lin, R. J. Stoner, H. J. Maris, and J. Tauc. Phonon attenuation and velocity measurements in transparent materials by picosecond acoustic interferometry. *Journal of Applied Physics*, 69(7):3816–3822, 1991.

[77] R. Vacher and J. Pelous. Behavior of thermal phonons in amorphous media from 4 to 300 k. *Phys. Rev. B*, 14(2):823–828, Jul 1976.

[78] Lei Zhang, Rajendra Persaud, and Theodore E. Madey. Ultrathin metal films on a metal oxide surface: Growth of Au on TiO_2 (110). *Phys. Rev. B*, 56(16):10549–10557, Oct 1997.

[79] A. Arbouet, C. Voisin, D. Christofilos, P. Langot, N. Del Fatti, F. Vallée, J. Lermé, G. Celep, E. Cottancin, M. Gaudry, M. Pellarin, M. Broyer, M. Maillard, M. P. Pileni, and M. Treguer. Electron-phonon scattering in metal clusters. *Phys. Rev. Lett.*, 90(17):177401, Apr 2003.

[80] Nen-Wen Pu and Jeffrey Bokor. Study of surface and bulk acoustic phonon excitations in superlattices using picosecond ultrasonics. *Phys. Rev. Lett.*, 91(7):076101, Aug 2003.

[81] M. Trigo, A. Bruchhausen, A. Fainstein, B. Jusserand, and V. Thierry-Mieg. Confinement of acoustical vibrations in a semiconductor planar phonon cavity. *Phys. Rev. Lett.*, 89(22):227402, Nov 2002.

[82] M. F. Pascual Winter, G. Rozas, A. Fainstein, B. Jusserand, B. Perrin, A. Huynh, P. O. Vaccaro, and S. Saravanan. Selective optical generation of coherent acoustic nanocavity modes. *Physical Review Letters*, 98(26):265501, 2007.

[83] A. Huynh, B. Perrin, N. D. Lanzillotti-Kimura, B. Jusserand, A. Fainstein, and A. Lemaître. Subterahertz monochromatic acoustic wave propagation using semiconductor superlattices as transducers. *Physical Review B (Condensed Matter and Materials Physics)*, 78(23):233302, 2008.

[84] A. J. Kent, R. N. Kini, N. M. Stanton, M. Henini, B. A. Glavin, V. A. Kochelap, and T. L. Linnik. Acoustic phonon emission from a weakly coupled superlattice under vertical electron transport: Observation of phonon resonance. *Physical Review Letters*, 96(21):215504, 2006.

[85] G. Rozas, M. F. Pascual Winter, B. Jusserand, A. Fainstein, B. Perrin, E. Semenova, and A. Lemaître. Lifetime of thz acoustic nanocavity modes. *Physical Review Letters*, 102(1):015502, 2009.